Coronal active region modelling based on SDO data

DISSERTATION

zur Erlangung des Grades
„Doktor der Naturwissenschaften“

an der Fakultät für Physik und Astronomie
der Ruhr–Universität Bochum

von
Stephan Barra

geboren in
Witten

Bochum 2019

1. Gutachter	PD Dr. Horst Fichtner
2. Gutachterin	Prof. Dr. Julia Tjus
Datum der Disputation	3. Juli 2019

Contents

Chapter 1

Introduction

With its vast amount of appearances and phenomena, the hot and optically thin "atmosphere" of the Sun, the *solar corona* (figure 1.1), is an interesting environment in various aspects. The broad distribution of density, temperature, magnetic field strength and length and time scales spans several orders of magnitude in all of these quantities (see table 2.1). This provides an unique laboratory for many fields of physics which cannot be reproduced on Earth. Additionally, the corona influences our every day life all the time, as it is the source region of violent magnetic storms which can have severe and destructive effects on human life on earth. All this makes the corona an important field of interest for research.

As the solar corona consists of highly ionized gas and free electrons confined in strong magnetic fields (strong compared to the gas pressure), it is subject to plasma physics. In the less dynamic parts of the corona, waves and flows in confined plasmas can be studied, as well as the transport and deposition of energy. On the other hand, in the context of events of sudden, large energy releases, *flares* and *coronal mass ejections*, allow for the research of magnetic reconnection and particle acceleration.

Atomic physics is also relevant in the corona. Due to the high temperatures, extremely highly ionized ions exist in the corona, and their collisional behaviour and level transitions can be investigated. Even nowadays spectral lines become identified as transitions of certain ions.

Outstanding regions in the corona are *active regions* (ARs). Such ARs appear above groups of *sunspots*, i.e. large concentrations of magnetic flux on the solar surface, where the strength of the magnetic field exceeds the usual value by a factor of 1000. Among the corona, density, temperature and magnetic field are highest within ARs, and these regions are the most dynamic ones. In the extreme ultraviolet light (EUV) and in X-rays, magnetic flux tubes filled with hot plasma appear as distinguishable, thin and elongated *coronal loops* (figure 2.2).

From time to time, coronal structures break apart and material is accelerated into interplanetary space. If such a *Coronal Mass Ejection* (CME) hits Earth, the geomagnetic field is strongly disturbed by the interaction with the CME plasma. This phenomenon is called a *geomagnetic storm*. It causes aurora to appear in the sky. In extreme cases, high voltage can built up in power lines. This may overload and destroy the power and/or telecommunication network. Also, satellites in orbit around Earth are at risk due to the increased flux of highly energetic particles.

Having all this in mind, a deep understanding of the solar corona and its physics is worthwhile to achieve. While coronal research was restricted to solar eclipses until the invention of the coronagraph by Bernhard Lyot in the early 1930s (Lyot, 1931, 1932), space-borne instruments have given us a deep insight into the corona in the past decades. They allow for continuous observation over longer time periods from days to years, tracking the dynamic changes in the corona. Also, the corona can be observed in wavelengths absorbed by the terrestrial atmosphere. Additionally, with the swift growing of computational power, more and more detailed numerical research has become possible.

Nevertheless, despite all this progress made so far, we cannot explain one of the most basic physical properties of the corona: its temperature.

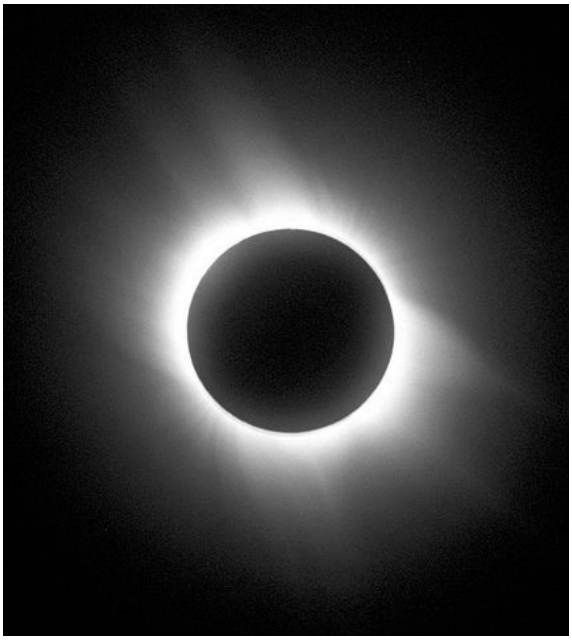

Figure 1.1: The solar corona during a total eclipse of the sun. Seen is the so called K-Corona which is produced by thermal electrons scattering sun light. (Photo by Ralf Künnemann, downloaded from `commons.wikipedia.org` on July 8th, 2014 under the Creative Commons Attributions-Share alike 2.5 Generic license: `Creativecommons.org/licenses/by-sa/2.5/deed.en`)

1.1 The coronal heating problem

The *photosphere*, the visible surface of the Sun, has a temperature of about 6,000 K. Thus, physicists in the late 19th, early 20th century expected the corona to be cooler in accordance with the laws of thermodynamics (Arrhenius 1904 estimated a value of 4620 K). When they started to discover the reality, they literally could not believe their findings in the beginning.

Schwarzschild (1906) measured the brightness of the corona in dependence of the distance r to the disc centre and claimed to agree with an empirically determined formula for which he refers to Turner[1], namely the intensity being $\propto (r/R_\odot)^{-6}$. Within the first 1.5 $R_\odot$ from the limb, this formula matches an exponential falloff with a scale height of 0.2 $R_\odot$, corresponding to a temperature of 2.8 MK. Back then, this conclusion was not drawn. Instead, Schwarzschild, while pointing out that electrons would display the observed radiative behaviour, argued against an electron corona and waived this proposition.

Grotrian (1931) interpreted the broadness of a dip in the spectrum of the inner corona around 385 nm as Fraunhofer Calcium lines, just thermally broadened to an extreme extent. He computed the thermal velocities involved to be 10 times higher than expected for 6000 K. This would relate to a 100 times higher temperature, but instead he assumed an anomalous effect to be at play.

Finally, Grotrian (1939) pointed out that two coronal lines coincide with forbidden transitions of Fe X and Fe XI. Later, Edlén (1943) then identified many coronal lines in the visible light and near infrared as emission lines of bound-bound transitions in highly ionized ions (like Fe X), concluding temperatures of some 10^5 K.

However, after the MK corona has been established, this leaves the question why the corona is so hot. This problem has been subject to research since then and has remained unanswered until now. While many mechanisms have been proposed, it is unclear which of these do act in the corona,

[1] Schwarzschild himself gives *Monthly Notices vol. 61* as reference, which usually refers to the Monthly Notices of the Royal Astronomical Society. Herbert Turner, Savilian Professor in Oxford that time, indeed published about solar eclipse observations in MNRAS these days. There is no such article including aforesaid formula at least in MNRAS vol. 61, nor in vol. 60 or 62, though.

if there is only one heating mechanism or if there are several ongoing at the same time. And if there are several, how do they interact? Which conditions cause which mechanism to operate or not in a certain location? Are the same mechanisms the most important ones everywhere in the corona? Or are different regions dominated by different mechanisms?

1.2 Scientific context

A detailed analysis of the solar atmosphere requires the determination of density and temperature in the corona. For energetic reasons (mechanical and thermal) it is not easily possible to make in-situ measurements in the corona. Instead, we are restricted to remote sensing nowadays, with the electromagnetic wave spectrum as the carrier of information.

The fundamental challenge of remote sensing the physical conditions of the solar corona is that the coronal plasma is optically thin over the entire range of electromagnetic wave frequencies. Hence, with the emission being barely absorbed, the detected intensity provides only a line of sight (LOS) integral. It lacks any information about the spatial distribution of emitting sources along the LOS.

A method for reconstructing this full 3D distribution of plasma emissivity would be a powerful tool of solar coronal research. Since the emission spectrum strongly depends on plasma temperature and density, monitoring the corona with such a tool in several wavelengths would allow a detailed tracking of the physical conditions of individual features, like loops, over their evolution in time. Such observations may be correlated to other observations, like those of the photosphere, which would give a deeper insight into the processes in the corona. Also, so far unknown correlations between phenomena in the corona, or correlations to other parts of the Sun, like the photosphere, might be recognised.

Thus, all this can greatly improve our understanding of the corona. It has a potential for allowing us to eventually understand the physics of the corona and maybe even forecast its behaviour, especially with regard to the Sun-Earth-connections.

1.2.1 State of the art

There are different approaches which potentially allow for retrieving the 3D distribution of the physical conditions in a solar AR.

Static modelling

It has been tried to reconstruct ARs in 3D using loop models. In this approach, extrapolated magnetic field lines are combined with theoretical models which describe the physical properties along the loop in dependence of a set of properties, like loop length or footpoint field strengths. With the resulting distributions of physical conditions satellite observations can be synthesized.

Schrijver et al. (2004) modelled the entire EUV corona to constrain possible heating mechanisms. Warren and Winebarger (2006) studied the scaling between the total integrated flux of an AR in soft X-rays and EUV and the total unsigned magnetic flux while changing the dependence of the model on field strength and loop length. The same authors used a dynamic model later for synthesizing images in the same bands (Warren and Winebarger, 2007). Lundquist et al. (2008a,b) compared their synthesized soft X-ray images with observations. Dudík et al. (2011) compared modelled temperature profiles with those obtained from observed filter ratios. All of them had the problem that the synthesised images only crudely coincide with the observations.

DEM analysis

Another approach is the analysis of the so called *differential emission measure* (DEM), a measure for the electron number in an infinitesimal temperature interval in dependence of the temperature (see chapter 3). From multi-band EUV observations, the DEM analysis results in values for density and temperature of the plasma within a line of sight (i.e. values for each pixel). Assuming that

the emission in a pixel originates only from exactly one loop and a background[2] which can be subtracted beforehand, these values correspond to the physical condition in the loop.

The spatial and temporal resolutions of this method is limited by the instrument, here by the time it needs for taking images in all of its passbands. It results are line-of-sight averages of the coronal plasma. When applying to loops, the background subtraction may become difficult where loops are criss crossing each other. The DEM analysis is based on an inverse problem, which is ill posed.

Kashyap and Drake (1998) wrote a DEM inversion code based on Monte Carlo chains. Hannah and Kontar (2012) used a regularization approach for tackling the problem. Del Zanna (2013) employs spline fitting for the inversion. Aschwanden et al. (2013) created a program which performs a DEM analysis on the whole sun.

Tomography

Tomographic methods reconstruct the 3D region of interest from two or more images regularly taken by the same observer over an extended time period (several days to a few weeks). Due to the rotation of the sun the region of interest moves underneath the observer and, thus, the perspective changes from image to image. These different perspectives eventually allow for reconstructing the spatial structure of coronal features.

An advantage of this method is that it requires only one instrument. Its disadvantage is that the images are taken over some time. This strongly reduces the temporal resolution to the period over which the sequence of images is taken. Coronal features usually evolve over such long time intervals. Hence, only long lasting structures can be analysed.

This method has been used by Kramar et al. (2009) to determine electron densities in extended coronal features. Aschwanden et al. (2000a) determined the geometric properties of coronal loops in an active region. Examples of such properties are the inclination angle to the solar surface and how planar and semicircular loops are, since this geometric assumptions have been made in many theoretical loop models (see chapter 7). Vásquez et al. (2011), using and DEM analysis, tomographicly reconstructed electron density and ion temperature of the entire corona at two different heights (about 21 Mm and 160 Mm above the solar surface), using observations of an entire Carrington rotation.

Stereoscopy

Stereoscopic methods avoid the problem of long time intervals by simply having two observers at different places at the same time. Like with the tomographic method, the different views on the same region make a 3D reconstruction possible. The advantage of stereoscopy is that is spatial and temporal resolution is limited by the instruments. The main disadvantage is its necessity of at least two instruments in significant different locations. Currently, this is mainly provided by STEREO data. The two STEREO probes were launched in October 2006, separating from earth by about 45 degrees per year (Kaiser et al., 2008). The observations STEREO has been made can be stereoscopically combined with data from SOHO (Fleck et al., 1995) and SDO (Pesnell et al., 2012, see chapter 4). In 2020, *Solar Orbiter* (Müller et al., 2013) is supposed to be launched, which also provides perspectives on the Sun different than from Earth at least in certain, regular observation windows.

Stereoscopic methods were used, for example, by Feng et al. (2007) to reconstruct coronal loops in 3D. In a series of papers, Aschwanden et al. (2008b,a, 2009) developed a code which triangulates the loops and models them, with the model parameters fitted in a way that the observed flux is reconstructed.

[2] In this context, any spatially homogeneous, the loop surrounding emission is called background. Thus, plasma in the foreground of the loop may also contribute to it.

Combining field modelling and loops traced in observations

Warren et al. (2018) developed a routine for matching loops traced in observations with the projections of field lines obtained from extrapolated coronal magnetic fields. The resulting combinations provide the physical conditions along the loops via the observations (for example using an DEM analysis). The field lines, on the other hand, give the 3D location of each point in the loops. Malanushenko et al. (2012) published a method to model the coronal magnetic field which incorporates observed loops. As a consequence, this method does not only yields a coronal field model but also links between field lines and traced loops, like above.

1.3 Motivation and goal of the thesis

The most dynamic and energetic events are observed in active regions of the sun. Here, we find much higher concentrations of magnetic field energy as well as higher temperatures and densities compared to other regions of the corona. Also, ARs display dynamics on time scales ranging from seconds to weeks, the lifetime of an AR. This makes the gaining of a comprehensive understanding of the processes ongoing in an AR a challenging task. Thus, ARs are subject to vast research, and we focus on them, too.

In this thesis we explore methods of determining the plasma configurations along the loops of an AR corona when the coronal magnetic field is given. As our main source of input data serves the *Solar Dynamics Observatory* (SDO, Pesnell et al. 2012), a space probe operated by NASA, and two of its instruments: The *Atmospheric Imaging Assembly* (AIA, Lemen et al. 2012) for images in the extreme ultraviolet (EUV) and the *Helioseismic and Magnetic Imager* (HMI, Schou et al. 2012) for measuring the photospheric magnetic fields. The outcome of the methods are 3D maps of density, temperature and pressure. Note that due to the equation of state, these quantities are connected to each other.

Due to the very low plasma beta, the AR coronal field $\vec{B}$ can be computed by extrapolating the measured photospheric fields assuming *force freeness*, i.e.

$$\nabla \times \vec{B} = \alpha(\vec{r})\vec{B},$$

with the spatial location $\vec{r}$ and a scalar function α. For AR loop modelling, mainly so called potential fields have been used (for example in most of the stationary modelling approaches mentioned above), defined by $\alpha = 0$. Such potential fields are fields of minimal energy with respect to a certain boundary condition (Woltjer, 1958). In contrast to this, the flux tubes of coronal loops are anchored in the high beta photosphere, and the photospheric motions causes stress onto the field (Sakurai, 1979) which enhances the field energy. Thus, in this work, instead of potential fields, we use a more realistic *non-linear force-free field* extrapolation (by Wiegelmann 2008), where α may vary in space, though not along a field line.

The goal of this thesis is to determine the 3D plasma configuration from observations. Several methods for doing so are presented. The ones among them which do not produce satisfying results are waived. Ultimately, a new tool which can approximate the AR corona from EUV observations and the magnetic field extrapolation is provided.

1.4 Outline of this thesis

First, we introduce the Sun and its atmosphere in chapter 2. We introduce the structure of the Sun as well as of the solar atmosphere. After this, some features of the solar surface and the solar corona are described. Among them, the ARs are discussed to a larger extent as they belong to the centre of our investigations.

In chapter 3 we briefly explain how the EUV line spectra of the corona are generated. The SDO satellite and its instruments are explained in chapter 4. Here, we go into the details of the calibration of AIA. Together with the equations of the previous chapter, we show how plasma emission creates AIA images since this is crucial for our work.

Afterwards, in chapter 5, a short overview over models of coronal heating and the observable signals they are expected to produce are given. Additionally, further processes that influence the energy budget of a loop are discussed.

The remaining chapters contain the results of our work. In chapter 6 we retrieve the physical properties of a loop directly from observations. In chapter 7 we use steady loop models to model an AR. Images synthesized from the resulting model AR are compared to observations. Finally, in chapter 8 we present a new, iterative method we developed to obtain the three dimensional atmosphere from single vantage point observations.

In chapter 9 we summarize the results of our work and present our conclusions, along with an outlook for future work.

Chapter 2

The Sun and its atmosphere

The Sun is a ball of gas and plasma which displays many interesting phenomena. Some of these phenomena are persistent while some others are episodic. In this chapter we present some of these phenomena and their observed physical conditions. As the corona of active regions is of special interest for this thesis, we go into further details for this part of the sun, compared to all other parts.

Both the standard model of the internal structure of the Sun and the structure of the solar atmosphere are well established and are described in various textbooks (like Bray et al., 1991; Stix, 2004; Aschwanden, 2004; Golub and Pasachoff, 2010) and thus will be presented here just briefly. When no further citations are given in this chapter, the reader is asked to look into such text books or reviews on the specific topics. Plots made by ourselves to illustrate something mentioned in this chapter are marked as own work.

2.1 Radial structure

2.1.1 Interior

The standard model of the Sun's internal structure is based on theoretical considerations and supported by numerical calculations and, especially, by the observations of neutrinos which are generated in the solar core as well as seismic waves observed on the photosphere.

The Sun has an inner *core* of a radius of about 250 Mm, in which hydrogen is transformed into helium via fusion. The energy produced by this reaction is radiated outwards as high-frequency electromagnetic (EM) waves. Within the core, the entire energy output of the sun is produced. The power at which this output takes place is known as the solar luminosity, which is of about $L \approx 3.8 \cdot 10^{26}$ W. Further outward, the core itself is followed by a *radiation zone* through that the radiation from the core can still easily travel. Different to the core, no fusion goes on in the radiation zone. However, about 500 Mm from the centre, the sun becomes opaque for the EM waves, and therefore, from here on, the energy is transported further outwards by a convective motion of the solar plasma. This gives the layer above the radiation zone its name, the *convection zone*. This convection zone reaches to the visible surface of the sun, the photosphere, which is located 696 Mm away from the centre.

All values mentioned above are current values for the sun. As for every other star, the values change over time because the fusion has only a finite amount of fuel and changes the chemical composition of the sun. However, the evolution of the sun is not subject of this thesis. Since we are interested in modelling current active regions, which have negligible lifetimes compared to that of the solar evolution (days compared to billions of years, respectively), we concentrate on the present state of the Sun.

A sketch of the solar internal structure is given in figure 2.1.

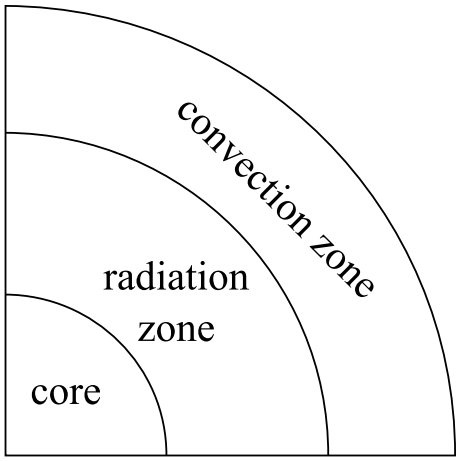

Figure 2.1: Cross section of the interior of a quarter of the sun (own work).

2.1.2 Photosphere

The *photosphere* is the visible surface of the sun. Above this very thin layer (300 to 500 km) EM waves of most frequencies can radiate outwards without much interference.

In vast parts of the photosphere the convective movements beneath appear as *granulation*: the up and down flow of hot cooling material. The granules appear as bubbles with a diameter of about 1 Mm and a lifetime around 6 minutes. The magnitude of the flow velocity is typically 1 to 1.5 km/s. Temperatures in the photosphere vary between 6000 K at the bottom and 4000 K at the top.

2.1.3 Chromosphere

The photosphere is followed by the *chromosphere* which appears as a red layer during a total eclipse. It is the solar "surface" for some chromospheric lines, notably Hα. Most important for the chromosphere, however, is the increase of the temperature with height. Indeed, the boundary between the photosphere and the chromosphere is defined by the temperature minimum. From the 4000 K at the lower edge, the temperature rises, first quickly, then much less steep to the range of 7000 K to 10 000 K at about 2000 km altitude.

2.1.4 Transition region

Between the chromosphere and the corona lies the transition region. It distinguishes itself from the neighbouring layers by its enormous temperature gradients. Within 100 to 200 km, the temperature jumps to 1 MK.

2.1.5 Corona

Historically, the corona is distinguished into different parts based on its appearance as a consequence of its constituents.

The *K-corona* (K is for Kontinuum) consists of photospheric light reflected at electrons. Due to the extremely wide thermal broadening, the Fraunhofer lines, well known from the photospheric spectrum, are missing in the light of the K-corona.

The *F-corona* (F is for Fraunhofer) is photospheric light reflected by dust. Unlike the K-corona, the F-corona displays the Fraunhofer lines since the dust is much cooler. Substantially, the F-corona extends far into interplanetary space, where it is called zodiacal light.

The dust which is responsible for the F-corona also emits thermal radiation due to its temperature, mainly in the infrared. This part is called the *T-corona*, where T is for thermal.

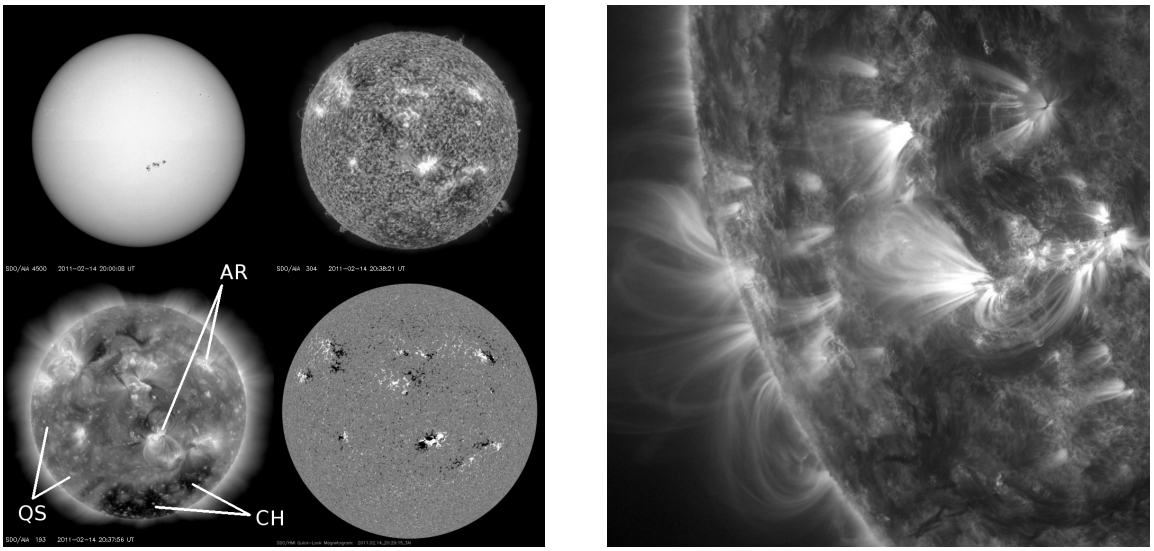

Figure 2.2: *Left:* The sun on Feb 14th, 2011, as seen by AIA in the 4500 Å (top left), 304 Å (top right), 193 Å(bottom left) channel. An HMI magnetogram is also shown (bottom right). In the 193 Å image, some examples for active regions (AR) and coronal holes (CH) are indicated, though more can be found. The quiet sun (QS) is also highlighted. Note that the ARs appear in the magnetogram as strong flux concentrations and in the optical image as groups of sunspots. *Right:* Part of the sun from Oct 27th, 2014, in AIA 171 Å channel. Coronal loops, fibres of radiating plasma confined in magnetic flux tubes, are a common feature (photos: NASA, own collection).

Finally, EUV and X-ray emission is radiated by the hot ions in the corona. This radiation is caused by level transitions of bound electrons, hence line emission. This part of the corona is called *E-corona* (for emission). The emitting ions form a plasma with the electrons of the K-corona. Thus, E-corona and K-corona share the same space.

The corona features temperatures in the MK range. The plasma is dominated by the magnetic field, which causes a prominent structuring of the corona, like coronal loops. These structures are addressed further below in more detail.

2.1.6 Interplanetary space and solar wind

Finally, parts of the corona transits into the *solar wind*, solar plasma radially expanding outwards permanently and filling the entire interplanetary space. This wind consists of two velocity components with flow velocities centred around 400 km/s and around 800 km/s. The exact processes of accelerating the wind particles is an entire topic of research by itself. Although it is linked to the coronal heating problem, it is not subject to this thesis. The fast wind components are related to coronal holes (see below), where particle can escape easily due to the "open" field structure.

At an altitude of about 400 to 500 Mm above the solar surface, the temperatures of electrons and ions begin to separate. While the electron temperature starts to drop from coronal temperatures, ions are heated and different ions reach different temperatures up to 100 MK. At about five solar radii, the solar wind becomes supersonic. Around 11 solar radii above the photosphere, the flow speed exceeds the Alfvén velocity (Stix, 2004, chapter 9.3.5).

2.2 Lateral structure

Besides the general radial structure mentioned above, the solar surface and atmosphere also show distinct, local features (figure 2.2).

2.2.1 Quiet Sun

The *quiet sun* takes up the largest fraction of the solar surface. The photosphere does not display any features besides the granulation. The magnetic surface field strength is, typically, of the order of 1 Gs, both positive and negative polarities mixed and varying on length scales similar to the granulation. In EUV, the corona appears as a homogeneous haze.

2.2.2 Bipolar regions

Bipolar regions consists of a part of positive and a part of negative polarity. The size of each of these parts significantly exceeds the length scales of the granulation. Though often this excess is not very high, bipolar regions can reach sizes of 100 Mm. It is common for bipolar regions to be formed by magnetic flux emerging to the surface. The smallest ones can be formed by random flux concentrations encountering each other by coincidence. The field strength in bipolar regions can achieve a few kGs. The polarity patches may have complicated geometric shapes, including fractionation.

2.2.3 Active regions

Active regions are formed by bipolar regions. In the photosphere they appear as sunspots, which are cooler (about 4500 K) and, thus, darker in the visible light than the surrounding quiet sun. The low temperature is the consequence of a very effective, but not total, suppression of the underlying convection by the strong magnetic fields. In the corona, ARs appear much brighter in EUV and X rays than the "quiet sun haze". Most prominently here are the coronal loops, EUV and/or X-ray bright plasma confined in the magnetic field, thus often outlying the magnetic connection between the two polarities or other bipolar regions.

2.2.4 Coronal holes

Coronal holes are regions where the magnetic field lines leading from the photosphere are "open", meaning that they leave the sun and first connect to the interplanetary field, and probably even further, before coming back to the photosphere. Since material can escape from the corona because of this field topology, the density of the corona is reduced in coronal holes, and these regions appear darker in emission than the quiet-sun corona.

2.2.5 Polar regions

At the poles, flux of one polarity is concentrated at latitudes roughly above 65° north, while flux of the other polarity can be found below 65° south. The field strength is of the order of 10 Gs. Following the solar cycle, the polarities are exchanged every 11 years. Above the poles, coronal holes can often be found.

Polar regions are difficult to observe from the ecliptic plane. For this reason, Solar Orbiter (Müller et al., 2013) is supposed to observe the Sun in an orbit inclined by 25°.

2.2.6 X-ray bright points

X-ray bright points (XBP) are small volumes in the lower corona emitting large X-ray flux. The XBPs appear all over the sun except for ARs. They are related to small bipolar regions. Their typical size is 50 Mm and they last for around a day.

2.2.7 The network

Besides the granules, a similar pattern of larger size can be observed, the *supergranulation*. It is connected to convection cells in the depth of the convection zone. Supergranules are of size of 10 Mm, have horizontal flow speeds of about 500 m/s and the upflow and downflow velocities are 50

	lg(L/Mm)	lg(n_e/cm^{-3})	lg(T_e/K)	lg(v/km/s)	lg(B/Gs)	ν_{ei}/Hz	lg R_m
AR loops	2 - 3.7 [3]	8.3 - 10.3 [3,4]	6 - 6.8 [2,3,4]		1 - 2.3 [1,3,4]	0.5 [1]	8 - 12 [1]
Coronal hole		6.2 - 8.3 [2,4]	5.9 - 6 [4]	1 - 1.2 [4]			
Flaring region	1.5 - 2 [3]	8.3 - 12.5 [3]	5 - 7.8 [3]	1.5 - 2.3 [3]	1.3 - 2.7 [3]		
X-ray bright point	1.7 - 2.3 [2]	9.7 [2]	6.3 [2]				
Quiet sun		7.9 - 8.6 [4]	6 - 6.3 [4]				

Table 2.1: Range of typical physical conditions for different parts of the solar corona. Given are the length scales L, electron number density n_e, electron temperature T_e, flow velocities v, magnetic field strength B, electron ion collision frequency ν_{ei}, and the magnetic Reynolds number R_m. Superscripts do not denote powers but sources: 1) Boyd and Sanderson (2003), 2) Golub and Pasachoff (2010), 3) Bray et al. (1991), 4) Aschwanden (2004) and references therein.

to 100 m/s. Along the edges of such supergranules, magnetic field is concentrated, the *network*. In the quiet-sun corona, a major part of the network field is connected to internetwork patches of magnetic flux, instead of other network field patches. In the chromospheric Ca II line, the network appears as a bright mesh.

2.2.8 Faculae

Facular fields are narrow flux tubes with a diameter of a few 100 km. Although they break vertically through the solar surface like the flux tubes of sun spots do, faculae appear brighter because of their low diameter. This is especially true when they are located near the limb, since faculae are depressions.In the side view the hotter and, thus, brighter walls of such depressions are easily visible.

2.3 The active region Corona

2.3.1 Physical conditions

The active region corona is dominated by magnetic flux tubes which connect, usually, two different polarities of a bipolar region. Plasma can broadly vary in density and temperature from flux tube to flux tube. Therefore, in EUV, the active region corona appears as a characteristic collection of coronal loops, elongated emitting plasma in a flux tube where the plasma in loops close by may not emit in the same wavelength.

The typical gas pressure of coronal AR plasma ranges from 0.1 to 1 dyne cm^{-2} while the strength of the magnetic field is about 10 to 100 Gs. Therefore, the ratio between gas pressure p_{gas} and magnetic pressure p_{mag}, commonly referred to as the *plasma beta*, is typically

$$\beta = \frac{p_{gas}}{p_{mag}} = \frac{8\pi p_{gas}}{B^2} \ll 1, \tag{2.1}$$

(cgs) which is the reason why the plasma is dominated by the magnetic field (fig. 2.4).

The appearance of a loop depends on the physical conditions of the plasma within. The EUV radiation mainly consist of line emission. The electron temperature defines the wavelength in which a loop, or parts of it, are visible, since different ions are present at different temperatures. As the line emission, to a large part, comes from bound-bound transitions in ions, where the excitation had been caused by collisions with thermal electrons beforehand, the density of the free electrons define the number of transitions and thus the intensity of the radiation.

Whenever we write about the temperature in this thesis, we refer to the electron temperature, if not stated otherwise. This is common practice in literature about the solar corona. The ion temperatures are of similar order, as collision time between ions and electrons (see table 2.1) are shorter than the processes in AR loops.

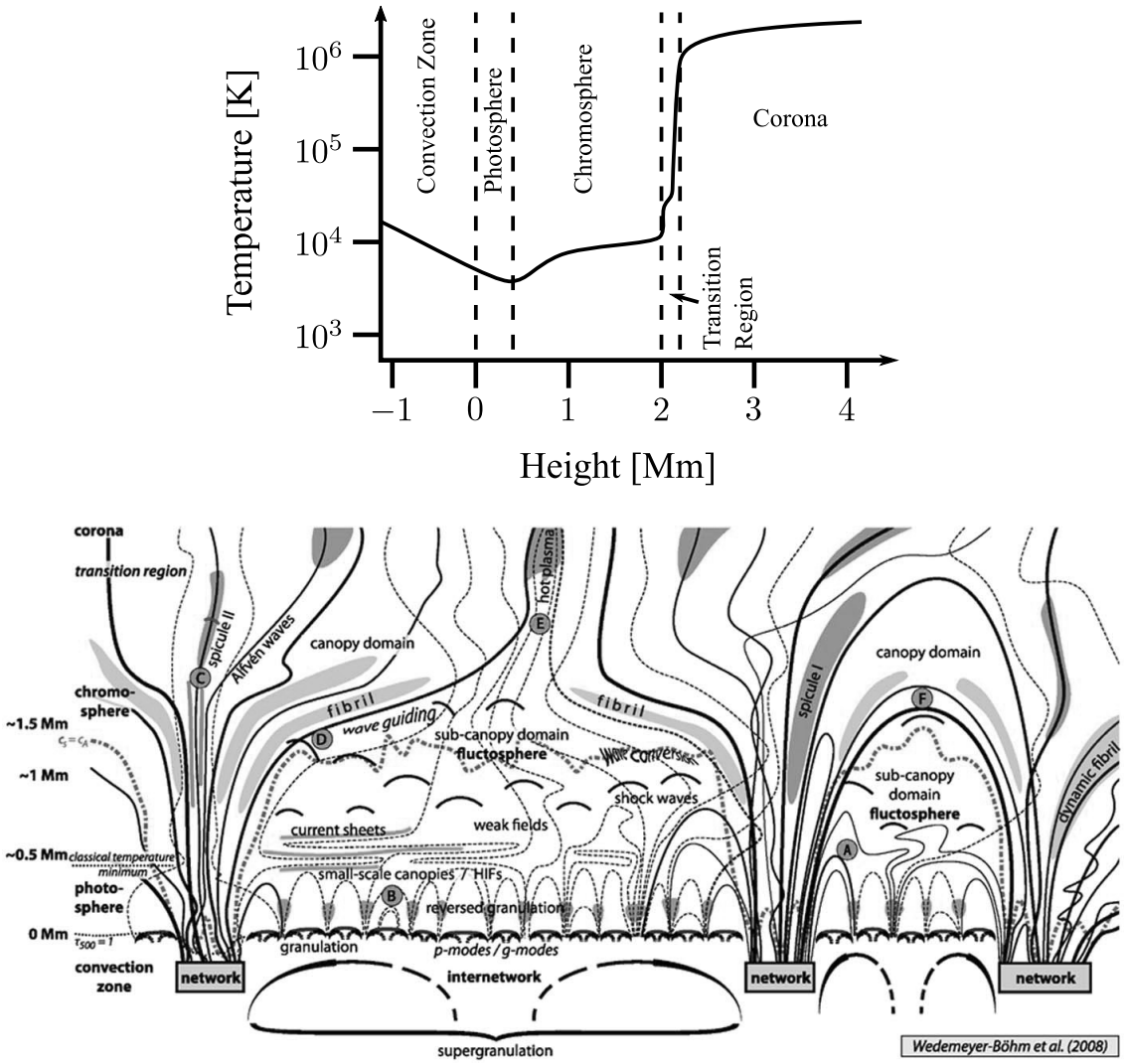

Figure 2.3: *Top*: A simple, layered solar atmosphere was one of the first ideas of the hot corona and still presents a global, rough average for the different altitudes. Thus, similar diagrams can be found in various textbooks (own work). *Bottom*: In reality, the situation is far more complex and spatial dependent to a high degree (from Wedemeyer-Böhm et al., 2009).

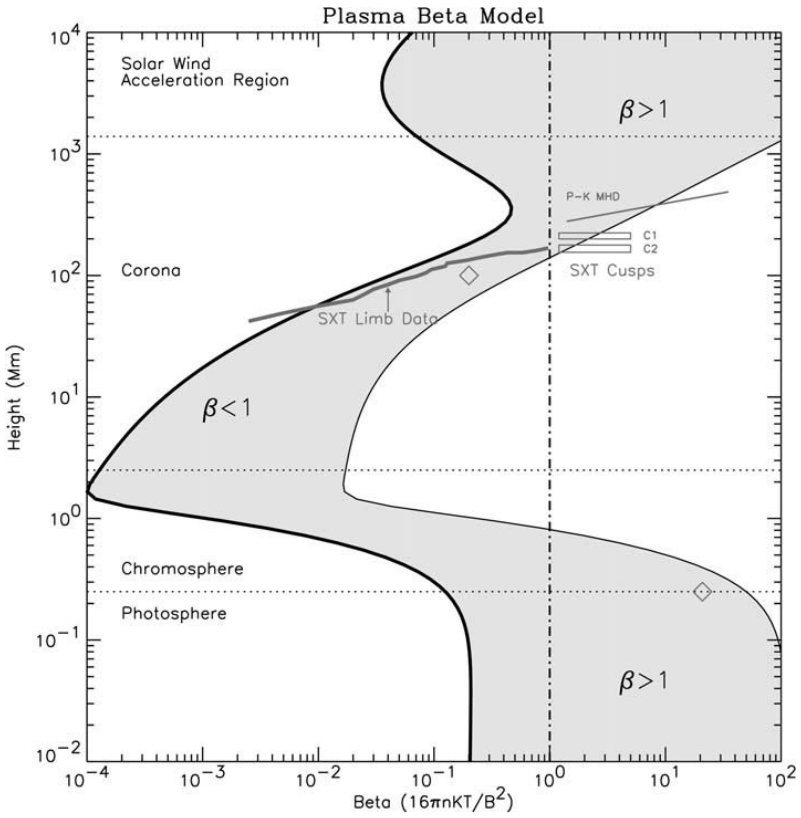

Figure 2.4: Plasma beta in the solar atmosphere (from Gary, 2001).

The geometric shape of a loop follows the flux tube it is trapped in. Thus, there are short loops that connect the edges of the two polarities which are facing each other as well as extremely long loops, arching over the entire AR and reaching high altitudes. Also, some loops connect to other parts of the sun like a neighbouring active region.

Observations have shown that the short loops in the core are the hottest ones, with temperatures of 3 MK and more in their coronal parts, while the footpoints are typically at 1 MK. Densities in these loops usually are 10^9 to 10^{10} cm^{-3}. The core loops appear steady relative to their radiative cooling time (for example Warren et al., 2010).

Contrary to that, loops anchored in the umbra do not appear to be heated at all. Their densities are similar, but their temperature is around 20 kK (Bray et al., 1991, sec. 2.4.3 & 2.5).

Long loops overarching the entire AR usually are cooler than the core loops, having an electron temperature of 1 MK. The typical densities of these loops is 10^9 cm^{-3}. The long loops can show spatial and temporal variations in their brightness which are commonly assumed to be related to heating and cooling. Estimated cooling times, though, are longer than expected for pure radiative cooling (Lenz et al., 1999).

Most of the magnetic flux tubes leaving the photosphere do not reach to the corona. Instead, they connect back to the photosphere within short distance. Such chromospheric, or even photospheric, loops form the *magnetic carpet* (Schrijver et al., 1997; Title and Schrijver, 1998). Flux tubes which reach to the corona, however, pass through the chromosphere as narrow hoses, so called *funnels*, and widen when they reach the transition zone (Warren et al., 2008).

2.3.2 Elemental Abundances

As usual for the sun, the solar corona consists of about 90% hydrogen and 10% helium, with traces of heavier elements (table 2.2). However, radiation observed in EUV mainly originates from

element	photosphere (1)	corona (2)	element	photosphere (1)	corona (2)
H	12.0	12.0	S	7.12	7.27
He	10.93	10.9	Cl	5.5	5.5[(3)]
Li	1.05	1.64[(3)]	Ar	6.4	6.58
Be	1.38	1.94[(3)]	K	5.03	5.67[(4)]
B	2.7	3.09[(3)]	Ca	6.34	6.93
C	8.43	8.59	Sc	3.15	3.71[(3)]
N	7.83	8.0	Ti	4.95	5.56[(3)]
O	8.69	8.89	V	3.93	4.54[(3)]
F	4.56	4.56[(3)]	Cr	5.64	6.21[(3)]
Ne	7.93	8.08	Mn	5.43	5.93[(3)]
Na	6.24	6.93	Fe	7.5	8.1
Mg	7.6	8.15	Co	4.99	5.46[(3)]
Al	6.45	7.04	Ni	6.22	6.84
Si	7.51	8.1	Cu	4.19	4.75[(3)]
P	5.41	5.45[(3)]	Zn	4.56	5.14[(3)]

Table 2.2: Elemental abundances on a logarithmic scale with H normalized to 12. These values are used in the CHIANTI atomic database v8.0.2 (Dere et al., 1997; Del Zanna et al., 2015). [(1)]From Asplund et al. (2009). [(2)] From Feldman et al. (1992), if not said otherwise. [(3)]From Grevesse and Sauval (1998) with the abundances of elements with an FIP below 10 eV enhanced by a factor of 3.5. [(4)]From Landi et al. (2002).

these heavy elements, especially iron. Elements with low *first ionization potential* (FIP) below 10 eV have enhanced abundances compared to the photosphere by a factor of roughly 3 (Cassé and Goret, 1978). In the literature, this observation is referred to as the *FIP effect*.

2.3.3 Magnetic field

Due to the low optical thickness of the plasma, the magnetic field is hard to measure directly in the corona. Few approaches were made into that direction (like Sahal-Brechot et al., 1986; Long et al., 2017).

Nevertheless, the common way to obtain the coronal magnetic field is to extrapolate it from photospheric vector magnetograms. In the photosphere, where the optical depth approaches unity within a few hundred kilometres, the magnetic field vectors can be measured deploying polarimetry (for example del Toro Iniesta, 2003). Several codes exists for the task of the extrapolation. A review about these approaches can be found in Wiegelmann (2008). The methods use the fact that the plasma beta is low in the corona. With the gas pressure and the gravity having negligible effects on the geometrical structure of the loop, also the Lorentz-force has to vanish, as otherwise the loops would not display the observed stability. This means that the magnetic field has to be parallel to its own curl, i.e.

$$\nabla \times \vec{B} = \alpha(\vec{r})\vec{B}. \tag{2.2}$$

In this equation, α is a scalar which can vary from field line to field line but is constant along a field line. Magnetic fields fulfilling the equation above are called *force-free fields*. Within this group, three sub-types are usually distinguished: force-free fields without further constraints on α except for the invariance along the field lines mentioned before are labelled *non-linear force-free fields* (NLFFF). In *linear force-free fields* (LFFF), α is spatially constant but different from 0. *Potential fields* have $\alpha = 0$ everywhere (Wiegelmann, 2008). Figure 2.5 plots field lines for each of the three types of extrapolation. All fields are extrapolated from the same magnetogram. Also the starting points for the Runge-Kutta-Iterator which computes the field lines from the extrapolated fields are the same. The differences between the three fields are obvious.

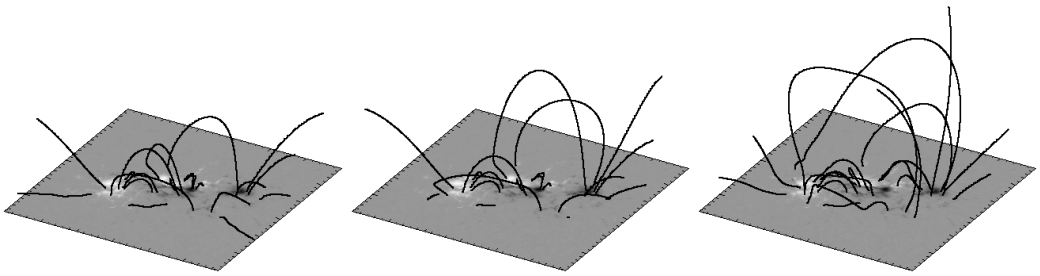

Figure 2.5: Twenty field lines for different magnetic field models for AR 11158, Feb. 14th, 2011, extrapolated from the same foot points. From left to right: potential field, linear force-free field with $\alpha = 2$, non-linear force-free field. The differences are striking (own work, field extrapolations courtesy T. Wiegelmann).

Chapter 3

Radiation of coronal plasma

In this work, we analyse the EUV radiation with wavelengths of about 100 Å. Hence, we have to know how this radiation is generated in the solar corona and transported through it. The description given in this chapter can be found again in several textbooks or reviews (like Mason and Fossi, 1994; Golub and Pasachoff, 2010; Stix, 2004; Aschwanden, 2004; Bray et al., 1991, and others) as well as in the handbook of the atomic database CHIANTI (Dere et al., 1997) that can be used to synthesize solar spectra.

It has to be mentioned that the theory given in this chapter holds, strictly speaking, for conditions of local thermodynamic equilibrium (LTE) as well as ionization equilibrium only Mason and Fossi (1994); Golub and Pasachoff (2010). Also, the calculations made by CHIANTI are valid just in case of both equilibria. Here, LTE means that a temperature can be assigned to the electrons at any location. Also, the population and de-population rates of levels are in equilibrium. Ionization equilibrium demands that an equilibrium in both the ionization and recombination rates of atoms could have been established. This is not necessarily the case in the AR corona, since the highly dynamical processes within its loops can dis-balance these rates. The heating and cooling, for example, changes the temperature and therefore the degree of ionization. However, such non-equilibria do not have a strong effect on the total radiative loss rates (Klimchuk, 2006, sec. 5). As a consequence, in this thesis, we can safely restrict ourselves to the CHIANTI loss rates.

Additionally, the coronal plasma is assumed to be optically thin, which means no absorption of the emitted EUV radiation occurs (Bray et al., 1991; Aschwanden, 2004, and others). This is not perfectly true, of course, but a very reasonable approximation (Pottasch, 1963). As a consequence the radiation emitted in some place of the corona is assumed not to affect the emission of plasma elsewhere, in accordance with the locality of the LTE.

Atmospheric models that incorporate the non-vanishing optical thickness of the plasma and non-LTE conditions exist (like that by Milić and van Noort, 2017), but they are, so far, 1D models restricted to the chromosphere and photosphere. Thus, we stay with the approximation of an optically thin plasma in LTE, allowing us the investigation of its 3D structure.

3.1 The coronal approximation

The EUV emission of coronal plasma is mainly due to line transitions in atoms. In principle, there are many processes for populating and depopulating the energy levels in atoms. The physical conditions in the corona provide a simplification for calculating line transitions commonly referred to as the *coronal approximation*. In this approximation it is assumed that any excited level is populated from the ground state only and only by collisions with free, thermal electrons. On the other hand the de-excitation happens due to spontaneous emission only (e.g. Aschwanden, 2004; Golub and Pasachoff, 2010). We apply this approximation in our thesis, too.

3.2 General description of emission and radiative transfer

3.2.1 Contribution of line emission

A large fraction of coronal emission originates from bound-bound line emission (for example Bray et al., 1991; Golub and Pasachoff, 2010). An important fact for coronal observations and analysis comes in handy: the mathematical description of the intensity of EUV emission can be separated into an atomic part and a part depending on the plasma and its physical state.

For a transition between a lower level a and an upper level b of an atom the excitation rate, which is proportional to the free-electron density n_e, may be written as $n_e C_{ab}$ and the de-excitation rate as A_{ba}. The coefficients A and C are known as *Einstein coefficients*. According to LTE, we assume the transitions into both directions to be in equilibrium. If the number densities of a certain ion in ground state a and an excited state b are denoted with n_a and n_b, respectively, $n_a n_e C_{ab} = n_b A_{ba}$ holds. If the de-excitation process emits photons of a frequency ν_j, the emissivity ε_j of the line, or radiative power density, is

$$\varepsilon_j = h\nu_j A_{ba} n_b$$

To split this into the atomic part and the plasma part, this expression is usually expanded by multiplying unity:

$$\begin{aligned}\varepsilon_j &= n_e^2 h\nu_j \frac{A_{ba} n_b}{n_e n_a} \frac{n_a}{n_I} \frac{n_I}{n_Z} \frac{n_Z}{n_H} \frac{n_H}{n_e} \\ &= n_e^2 \hat{G}_j(T, n_e).\end{aligned}$$

The so called *Contribution Function* $\hat{G}(T, n_e)$ now depends on atomic data only. This data can be determined by laboratory experiments and theoretical calculations. It is independent of the actual plasma in which the atoms are observed and can be made accessible via databases like CHIANTI (Dere et al., 1997). The contribution consists of several ratios. The first one, $A_{ba} n_b / n_a n_e = C_{ab}$ describes the excitations in case of transition equilibrium. The second one is the number density of ions in the lower state relative to the total number density n_I of that ion. The next fraction is the degree of the ionization for that ion, i.e. the amount of the specific ion relative to all atoms of the element, having a number density of n_Z. Followed by this is the elemental abundance relative to hydrogen and the last factor is the ratio of hydrogen number density n_H to the electron number density.

The fraction n_a/n_I is roughly unity. The de-excitation happens about 10 000 times faster than the excitation, hence most ions are in the lower state. On the other hand, the corona is, at least for lighter elements, a fully ionized plasma. With its 90% of hydrogen and 10% of helium in numbers (table 2.2), the ratio of total ionization is $n_H/n_e \approx 5/6$

The contribution function $\hat{G}_j$ has a sharp peak in temperature, since a certain ion can exist in a narrow temperature range only. If the environment is too cold the atoms cannot be transformed into the ions emitting line j. If it is too hot, the atoms will be ionized even further. Hence the ratio n_i/n_Z is a narrow function of temperature and $\hat{G}_j$ inherits this sharpness. For that reason temperature analyses of the corona can be done by EUV and X-ray observations since at different temperatures different ions are present that emit in different wavelengths.

The total emissivity of a plasma is now the sum of the emissivities of all lines:

$$\begin{aligned}\varepsilon_{tot} &= \sum \varepsilon_j \\ &= n_e^2 \sum \hat{G}_j(T, n_e) \\ &= n_e^2 \Lambda(T, n_e). \end{aligned} \tag{3.1}$$

The function Λ is named the *radiative loss function*. In the description above the contribution function of a line is a delta distribution in wavelength, but of course there are effects (like thermal or turbulent motions) that cause the line to smear out in wavelength (see below). Since the

contribution functions are weakly sensitive to changes in density, the dependence on n_e is often dropped.

Hence the contribution function can be taken from databases, we consider it as "known" in this thesis, though significant changes have been made over the years. Such changes are made whenever new lines become identified and are included into the calculations, or when the abundances are changed.

3.2.2 Broadening of emitted wavelengths

The delta-peak, as used above, is only a theoretical simplification of a spectral line. In real measurements, the detected emission from a single line does not have an unique wavelength. Instead, effects like thermal broadening widens the emission, causing the line to form a line profile. The power density becomes a wavelength-depended differential emissivity then,

$$\begin{aligned}\varepsilon_j &= \varepsilon_j(\lambda) \\ &= n_e^2 \hat{G}_j(\lambda, T, n_e)\end{aligned}$$

of the dimension power per volume and wavelength. The contribution function now contains the shape of the line profile, too. Adding up the contributions of different lines to a single wavelength yields the differential emissivity of the wavelength

$$\varepsilon(\lambda) = \sum_j \varepsilon_j(\lambda).$$

Thus, the total emissivity is again

$$\begin{aligned}\varepsilon_{tot} &= \int_0^\infty \varepsilon(\lambda)\, d\lambda \\ &= n_e^2 \Lambda(T, n_e).\end{aligned} \tag{3.2}$$

Furthermore, we can define a total contribution function

$$\hat{G} = \sum_j \hat{G}_j.$$

In general, the emitted power might depend on the direction. The omnipresent magnetic field in the corona causes a spatially inhomogeneous environment, for example. Hence this is not the case for the intensity of EUV radiation of coronal plasma, we do not consider such an effect in this thesis. Nevertheless, we mention here that the polarisation state depends on the magnetic field. This is used to measure the magnetic field on the photosphere, where the sun becomes optically thick.

3.2.3 Line-of-sight intensity and the differential emission measure

The coronal plasma is considered as an optically thin plasma. Hence the total differential flux of emitted radiation along the LOS received at a single point of view is simply the integrated differential emissivity of the plasma in the LOS:

$$\begin{aligned}\hat{I}(\lambda) &= \frac{1}{4\pi} \int_{LOS} \varepsilon(\lambda)\, dz \\ &= \frac{1}{4\pi} \int_{LOS} n_e^2(z) \hat{G}\big(\lambda, T(z), n_e(z)\big)\, dz\end{aligned} \tag{3.3}$$

that is of dimension power per area, wavelength and steradians. The factor $1/4\pi$ is for the reason that ε itself describes the total power per wavelength, spread over all directions.

In coronal physics, an often used measure is the *differential emission measure* DEM[1] (Craig and Brown, 1976)

$$DEM(T) = n_e^2 \frac{dz}{dT}, \tag{3.4}$$

that allows to rewrite equation (3.3) as

$$\hat{I}(\lambda) = \frac{1}{4\pi} \int_0^\infty \hat{G} \cdot DEM \; dT. \tag{3.5}$$

The $DEM(T)$ describes the amount of free electrons in the LOS having a temperature in the interval between T and $T + dT$. In the corona, the DEM usually has a local maximum around $T = 1$ MK, as this is a typical temperature of coronal plasma.

[1] It has to be taken care of that different definitions of the DEM exist in literature. There are one-dimensional definitions, like we use in this thesis, as well three-dimensional ones, like in the original publication. Also sometimes the product of electron and hydrogen number densities, $n_e n_H$, is used instead of the square of the electron density.

Chapter 4

The Solar Dynamics Observatory SDO

In this section we will describe NASA's satellite *Solar Dynamics Observatory* (SDO), whose data are of immediate importance for our work. After a short introduction of the satellite itself we present it's three scientific instruments. The *Extreme ultraviolet Variability Explorer* (EVE) does not play a role to this thesis and will be mentioned only briefly. This is also true for the *The Helioseismic and Magnetic Imager* (HMI). At least, its magnetograms are the basis for the magnetic field reconstruction and can provide us with additional information about the physical quantities in coronal loops, as explained later.

Special emphasis is given to the *Atmospheric Imaging Assembly* (AIA). Since we want to produce artificial images that can be compared to real AIA observations, we have to carefully mimic the way AIA generates images out of the incoming light. Therefore, great parts of this chapter are for explaining the details how the observed photon flux affects the instrument and, vice versa, is affected by the instrument, in order to understand what we see with AIA and how we see it.

4.1 General information about SDO

SDO is a satellite operated by NASA, launched at February 11th, 2010. Its goal is to image the Sun at high spatial and temporal resolution, observing its dynamics and understanding the influence of these variations onto life and Earth. SDO is in a geosynchronous orbit to remain in contact with its own ground station in New Mexico, USA.

The satellite faces the sun all the time. This allows for continuous observations except for two times per year, around the spring and autumn equinoxes. Both sun and earth are in SDO's orbital plane then and this causes the earth to occult the sun once per day during these phases (see SDO webpage; SDO mission webpage).

4.2 The Extreme ultraviolet Variability Explorer (EVE)

EVE (Woods et al., 2012) is a spectrograph for the extreme ultraviolet radiation. It takes EUV spectra in the range from 1 to 1050 Å, with an resolution of 1 Å. The spectra are taken every 20 seconds. To cover the entire range, EVE consists of several detectors that measure the incoming EUV radiation in different passbands (see EVE webpage).

4.3 The Helioseismic and Magnetic Imager HMI

The *Helioseismic and Magnetic Imager* (Schou et al., 2012) provides observations of magnetic fields in the photosphere. HMI images the polarized white light of the sun's surface with a cadence of 45 seconds and a spatial resolution of 0.91". The methods of spectropolarimetry (for example del Toro Iniesta, 2003) are used to translate the polarized light into 3D magnetic field vectors. These *magnetograms* are used as a basis for the extrapolations of the magnetic field into the corona required for our work in this thesis.

These observations directly provide images of the surface taken in the range of the thermal continuum, i.e. the visible light. Additionally, HMI delivers dopplergrams used for helioseismology (see HMI webpage).

4.4 The Atmospheric Imaging Assembly AIA

The Atmospheric Imaging Assembly is an imager, which means its takes photos like a common photo camera, in difference to a spectrometer. Spectral information is obtained by using colour filters, though these are broad band filters (filter width between 10 and 20 Å compared to 76 mÅ for HMI). AIA observes the sun with a spatial resolution of 0.6" (about 450 km at the sun) and a cadence of 12 seconds in each filter. The images are taken with ten different filters. Seven of them are in extreme ultraviolet (94 Å, 131 Å, 171 Å, 193 Å, 211 Å, 304 Å and 335 Å). Two are in the ultraviolet range (1600 Å and 1700 Å). One filter observes in white light (4500 Å). All channels are named after the wavelength in Ångstroms at which the channel's passband is centred (see AIA webpage).

4.4.1 Instrumental setup

This subsection 4.4.1 briefly describes the setup of AIA. The information given here can be found, among further details, in Lemen et al. (2012).

AIA consists of four generalised Cassegrain telescopes. All of them are observing in at least two channels, where either shutters or filter wheels are used to select between the channels. As it has been said before, seven channels observe in the extreme ultraviolet, but on one telescope several additional filters have been installed for the ultraviolet (UV) and white light observations.

The detection of the photons is done by CCD chips with 4096×4096 pixels in each of the telescopes. The resolution is 0.6 arcsec per pixel, the field of view measures 41 arcmin. This is enough to observe the entire disk of the sun (that has a size of about 30 arcmin) at once, including the corona up to half of a radius of the sun over the limb. Images are usually taken every 12 seconds in each EUV channel, but observations with a cadence down to two seconds with a smaller field of view can be made, for example to observe very dynamic events like solar flares.

Each pixel has a size of 12 μm. The corners of the CCDs lye in the shadow of the filter wheels. Hence they are never illuminated by the sun, they are used as a reference for the camera noises. The full-well capacity is of about 150,000 electrons per pixel. The detectors have been subdivided into four parts of 2048×2048 pixels, which are read out simultaneously with a rate of 2 Megapixels per second. Each of these quarters have a readout noise lower than 25 electrons.

The primary mirrors have a diameter of 20 cm, and the holes in their middle a diameter of 6.5 cm. Each of the, in total, eight mirror halves have a different coating to make them reflective in the desired wavelengths. In each telescope, filters in front of the CCDs then select between the different channels provided by the mirror.

The filters are made of zirconium (for the 94 and the 131 Å channels) or aluminium (for observations in the longer wavelengths) and are placed close to the focal plane, directly in front of the CCD sensors. The filter wheels contain up to four types of filters for EUV observations: a thin zirconium filter and a thin aluminium filter which are used for operations, and a thick zirconium and a thick aluminium filter for redundancy. In telescope 1 (131/335 Å) and telescope 4 (94/335 Å) no more filters are required to block the light observed by the one half of the primary mirror

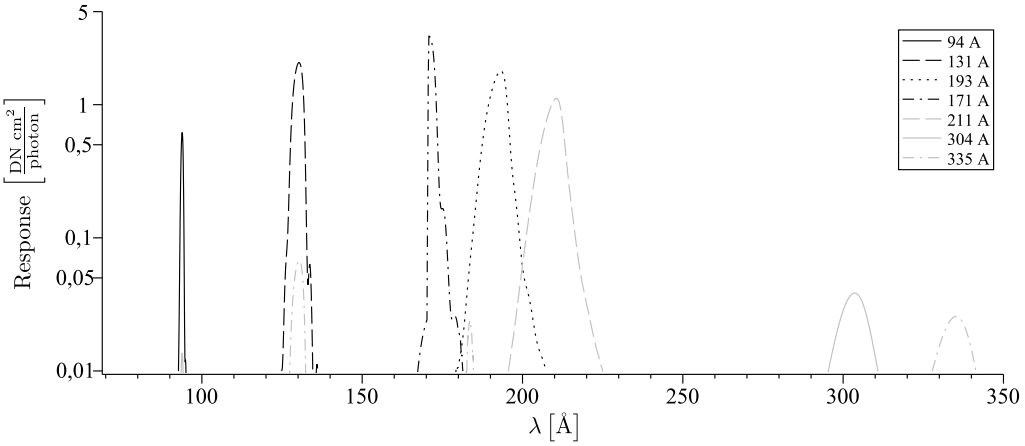

Figure 4.1: The AIA wavelength response functions R_i of the EUV channels.

or the other. Telescope 2 (193/211 Å) however uses a blend at the aperture to select between its two channels, as both of the observed wavelengths can pass the aluminium filter. Hence it lacks the zirconium filters. Telescope 3 (171 Å/UV) has, besides the thin and the thick aluminium filter, three different additional filters for its UV and white light channels, but no further ones. All filters are supported by a mesh made of nickel with a spacing of 70 line-per-inch. These meshes cast a shadow pattern on the CCDs that can be removed by flat fielding (see section 4.4.4).

The entrances of the telescopes are equipped with additional filters to remove radiation in undesired UV, IR and visible light regimes. These filters are also supported by 70 line-per-inch meshes that cause diffraction patterns here (see section 4.4.3).

4.4.2 Instrument calibration

The instrument calibration describes the strength of the signal, measured in digital numbers (DN), depending on the incoming photon flux and the selected channel. The initial calibration of AIA is explained in Boerner et al. (2012), and the informations and equations presented in this subsection 4.4.2 are taken from there.

If the subscript i denotes the associated measure for the i-th channel, and we want to describe the information obtained by a certain pixel p in this channel, one can do this by

$$p_i = \int_0^\infty A_{eff,i}(\lambda)\tilde{g}(\lambda)F(p) \int_{FOV} I(\lambda,\Omega)d\Omega\, d\lambda.$$

The *effective area* $A_{eff,i}$ takes into account the effects of the optical system onto the incoming photon flux. It is given by

$$A_{eff,i} = A_{geo}R_{P,i}(\lambda)R_{S,i}(\lambda)T_{E,i}(\lambda)T_{F,i}(\lambda)Q(\lambda)D(\lambda,t)$$

where A_{geo} is the geometric size of the collecting area, $R_{P,i}$ and $R_{S,i}$ are the reflectances for the primary (P) and secondary (S) mirror in the given channel, $T_{E,i}$ and $T_{F,i}$ are the transmissivities of the filters at the entrance (E) of the telescope or near the focal plane (F), respectively. The measure Q is the quantum efficiency of the detector and the factor D describes the degradation of the instrument.

The *system gain* $\tilde{g}$ of the camera, measured in DN per photon, includes the photon to electron conversion (in electrons per photon) and the camera gain (in DN per electron). The system gain $\tilde{g}$ ranges from 0.6 DN per photon to 2.13 DN per photon, depending on the EUV channel.

The dimensionless *flat-field function* $F(p)$, which depends on the pixels, collects all effects that systematically affect the detected light on each pixel, like diffraction and shadowing of the filter

supporting meshes, slightly variations of the sensitivities of each pixel and so on. Subsection 4.4.4 will give some further details about the flat-field function.

The measure I [photons Å^{-1} sr^{-1} s^{-1} cm^{-2}] is for the differential photon flux. It is physically identical to the differential flux $\hat{I}$ defined in (3.3), but differs in the way that $\hat{I}$ uses Watt whereas I is in photons per second. Thus their relation is $h\nu(\lambda)I(\lambda) = \hat{I}(\lambda)$, with h being Planck's constant and ν the frequency of the photon. We keep the hat to formally distinguish between the two fluxes, and will do the same with the contribution function G. Here, we also include the factor 4π, so that $h\nu G = \hat{G}/4\pi$, since it is this G that can be obtained from the CHIANTI database (Dere et al., 1997).

Finally, p_i is the counting rate for the pixel p observing through filter i, and is of units DN s^{-1}. Integrated over the exposure time of an image, it yields the DN value for that pixel. Hence, the final image is the array of the DN values from all pixels of the CCD.

The *wavelength responses* $R_i(\lambda)$ for the filters are given by

$$R_i(\lambda)[\text{DN cm}^2 \text{ photon}^{-1}] = A_{eff,i}(\lambda)\tilde{g}(\lambda).$$

The wavelength responses for the seven EUV channels are shown in figure 4.1. However, as mentioned in chapter 3.2.1, the constituents of coronal plasma emit EUV radiation only in a very narrow temperature range. Using (3.5),

$$I(\lambda) = \int_0^\infty G \cdot DEM \; dT,$$

we can write the detected count rate on the pixel p as

$$p_i = \int_0^\infty R_i(\lambda)F(p) \int_{FOV} \int_0^\infty G(\lambda, T) \cdot DEM(T) \; dT \; d\Omega \; d\lambda.$$

The temperature integral represents the LOS integration. Together with the integration over the FOV this yields a 3D integral over the entire volume of emitting plasma observed by the pixel.

The observed solid angle Ω might be expressed in multiples of the solid angle Ω_0 observed by one pixel: $\Omega = \Omega_0\omega$, if ω pixels are involved. AIA has a spatial resolution of about 0.6". With SDO being $r_S \approx 1.5 \cdot 10^5$ Mm away from the sun, Ω_0 is $8.4 \cdot 10^{-12}$ st per pixel (fig. 4.3). This allows us to substitute the solid angle integration by an integration over the illuminated fraction of a pixel: $d\Omega = \Omega_0 \; d\omega$. Quite naturally, when integrating over exactly one pixel, we end up with $\omega = 1$ pixel. But later in this work we will add up contributions from fractions of a pixel. Thus, $\omega \in \mathbb{R}$.

As the wavelength responses R_i of the instrument and the contribution function G are known from measurements, both can be combined to a *temperature response*:

$$K_i(T) = \; \Omega_0 \int_0^\infty R_i(\lambda)G(\lambda, T)d\lambda,$$

which has a dimension of DN cm^5 s^{-1} pixel^{-1} and is displayed in figure 4.2. This allows for expressing the counting rate of the pixel in terms of the DEM:

$$p_i = \; F \int_{pixel} \int_0^\infty K_i \cdot DEM \; dT \; d\omega. \tag{4.1}$$

The factor F from the flat field can be extracted from the integral as it is constant over an entire pixel. In our work we often approximate the solar atmosphere by small cubes filled with an isothermal plasma of temperature T and of constant density n. In this case, using (3.4) backwards,

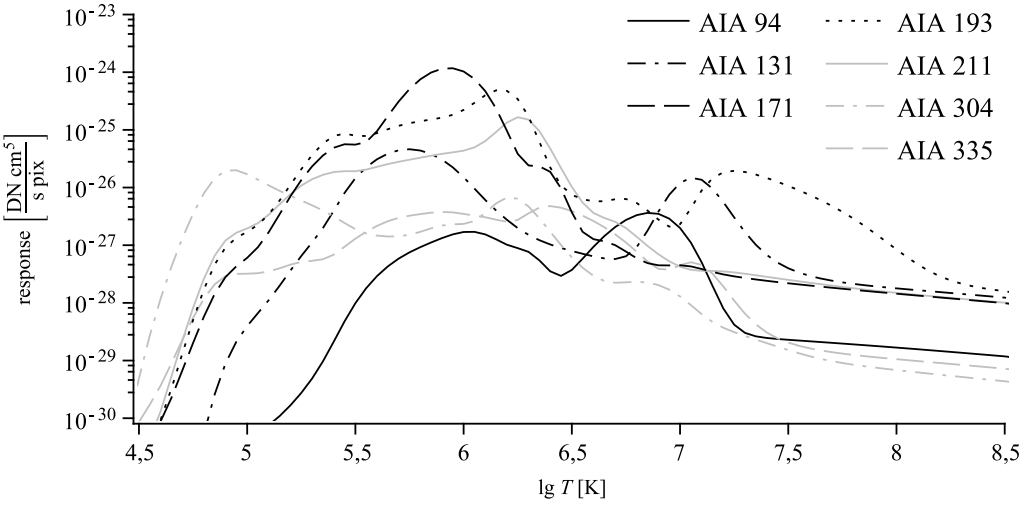

Figure 4.2: The temperature response functions K_i of the EUV channels in dependence of the temperature at launch. They were calculated as described in Del Zanna et al. (2011) using CHIANTI v8.0.2 (Dere et al., 1997; Del Zanna et al., 2015) and the coronal abundances as given in table 2.2.

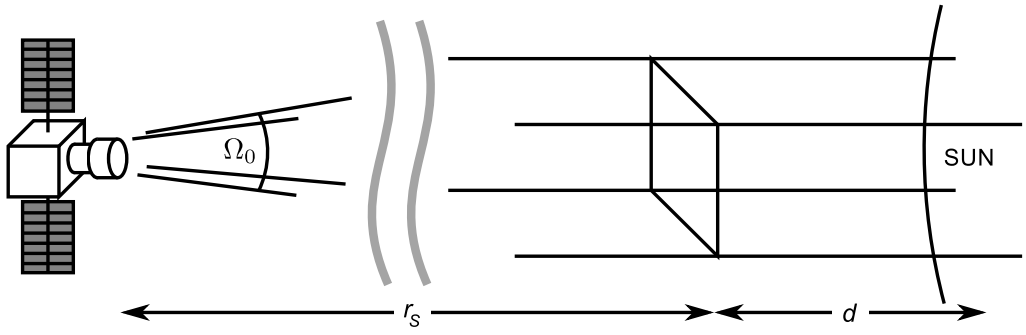

Figure 4.3: Schematics of a pixels field of view. The pixel observes a solid angle of Ω_0. Since the sun is far away, and the observed part of its atmosphere is thin compared to the distance ($r_S \gg d$), the line of sights might be considered parallel on the sun (own work).

we can express the contribution of the small, single volume to the count rate of pixel p in filter i as

$$\begin{aligned} p_i^{vol} &= F\omega \int_{z_0}^{z_1} n^2 K_i(T)\, dz \\ &= F\omega n^2 K_i(T) \Delta z \end{aligned} \tag{4.2}$$

with ω denoting the fraction of the pixel illuminated by the volume and z_0 and z_1 the locations of the front and the rear surface of the cell along the LOS, respectively.

The effective areas and the temperature responses are provided by the AIA team via SolarSoft (Freeland and Handy, 1998) in IDL (see Boerner et al., 2012). Another way to calculate the temperature responses is described in Del Zanna et al. (2011). Both of them employ the CHIANTI database (Dere et al., 1997) to obtain the contribution function G.

4.4.3 Point spread function

As mentioned in section 4.4.1 above, the meshes which supports the filters produce a diffraction pattern on the images. Additionally, the mirrors and the CCDs can contribute to these patterns,

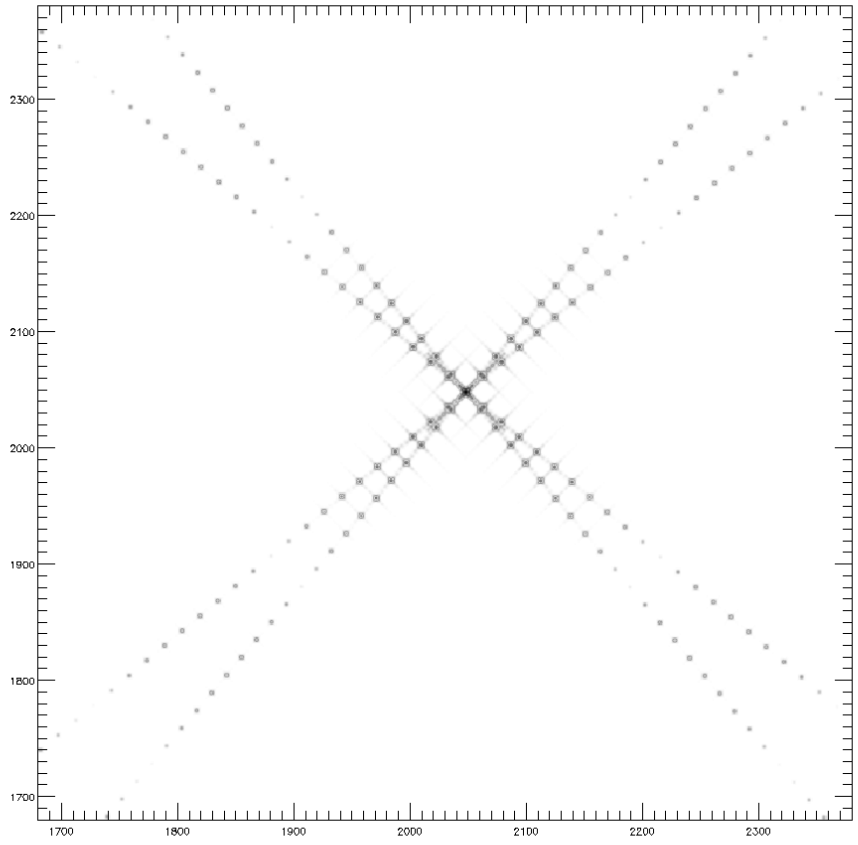

Figure 4.4: Point spread function for AIA's 211 Å channel. The numbers on the axes are the pixel numbers (from Grigis et al., 2012).

too. The resulting image of a point source of light is called the *point spread function* (PSF). A detailed description of this effect and how to deal with it is given in Grigis et al. (2012). Figure 4.4 shows a modelled PSF for the 211 Å passband of AIA. The PSFs for the different EUV channels have been obtained from analyses of images taken during operation of AIA. Like the response functions, these PSFs are provided via SolarSoft by the AIA staff, together with a procedure to deconvolve the images.

4.4.4 Flat-field function

The flat-field function corrects for phenomena like varying sensitivity of different pixels, slightly different gains in different quadrants, vignetting or contamination by dust. It appears at a simple factor (F) for each pixel in the calibration and is normalized to 1. The flat-field is checked for temporal evolution from time to time.

4.4.5 Data processing

AIA images are 4096 $\times$ 4096 arrays, where each entry is a number in a measure, the DN, which depends linearly (besides noise and errors) on the incoming intensity of EM radiation. These

images, as they are, are called level 0 images. However, two further levels of processed images are provided, the level 1 images and the level 1.5 images. This image processing is described in Lemen et al. (2012) and is summarised here.

Level 1 images

The processing pipe line to level 1 mainly removes the noise and errors of the detectors. First, so called over/scan rows and lines are removed, if present. These are remnants of charges from previous read-outs.

Second, the dark image, the image one would obtain in a completely dark universe without incoming radiation, is removed. This dark image is caused by the read noise and dark current, due to thermal effects.

As third step, the flat field function (see section 4.4.4) is applied to the image.

Fourth, the DN value of permanently malfunctioning pixels are replaced by an interpolation of the DN values of adjacent pixels.

Fifth, "spikes" within the images, these are pixels which have unexpected and significantly higher DN values than other pixels close by, are removed. This is done by replacing the pixels value to the median of the values from pixels in the surrounding. The "spikes" can be produced by energetic particles, for example.

Finally, the image is flipped so that the north of the sun appears on top and the south in the bottom of the image. Though, the rotational axis might still be inclined to the image axis.

All information used for the data procession to get level 1 images (like the list of malfunctioning or despiked pixels or the flatfield) are provided with the images, so that level 1 images can be reprocessed to level 0 again, without loss of information.

Level 1.5 images

As AIA takes EUV images every 12 seconds, thus monitoring the dynamics of the solar corona with a high cadence, it is one of the goals of the mission to support videos of the sun displaying these dynamics (Lemen et al., 2012). In these videos, the Sun should neither bobbing around nor shrink or grow from frame to frame. To do so, further processing of the level 1 images is done.

First, the images are rotated in a way that the image of the sun has an inclination angle of $0°$. This means that the line from north to south pole is parallel to the left and right edges of the images, with north heading to the top edge. This step is necessary because, although the four telescopes have been co-aligned prior to the launch, a residual roll within a quarter of a degree between them still remains (Boerner et al., 2012).

Second, a kind of "digital zoom", the so called plate-scale correction, is applied to adjust each image to a field of view with 0.6 arcsec per pixel. The sun appears in the same size in each filter then.

Third, the slight differences in the bore-sights of the telescopes are corrected so that the Sun's centre appears in the middle of each image.

4.4.6 Errors

Boerner et al. (2012) also estimated the measurement errors of AIA caused by uncertainties in the instrument calibration. According to them the 1σ error in the effective areas A_{eff} adds up to 28%, with the contamination and the quantum efficiency of the detectors being the largest contributors. The cameras themselves have read out noises between 1.14 and 1.2 DN. Their response to the incoming photon flux is linear within 1% up to 11 kDN, a value not reached outside of flares.

Chapter 5

Coronal heating theory

The energy budget of a loop consists of the heating E_H, the total radiative cooling ε_{tot} and the conductive losses $\dot{U}_C$. All these terms together describe the rate of change of the thermal energy density

$$\dot{U}_{th} = E_H - \varepsilon_{tot} + \dot{U}_C.$$

In general, all these terms depend on location, temperature, density and plasma composition. In the following, we give a quick overview over the models. The two cooling terms on the right hand side are relatively well known, and their descriptions are well established in the scientific community. The heating term E_H and its underlying physics are yet not fully understood and has been debated since decades. Hence, many models are under discussion.

5.1 Heating mechanisms

The energy required to maintain the observed coronal temperature is only 0.01% of the solar energy release (for example Stix, 2004, sec. 9.4.1, Walsh and Ireland, 2003, Golub and Pasachoff, 2010, sec. 7.4). It is broadly agreed that the energy for heating the corona is taken from the motions of the photospheric plasma where the field lines are anchored in (Aschwanden, 2004, sec. 9.2, Golub and Pasachoff, 2010, sec. 7.4, among others). Many theories have been proposed for transporting this energy into a coronal loop and transforming it into heat there. We introduce here the main approaches which are generally discussed in reviews like Narain and Ulmschneider (1996), Walsh and Ireland (2003), Klimchuk (2006), De Moortel and Browning (2015) or textbooks (Aschwanden, 2004, chp. 9, Bray et al., 1991, sec. 5.7, Stix, 2004, sec. 9.4, Golub and Pasachoff, 2010, sec. 7.4).

5.1.1 Dissipation processes

There are, ultimately, few processes which can generate thermal energy from other kinds of energy.

Compression

The compressional shock dissipation of waves is one of the mechanisms which is considered for coronal heating. Here, the internal energy of the gas is changed when the flow velocity $\vec{u}$ compresses (or relaxes) the gas, i.e.

$$\nabla \cdot \vec{u} \neq 0.$$

Joule heating

Electric currents produce heat with a power of

$$\frac{\vec{j}^2}{\sigma}, \tag{5.1}$$

with $\vec{j}$ being the current density and σ the electrical conductivity. However, the ratio of Joule heating to compressional heating is

$$\frac{\vec{j}^2}{\sigma p\,|\nabla \cdot \vec{u}|} \approx \frac{1}{\beta R_M}, \tag{5.2}$$

here p denoting the plasma pressure, $\vec{u}$ the velocity of the flow, β the plasma beta and R_M the magnetic Reynolds number. In the solar corona, β is about 0.01 to 0.1, while R_m is in the range of 10^{10} (see table 2.1), when considering the length scales of a coronal loop. Thus, mechanical work would outweigh the Joule heating by far, making it in principle negligible. Nevertheless, the joule heating is one of the main dissipations mechanisms in coronal heating theory, since in many proposed mechanisms very short length scales are produced. On these short length scales the magnetic Reynolds number is locally decreased far enough for the heating process to become efficient.

Viscous dissipation

Viscous dissipation as a heating mechanism is discussed for shear waves. At a shear viscosity μ and a flow velocity $\vec{u}$, the heating power here goes with

$$\mu \sum_{ij} \partial_j u_i.$$

However, the shear viscosity is small compared to the compressional viscosity (Ofman et al., 1994), thus the gradients have to be large again. Likewise for the Ohmic heating, the viscous dissipation requires short length scales.

Wave damping

For the heating of ions, resonant damping of cyclotron waves has been considered for the solar corona and for the acceleration of the solar wind (Hollweg, 1986; Isenberg, 1990; Marsch and Tu, 1997a,b). Also, the thermal velocities of the electrons in the MK plasma are comparable to the wave velocities, like the Alfvén velocity. Thus, waves can experience Landau damping.

5.1.2 Scale transfer mechanisms

Both the Ohmic heating as the viscous dissipation require length scales several orders of magnitude shorter than the typical length of a coronal loop. In literature, different mechanisms allowing this situation to occur have been proposed.

Phase mixing

Heyvaerts and Priest (1983) investigated a configuration where shear Alfvén waves, with a displacement vector in y direction, travel along field lines in z direction. The gradual variation of the Alfvén speed in x direction causes the waves on two neighbouring lines to become out of tune with each other. Due to their mutual coupling the waves become damped. In laminar situations, the authors estimated the damping length in open field lines and the damping time in closed structures like loops to scale with $R_{tot}^{1/3}$. The value R_{tot} is a "total Reynolds number" which includes both magnetic diffusivity and kinematic viscosity. In the same publication, the authors point out that due to the small scales the phase mixing produces, the coronal plasma can be in a state of permanent Kelvin-Helmholtz-like turbulence, so that the laminar picture breaks down and both damping length and damping time become significantly shortened, increasing the heating power. Abdelatif (1987) denoted that high-frequency waves can deposit their entire energy into the corona, but no such waves were observed. Whereas, the observed low-frequency waves do not dissipate enough energy to account for the entire heating. On the other hand, Hood et al. (1997) found that

the phase mixing of shear Alfvén waves can heat the corona on time scales equal or shorter than the radiative cooling time scales, and may provide at least a base level of heating. Similon and Sudan (1989) and Malara et al. (2000) proofed that the scaling mentioned above holds in (quasi) 2D field geometries, like in Heyvaerts and Priest (1983), but in really 3D field configurations, the damping length and time rather go as $\propto \ln R_{tot}$, which means an enhancement of the heating.

Shear Alfvén waves generated in the foot points and dissipated by phase mixing release their energy near the footpoints and, thus, a brightening in X-rays is expected there (Abdelatif, 1987).

Resonant layers

Ionson (1978) suggested the idea of resonant layers in coronal loops: MHD surface waves are transmitted into the inner part of the loop. Due to inhomogeneous Alfvén velocities, there is at some point a thin layer of field lines which is in resonance and becomes heated. Later, Ofman et al. (1998) pointed out that the heated layers move across the loop since density changes where the resonant heating occurs and the heated field lines becomes detuned while others tune in. They also showed that a broadband spectrum for the driver is required for sustaining the heating. Beliën et al. (1999) found that a large amount of the energy in the Alfvén waves is converted into energy for exciting magnetosonic waves, while traversing the chromosphere. They conclude that, hence, the energy which can be dissipated by resonant layers is strongly depleted, though the magnetosonic waves may contribute to the heating due to shock dissipation. De Groof and Goossens (2002) demonstrated that when using drivers with random spectrum resonant layers can appear in every location within the loop.

Resonant layers are very thin, between 300 m and 250 km, depending on the assumptions made (Davila, 1987), which is beyond the resolution of current observations. Additionally, they expect the root mean square of non-thermal velocities to be 2 to 6 km/s (Davila, 1987).

Braiding, Current sheets and Nanoflares

Parker (1983a,b, 1988) suggested that magnetic flux tubes become twisted and braided with neighbouring tubes due to footpoint motions. The magnetic field eventually reconnects at such discontinuities in the field topology, releasing their energy in small, short and impulsive events called nanoflares. Additionally, small-scale current sheets appear and become dissipated where the flux tubes are entangled.

Van Ballegooijen (1986) showed numerically that the large-scale stress indeed can be transferred to small scales when the coronal flux tubes split up into finer filaments, like the funnels, near the photospheric footpoints. In another numerical braiding model, they concluded that braiding itself may cause too less heating to explain the coronal temperatures alone (van Ballegooijen et al., 2017).

Hudson (1991) pointed out that for nanoflares to support the entire coronal heating, the power law which describes the differential flare frequency in dependence of the flare energy,

$$\frac{dN}{dE} \propto E^{\alpha},$$

must have a slope $\alpha < -2$. For such a slope, the the major contribution to the energy input is from the small flares. For slopes less steep, the large flares dominate. (Aschwanden, 2004, chapter 9.8).

Turbulence

In turbulent models the permanent mechanical stress on the loops due to footpoint motions induces energy on larger scales into the coronal loops. The turbulence cascades this energy to the small scales where Joule heating occurs.

Heyvaerts and Priest (1992) derived that such turbulent velocities should be 20 to 30 km/s. In the simulations by Dmitruk et al. (1998), the turbulent heating appears to be similar to nanoflare heating. Chae et al. (2002) determined that turbulent heating would occur near the footpoints.

5.1.3 AC heating vs. DC heating

In the literature, the mechanisms are commonly divided into AC or DC mechanisms (for alternating and direct current, respectively), based on their typical time scales. The discriminating time is the time an Alfvén wave needs to travel from one footpoint of a loop to another. Processes faster than this Alfvén travel time of 5 to 8 minutes are denoted as AC processes. Mechanisms acting on longer time scales are collected into the group of DC mechanisms.

Basically, all wave approaches belong to the AC group. The current sheet dissipation and nanoflare models are based on the loop braiding, hence they are associated to the DC heating. Turbulent models exist for both groups.

5.2 Some observational constraints

It must be pointed out that deducing the heating from observations is a difficult task. Examples where the interpretation of observations led to intense discussions are given in Walsh and Ireland (2003, sec. 3.3.3). This includes the case where, from the same data set, Priest et al. (2000), Aschwanden (2001) and Reale (2002) deduced a uniform heating along the loop, a heating at the footpoint or a heating at the loop top, respectively.

While the heating itself is not observable, the back reactions of the plasma onto it are. Since the availability of space-borne observations, the corona has been observed in X-rays and the EUV. Many events have been reported and have been connected to coronal heating. All of these observations must be explained by a consistent theory of coronal heating. Many of these observations are established. If no further citation is given, summaries and their general conclusions can be found in textbooks like the ones already mentioned in section 5.1. The little overview is, of course, not exhausting.

With Multi-passband-imagers like AIA inversions of the DEM can be performed (see section 1.2.1). Such analysis makes clear that coronal active region plasma can be found within the entire temperature range from one to several MK. Short loops in the core of active regions are generally hotter and less variable in intensity than long loops footed in the outer parts of an AR. From the Umbrae of sun spots, however, no X-ray or EUV loops emerge.

From the non-thermal broadening of lines, Chae et al. (1998) found velocities up to 30 km/s in plasma below 2 MK. This matches the expected velocities of the turbulent models as well as the estimates for the resonant layer heating.

At the coronal footpoints of hot loops, Testa et al. (2013) identified brightenings with a lifetime of 15 seconds. They interpreted these as signatures of nanoflares, as both have similar amount of energy.

Also, waves can be observed in the corona (like in Morton and McLaughlin 2014). The waves in coronal loop become damped when their energy is transferred to heat. In hot loops, the modelled damping times of magnetosonic waves due to thermal conduction matches the observed values (Ofman and Wang, 2002). At the same time, for kink oscillations, theoretical and observed damping time roughly agree only for phase mixing (Ofman and Aschwanden, 2002).

Cirtain et al. (2013) observed flux tube braiding in the corona in EUV images, which has been confirmed via field extrapolations (Thalmann et al., 2014).

Aschwanden et al. (2000b, and references therein) reported that the power law for the flare frequency in dependence of the flare energy follows a slope of -1.8, too shallow for the nanoflare model to be sufficient for coronal heating. However, they compare their founding to similar surveys, some of them having even flatter slopes while other claiming a slope steeper than the required -2.

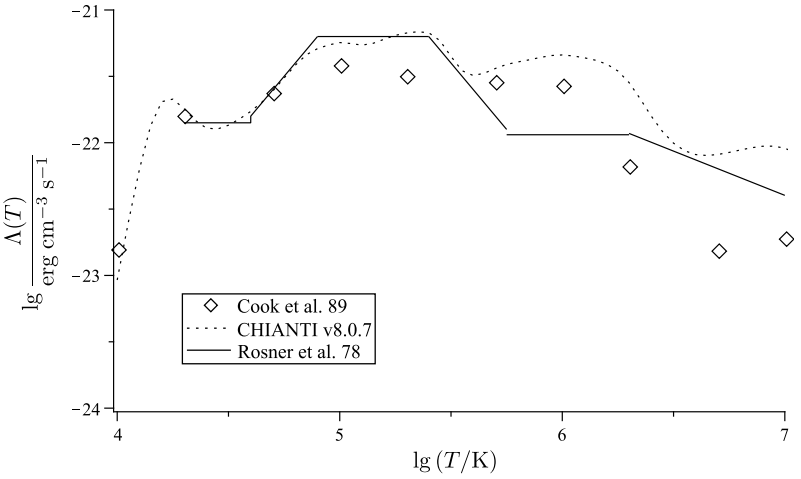

Figure 5.1: The radiative loss functions $\Lambda(T)$, as given by Rosner et al. (1978) and Cook et al. (1989) and computed with CHIANTI version 8.0.7 (Del Zanna et al., 2015) with the coronal abundances displayed in table 2.2

5.3 Coronal cooling

5.3.1 Radiative cooling

As mentioned in chapter 3, an important process for a coronal plasma of loosing energy is radiating EM waves due to bound-bound-transitions. The ions become excited by collisions with free electrons, draining their thermal energy. Besides this bound-bound emission, a free-bound continuum contributes in the EUV. Its emissivity is a factor of 100 lower than the line emissivity at 1 MK, but becomes significant at 10 MK and above (Golub and Pasachoff, 2010, sec. 3.3). The total power density ε_{tot} of these radiative losses is usually described by the product of the electron density n_e and the radiative loss function $\Lambda(T)$, which mainly depends on the electron temperature:

$$\varepsilon_{tot} = n_e^2 \Lambda.$$

The part of the radiative loss function which is caused by the bound-bound transitions is given in equations (3.1) and (3.2). This function can only be approximated for the corona.

Commonly used radiative loss functions are given by Rosner et al. (1978); Cook et al. (1989). It can also be generated from the CHIANTI database (Dere et al., 1997). These loss functions are plotted in figure 5.1.

5.3.2 Heat conduction

The heat conduction in a coronal loop is supported by the free electrons. The conductive losses are described as

$$\dot{U}_C = -\kappa_0 \partial_x \left(T^{5/2} \partial_x T \right)$$

as proposed by Spitzer (1962). The constant part of the coefficient of conductivity is $\kappa_0 \approx 10^{-6}$ erg s^{-1} cm^{-1} K$^{-7/2}$, but slightly varying values are used in literature since it depends on the plasma composition.

It must be noted that below around 20 000 K, in the transition region, this description of heat conduction breaks down. At such low temperatures, the ambipolar diffusion of atomic hydrogen becomes significant (Fontenla et al., 1990).

It has been recently found that in flaring loops, turbulence may significantly reduce the coefficient of heat conduction to

$$\kappa \propto n_e T^{1/2}$$

due to pitch angle scattering of the electrons (Kontar et al., 2014; Bian et al., 2016).

5.3.3 Mass flow

The exchange of mass between corona and chromosphere can significantly change the energy distribution. Especially the transition region can shift up- and downwards.

In case of *chromospheric evaporation*, chromospheric plasma becomes heated. The increased pressure compared to the corona causes an upflow of material into the corona, filling loops with plasma of 10^5 K up to 10^6 K. Such upflows can reach velocities of 100 km/s (for example, De Pontieu et al., 2011). The evaporation can be driven by direct heating of the chromospheric plasma, like in flares, or be the response of the plasma on coronal heating (Polito et al., 2018).

The *coronal rain* are plasma blobs of a few 100 km in size and around 10 000 K in temperature, i.e. far cooler than the corona. Condensed in loops not in thermal equilibrium, these blobs form a downflow from the corona to the chromosphere along field lines (Foukal, 1976, 1978; Antolin and Rouppe van der Voort, 2012).

If the pressures in the footpoints of a loop are different, this is balanced by *siphon flows*, where material moves in one direction along the entire loop.

Chapter 6

Inferring the physical conditions directly

Here we evaluate the possibility of inferring the physical properties of the coronal plasma from observations directly. The method is described in Aschwanden et al. (2008a).

In the procedure, a hose of points is wrapped around a loop. The central axis of the tube follows the loop. This loop is represented here by an extrapolated field line. The points on this central axis are spaced according to the pixel size. From each point on the central axis a perpendicular axis is extruded into both directions. The points on them are placed with the same spacing as on the central axis (figure 6.1). The DN values of the observed image are sampled on each of the points.

The perpendicular extensions are used to subtract the background of a loop. For each of the orthogonal axes it is assumed that the point on the central axis samples a part of the loop. So do the directly neighbouring points on the perpendicular axis, up to a certain width. The points further out are assumed to sample the background. A polygonal function is fitted to the DN values of the background points. The value of the fitted function at the locations of the loop points is then the background. Consequently, the remainder of the DN value at the loop points is interpreted as the contribution of the loop itself.

Once the background has been subtracted, the remaining emission of the loop in different filters can be used to infer the physical conditions along the loop. This can be done as described in the paper above, or by other implementations of the DEM analysis (like Kashyap and Drake, 1998; Hannah and Kontar, 2012; Del Zanna, 2013). Together with the 3D information of the field extrapolation, this would allow for the modelling of an entire AR in 3D when being applied to a set of field lines representative for the full AR.

6.1 Application to AR 11158

In Aschwanden et al. (2008a), the method is applied to well-isolated loops. For one of the loops, the authors are unable to find satisfactory results in one part. In the publication, this is explained by another loop crossing the first one in the images. However, we find out if we can apply the method to entire ARs near the disc centre, where such loop crossings are very common.

We apply the approach to a loop in the core of AR 11158, observed on February 14th, 2011 (figure 6.2). This loop has been chosen because it has a good visual match with an extrapolated field line in the western half of the field line. However, along the eastern half of the field line, no matching loop is, by eye, visible any more. Instead, other loops are crossing the field line. The western foot point is part of a bundle of foot points, which appear as an extended bright feature in the observations. The eastern foot point is clearly visible in the AIA 304 channel, though.

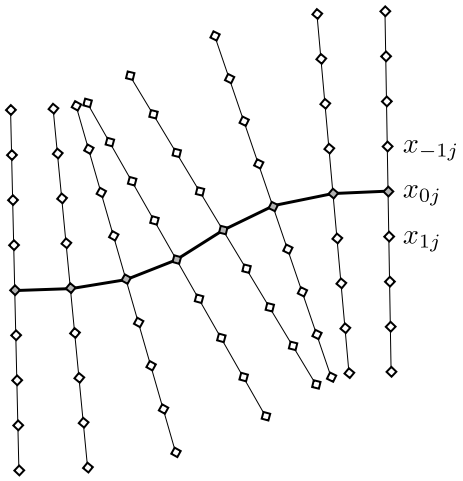

Figure 6.1: Placing of the sampling points. The extrapolated field line (thick line, with grey diamonds) defines the central axis. The perpendicular axes (thin lines with cupped diamonds) are extensions orthogonal to the central axis.

6.1.1 Background subtraction

For the background subtraction, the projection of the field line into the image plane serves as central axis. The width of extension to each side is $n = 4$ points, making up for a total of 9 points. Out of these, the three inner points are initially declared to belong to the loop and the remaining ones to the background.

We denote the perpendicular offset of the j-th node on the central axis with x_{0j}. The offsets of the points on the related perpendicular axis are denoted by x_{ij}, where i runs from $-n$ through n. It holds by definition

$$\begin{array}{rcll} x_{0j} & = & 0 & \forall\, j, \\ -x_{ij} & = & x_{-ij} & \forall\, j, \\ x_{ij} & = & x_{ik} & \forall\, i. \end{array}$$

At each of the points we take the local DN value from the observations. We fit a polynomial of 3rd order to the points, using a common polynomial regression. We define

$$\begin{aligned} \vec{z}_j &= \left(\{x_{ij} | \text{ node of index } i \text{ belongs to background}\}\right)^T, \\ \vec{y}_j &= \left(\{DN_{obs}(x_{ij}) | \text{ node of index } i \text{ belongs to background}\}\right)^T \end{aligned}$$

and

$$\mathbf{M} := \begin{pmatrix} 1 & z_{j,0} & \cdots & z_{j,0}^d \\ 1 & z_{j,1} & & z_{j,1}^d \\ \vdots & & \ddots & \vdots \\ 1 & z_{j,k-1} & \cdots & z_{j,k-1}^d \end{pmatrix},$$

where k is the number of points going into the regression and $d = 3$ is the degree of the fitted polynomial. The value $z_{j,l}$ is the l-th component of the vector $\vec{z}_j$. With these definitions, the $d+1$ -dimensional vector of regression-coefficients, $\vec{a}$ is computed by

$$\vec{a}_j = \left[\left(\mathbf{M}^T\mathbf{M}\right)^{-1}\mathbf{M}^T\right]\vec{y}_j.$$

Consequently, the background emission along the perpendicular axis of node j is now defined by

$$f_j(x) := \sum_{l=0}^{d} a_{j,l}\, x^l.$$

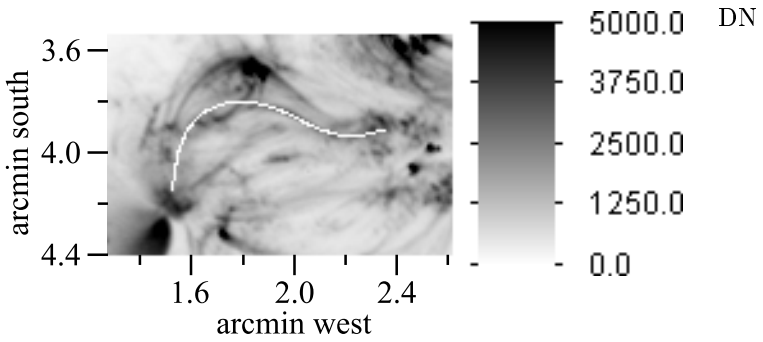

Figure 6.2: Region of interest with the loop analysed in this chapter, as seen in channel AIA 171. The field line used for the analysis is overplotted.

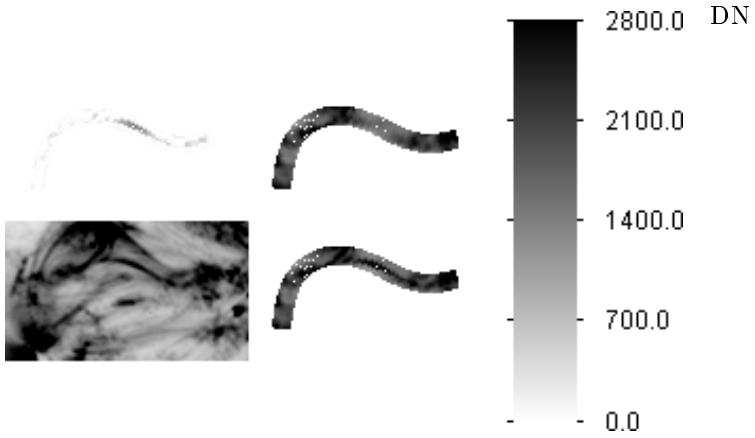

Figure 6.3: The analysed loop as seen in channel AIA 171. Bottom left: Observation, bottom right: sampled intensities, top left: computed loop intensities, top right: computed background intensities.

The emission from the loop at the sampling points follows then directly from

$$DN_{loop}(x_{ij}) = DN_{obs}(x_{ij}) - f_j(x_{ij}).$$

In case that the loop intensity turns out to be negative, f_j is recomputed with only the outermost two points on each side as background points (wider loop). If this does not cause the loop-intensity to become non-negative, a final attempt is made with all but the point on the central axis as background points (loop more narrow). If no positive loop emission is found then, the values are kept as they are. The loop is declared invisible at this location in the chosen filter.

6.1.2 Background-subtracted loop

Figure 6.2 depicts the loop with the projection of the field line over-plotted. Figure 6.3 shows the loop and its surroundings, the loop masked for the hose, and the computed background and loop intensities. For each perpendicular axis, the total intensity and the computed background intensity are plotted in figure 6.4 in sequence.

6.2 Discussion and conclusion

From figures 6.3 and 6.4 it is clear that the analysed loop can be detected only along roughly a quarter of the length of the field line in AIA 171. For the remaining parts of the field line, the total intensities and background intensities are close to each other, compared to the 28% error of AIA. For some nodes, the algorithm failed to find a proper background due to the low contrast, like at

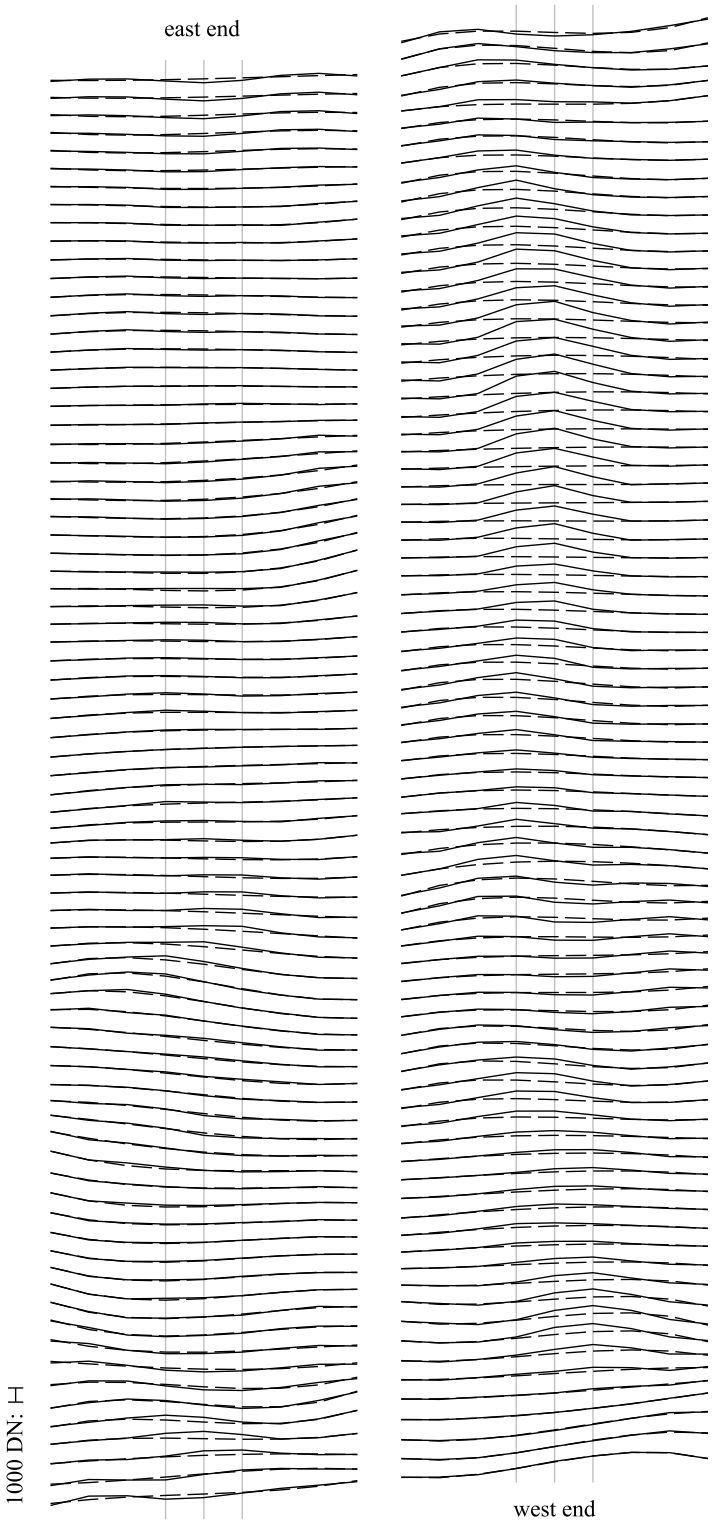

Figure 6.4: Observed total intensities (solid lines) and computed background intensities (dashed lines) for each perpendicular axis for the AIA 171 channel. The plots for each axis are displayed in consecutive order, split into two halves for reasons of spacing. The three grey, vertical lines denote the locations of the three central sample points on the perpendicular axes. The height of the bar in the lower left represents an intensity difference of 1000 DN.

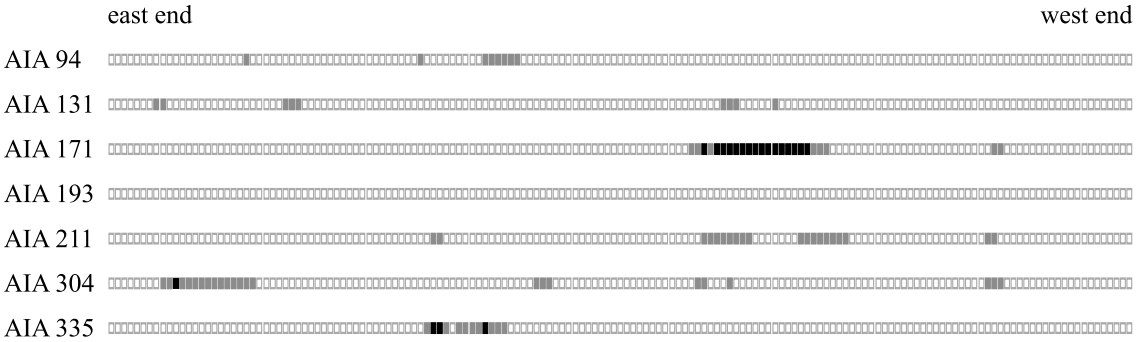

Figure 6.5: Categorized excess of total intensity relative to computed background intensity for each point on the central axis and for each of the seven AIA channels. Black squares: The total intensity exceeds the background intensity by at least 56% (twice the AIA calibration error). Grey squares: the total intensity exceeds the background intensity by at least 28% (once the AIA calibration error). Cupped, light grey squares: the total intensity exceeds the background intensity by less than 28%, or not at all.

the eastern end of the field line. Negative loop intensities were computed here, though lower than the observational error.

The situation is similar, or worse, in other channels. Figure 6.5 categorises how much the total intensity on each sampling point along the central axis exceeds the computed background intensity. The thresholds for the categories is the AIA calibration error of 28% (Boerner et al., 2012). A black square indicates that the total intensity at this point and in this channel exceeds the background intensity by at least 56%. A grey square indicates points where the total intensity is between 28% and 56% higher than the background. Points and channels where the total intensity is less than 28% brighter than the background are denoted by cupped squares. In the latter case, the loop is not significantly distinguishable from the background any more, or even invisible. As it can be read from the figure, this latter case is the main category for most points in any channel. For proper determination of the temperatures, the loop must be clearly visible in several channels.

Therefore, we conclude that inferring the physical conditions in loops in the centre of ARs with this method is impracticable. In this crowded part of the corona, loops are isolated far too rarely. The contrast required for the background subtraction is too low too often. Consequently, inferring the 3D atmosphere from multi-channel observations this way is not feasible, and other approaches are to be considered.

Chapter 7

Synthesizing AIA images based on loop models

The goal of this thesis is the determination of the physical conditions in an coronal active region in three dimensions, rather than yielding two dimensional projections. One way to achieve this is applying loop models to the field lines known from magnetic field extrapolations. Such models specify electron density, gas pressure and temperature on each point of each field line. Mathematically, they define functions

$$T(s),\ n(s),\ p(s)$$

on a given field line

$$\vec{r}(s),$$

where s is the loop coordinate, the distance to one footpoint measured along the loop, T, n and p are electron temperature, electron density and gas pressure, respectively, and $\vec{r}$ is the location in space.

The models can be tested by synthesizing satellite images from the model atmosphere and comparing these with actual observations. If the synthesized images are similar to the observations, this would be a strong hint that the model is correct, though it does not necessarily has to be. On the other hand, the model can be ruled out if the synthesized images differ strongly from the observations.

Having observations from multiple view directions at hand (like from the STEREO mission, Kaiser et al., 2008) is advantageous for this kind of analysis. Since it can be assumed that a model which successfully reproduces the observations from different perspectives simultaneously must be very close to reality.

A problem is the fact that the field lines are one dimensional curves in a three dimensional space. Therefore, an infinite amount of lines fit into a small but finite part. Due to the magnetic insulation between coronal loops the physical conditions might have discontinuities at the boundaries between two loops. On the other, hand the 3D model shall converge when more and more field lines are taken into account. Thus, a useful number of field lines accompanied by a suitable density of field lines has to be found.

In this chapter, the models are applied to AR 11158, which has been considered in chapter 6 already. The resulting synthesized images are compared against EUV observations from SDO/AIA.

There have been other works in the direction of forward modelling using 1D steady state models of loops. Lundquist et al. (2008a) published a forward modelling code that tries to fit X-ray observations of ARs. Their results matched better either to the observed temperature distributions of an AR (when applying loop top heating) or the observed morphology of the emission (when applying footpoint heating). They could not reproduce both at the same time, however. Warren and Winebarger (2006) could reproduce the X-ray AR, the resulting EUV emission failed to match the observation. Dudík et al. (2011) was able to match both X-ray and EUV with a steady state

	Field		Field
	Is it a closed line?	h_t	line top height
B_1	Footpoint A field strength	B_{max}	max field strength
B_2	Footpoint B field strength	B_{min}	min field strength
L	Field line length	B_t	field strength at top
x_1	Footpoint A location x	$\langle B \rangle$	mean field strength
y_1	Footpoint A location y	σ_B	standard dev. field strength
x_2	Footpoint B location x	s	loop coordinate
y_1	Footpoint B location y		

Table 7.1: Field line data stored for each grid point. The footpoint field strengths B_1 and B_2 refer to the photospheric field strength at the positive and negative polarity, respectively. The loop top field strength B_t is taken at the highest point of the field line.

model. This required them to have unstable loops in the AR which contradicted the steady state property of the model. All of these authors concluded that steady state models can explain X-ray observations to some extent, but not the EUV observations. Consequently, they proposed that the AR corona should be described with dynamic models.

These authors used potential field extrapolations to model the coronal field. The exception is the work by Lundquist et al. (2008a) who used a model which they label "quasi-force-free". Their model allows the α in equation (2.2) to vary between field lines, like a NLFFF model. Unlike these authors, we mainly use a NLFFF model, but also compare to other field models.

7.1 General processing pipeline

Since the models differ only in the assignment of the physical conditions along the loops, a general processing pipeline can be established. In this section we describe this pipeline, assuming that the magnetic field data has been generated before.

7.1.1 Dataset

The extrapolated magnetic field data are given in a regular computational box of $N_x \times N_y \times N_z$ grid points, determined by HMI resolution. The last value, N_z, refers to the number of grid points in altitude. On each point the magnetic field vector is specified. Since this resolution is given, it determines the density of the field lines taken for the model. No more information is gained when interpolating field lines from more points.

For each grid point, we call a field line tracer to determine the field line running through that point. All relevant field line data is then stored, resulting in a scalar grid of size $N_x \times N_y \times N_z \times N_B$, with N_B being the number of stored field parameters (listed in table 7.1). After this step, the model generates the physical conditions at each grid point. An image synthesizing routine generates AIA EUV images with a resolution of $N_x \times N_y$ then. These images have to be mapped to the higher resolution of AIA.

Often, models refer to the magnetic field strengths at the coronal footpoints of the loop, not the photospheric ones. Therefore, we can put the lower boundary for the field line data computation to any horizontal layer of the field grid. The field lines are computed only from grid points in this layer and above. The resulting field lines are truncated where they cut the settled lower boundary. The footpoint locations and footpoint field strengths are taken at these truncation points. All data below the lower boundary are ignored for any further computation with this field model. Setting the lower boundary to $z = 0$, the lowest layer of the field grid, therefore includes all data. Within this frame, a loop is considered as "closed" when both ends are located in the lower boundary layer. Likewise, a field line with at least one end on any of the remaining five facets of the computational domain is labelled "open".

All this data is specific to the magnetic field only. Once computed, it can be used to any of the loop models. The computation time can significantly be reduced this way.

7.1.2 Modelling the loop

In the next step, the physical conditions at each grid point are determined on the basis of the chosen model and the magnetic field data. This requires a specific loop model, hence we go into details here in the following sections.

7.1.3 Synthesizing AIA images from the modelled active region

From the modelled physical data we synthesize observations by AIA in the line of sight, the z view, as well as the x and y view. To do so, we use equation (4.1):

$$p_f = \int\limits_{pixel} \int\limits_{0}^{\infty} K_f \cdot DEM \; dT \; d\omega,$$

where the flat-field value F has been set to 1 now since we want to compare our synthesized images to flat-field corrected observations.

For the image synthesising, we divide the volume into regular, cubic cells, with the grid points being located in the centre of the cells. Thus, the facet area of a cell covers a pixel, causing

$$\int\limits_{pixel} d\omega = 1.$$

The plasma in a cell may have the density stored on its grid point. A slope for the temperature is computed from the temperatures of the adjacent grid points above (subscript $+$) and beneath (subscript $-$) by the central difference

$$m := \frac{T_+ - T_-}{2d}$$

with d being the grid spacing. At the top and the bottom layer, a one-sided difference is used. This yields a constant DEM, and the DN originating from the cell is then

$$p_f = \int\limits_{T_{low}}^{T_{up}} \frac{R_f n^2}{m} dT.$$

The boundary temperatures are derived from the temperature T of the cell and the slope by

$$T_{up,low} = T \pm \frac{d}{2} m$$

In case the slope is too shallow ($|T_+ - T_-| < 10^{-10}$ K), we can use the isothermal approximation (4.2)

$$p_f = n^2 K_f(T) d.$$

The resulting images are of the HMI resolution (about 720 km) since they are based on the magnetic field data. However, AIA has a higher resolution (about 450 km) and the observed regions are of slightly rectangular shape rather than the quadratic shape of the numerical box. Therefore, we have to map the previously synthesized images onto AIA resolution. In this step we also add an approximated correction for the small angle between the LOS and the z direction of the numerical grid, which is normal to the local solar surface. This tilt angle is very low since the observed ARs are near the centre of the solar disc.Because the observed region is not located directly on the disc centre the angle does not vanish, though.

The mapping is sketched in figure 7.1. First, we construct a rectangular image array representing the part of the AIA images with the region of interest. The pixels within this image are initialized with 0 DN, i.e. completely dark. We then take the $N_x \times N_y \times N_z$ numerical box with

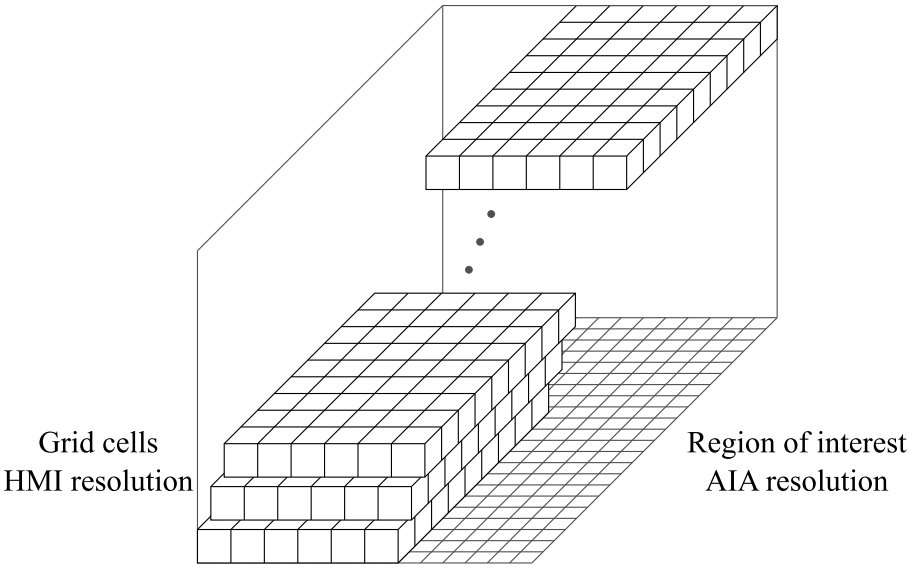

Figure 7.1: HMI to AIA mapping.

the emitting grid cells and place the entire box into the corner of the image array that is closest to the disc centre. Beginning with the second lowest layer, each cell layer is then shifted towards the opposite corner. This shift increases linearly with altitude in a way that finally the topmost layer is located exactly in the corner farthest away from disc centre.

Finally, the DN values of the grid cells are projected onto the pixels of the image array. This is, if a pixel of the image covers a fraction of f of the bottom surface area of a grid cell, f times of the cells DN is added to the pixels DN value. The result is an synthesized AIA image.

7.2 The RTV 78 model

7.2.1 The model

Rosner et al. (1978, in the following RTV78, from Rosner, Tucker and Vaiana) suggested a first, one-dimensional and static model for a coronal loop. They assumed that the loop is semi-circular and vertically inclined towards the photosphere. In their model the authors describe the energy balance within the loop. They neglect all energy transfer across boundaries (particles are bound to magnetic field lines due to Lorentz force) and the footpoints of the loop (inefficient heat transport at low temperatures) and assume that no flows are present within the loop. Thus, energy is added to the system only by an unspecified heating function whose power density depends on the position along the loop. Loss of energy occurs by radiative cooling only, for which the authors give a function depending on the temperature in their publication (plotted in figure 5.1). Additionally, heat transport by diffusion is included, using the non-linear, temperature-dependent diffusion coefficient found by Spitzer (1962, see section 5.3.2).

The authors also point out that their analysis is valid only for low loops since they assume a constant pressure along the entire loop. Nevertheless, results from the RTV78 model (see below) have widely been applied to other loops over the past as well, or used as a reference at least.

In general, the model described by RTV78 fulfils the equation (in cgs units)

$$0 = E_H + \Lambda(T) - \partial_s \left(\kappa_0 \cdot T^{5/2} \partial_s T \right), \tag{7.1}$$

where $\kappa_0 = 10^{-6}$ erg cm^{-1} s^{-1} K$^{-7/2}$ is the constant part of the diffusion coefficient, E_H the heating function and Λ the radiative loss function, the only measure in the equation which is not explicitly spatially dependent.

The authors point out several relations between pressure, temperature, heating, loop size, magnetic field, and characteristic time scales and lengths for different models of heating. The model which is usually referred to as *the RTV78 model* is the special case of a constant heating along the loop. In this case RTV scaling laws

$$T_{max} = 1.4 \cdot 10^3 \ \frac{\mathrm{K}}{(\mathrm{dyne/cm})^{1/3}} \ (pL_{half})^{1/3}, \tag{7.2}$$

$$E_H = 9.8 \cdot 10^4 \ \frac{\mathrm{erg}}{\mathrm{s\ cm^{3/2}\ dyne^{7/6}}} \ \frac{p^{7/6}}{L_{half}^{5/6}} \tag{7.3}$$

can be derived. Here, T_{max} is the maximum temperature which is reached at the loop top and L_{half} is the loop semi-length. For this case the temperature T in dependence of the loop coordinate x is also explicitly given by the authors using the inverse expression

$$x(T) - x(T_0) = \frac{2.5 \cdot 10^5}{p} \left[9.6 \cdot 10^{-16} T_{max}^3 \left(1 + \arcsin\left(\frac{T}{T_{max}}\right) - \left(\frac{T}{T_{max}}\right) \sqrt{1 - \left(\frac{T}{T_{max}}\right)^2} \right) \right]. \tag{7.4}$$

In this formula, T_0 expresses the footpoint temperature which the authors set to 20 000 K. At T_{max}, $x(T_{max}) = L_{half}$ holds by design. The units are cgs units again, and the units of the constants are such that the equation is in cm. We dropped the units of the constants here for convenience, as the equation is already lengthy.

We also employ the RTV78 model, with constant heating, for our modelling. However, equation (7.4), together with (7.2), leaves one free parameter, either the pressure p or the peak temperature T_{max}.

7.2.2 Implementing the RTV78 model

When implementing the RTV78 model, we tackle the problem by using two different equations which have been found by other authors before and which link p or T_{max} to the magnetic field strength. First, we apply a scaling by Golub et al. (1982) which claims that

$$p \approx \frac{63\ \mathrm{dyne}}{\mathrm{cm^{7/4}\ Gs^{3/2}}} \ B_z^{3/2} L^{-1/4}. \tag{7.5}$$

Second, we use a finding made by Schrijver et al. (2004),

$$F_H \approx 4 \cdot 10^{14} \ \frac{B}{L} \ \exp\left(- \left(\frac{B}{500\ \mathrm{Gs}} \right)^2 \right), \tag{7.6}$$

$$T_{max} = \ (F_H L_{half})^{0.3} \ \exp\left(\frac{L_{half}}{9.4 \cdot 10^{10}\ \mathrm{cm}} \right) \tag{7.7}$$

for a pressure scale height of $4.7 \cdot 10^9$ cm (corresponding 1 MK). The measure F_H, in erg cm^{-2} s^{-1}, is the energy flux through a footpoint of the loop. Additionally, we apply the models to three different field extrapolations, a potential field, a LFFF with $\alpha = 2$ and a NLFFF (fig. 2.5).

Once pressure and temperature are known, the density is derived from the equation of state

$$p = 2nk_BT \tag{7.8}$$

with the Boltzmann constant k_B.

The RTV78 model assumes the loop to be symmetric. This is usually not the case for our model loops, as the different magnetic field strengths at the two foot points, together with the two scalings above, cause two different solutions for the model loop. For merging these solutions, we average them at each point with a weight equal to the relative distance between the point and

the foot points. For example, for the pressure p, which may be determined to p_1 and p_2 at the footpoints, the value at each location x along the loop would be

$$p(x) = \frac{x}{L} p_2 + \left(1 - \frac{x}{L}\right) p_1,$$

where x is the distance along the loop to the footpoint where the field strength yields the pressure p_1 and L is the total length of the loop. This way it is guaranteed that, at both footpoints, the solution there is the one that belongs to the footpoint, while at the same time the solution smoothly transits from the one to the other along the loop.

The model RTV78 + Golub et al., 1982

In this model, we use equation (7.5) to derive the pressure p from the input vector magnetogram. For a certain field line, this magnetogram is bi-linearly interpolated at the location of the footpoints. By inverting equation (7.4) numerically, we can determine the temperature along the loop, and hence for the grid point the field line is extrapolated from.

The model RTV78 + Schrijver et al., 2004

Here, the loop top temperature T_{max} is deduced from the vector magnetogram via equation (7.7). The relation (7.4) yields the pressure then when being evaluated at the loop top, $x = L/2$, where $T = T_{max}$ holds. Equation (7.4) is then used for computing the temperature at the grid point from which the field line has been extrapolated.

7.2.3 Error estimation for the model RTV78 and Golub et al., 1982

The estimation of the errors is a bit tricky. Errors taken into account are caused by measurement errors of the footpoint field strength, of the length of the field line and of the loop coordinate of the point of interest.

Strictly speaking, this error estimation is a highly non-linear problem. Two field lines with footpoints very close to each other at one end can connect two completely different, well separated regions. A slight change in the vector magnetogram, within the measurement errors, can shift the topological boundary between the field lines. Both field lines would connect to the same region then, after one line experience a drastic change, possibly with the length varying by a factor of ten or so.

Such a treatment of the errors is infeasible. We approximate the errors numerically instead. We define a four-dimensional error grid by any combination of a set of given values in B_z for the one foot point, B_z for the other foot point, L and s. The values span the entire expected parameter space. Also, errors for these input parameters are defined on the error grid points (table 7.2). For each of the error grid points we compute errors in T, p and n resulting from the model RTV78 + Golub et al. (1982).

To demonstrate the error estimation, we arbitrarily choose generic values for the relative errors. It is pointed out in this section that the models do not perform well enough for an estimation with realistic values to be necessary. The errors in the magnetic field are chosen to be 10%. The exception is the 1 Gs error grid point, where the error is 100%, accounting for the low signal. The lengths L and s are assumed to be more precise, thus those errors are set to 1%. This cannot account for the extremely non-linear topological errors mentioned above, which are ignored as they are difficult to handle. These errors allow for a error estimation in a first place, and allow for working with the error computation code at all. We will see why it is not necessary to become more precise with the error handling. For a certain error grid point in the parameter space, we computed 2000 realisations of (B_{z1}, B_{z2}, L, s), where each input parameter is randomly determined with a Gaussian distribution with the mean being the pre-specified value at the grid point and the pre-defined error as the standard deviation. The errors are computed from the resulting standard deviations. This is repeated for all of the grid points.

B_z [Gs]:	1	10	20	50	100	200	500	750	1000	1250	1500
ΔB_z [Gs]:	1	1	2	5	10	20	50	75	100	125	150
B_z [Gs]:	1750	2000	2250	2500	2750	3000					
ΔB_z [Gs]:	175	200	225	250	275	300					
$\lg L/\mathrm{Mm}$:	0	0.5	1	1.2	1.4	1.6	1.8	2	2.2	2.4	2.6
$\Delta L = 10^{-2}L$											
s/L	0.1	0.2	0.3	0.4	0.5						
$\Delta s/L = 10^{-2}s/L$											

Table 7.2: Parameter space for error calculation in the RTV78 models.

For a certain field line in the model, the errors are quadri-linearly interpolated from the error grid then.

7.2.4 Results of the RTV78 model

From the computed model atmosphere, artificial observations are synthesized. These are compared to the real observations. Additionally, maps of the computed physical parameters are drawn.

The model RTV78 + Golub et al., 1982

Figure 7.2 shows the synthesized LOS images in the AIA 171 channel for the three magnetic field models, along the observations. The lower boundary is the lower boundary of the box at $z = 0$. Figure 7.3 displays the same, just with the lower boundary set to $z = 5$, i.e., the lower five layers are ignored. In both figures, the synthesized images are once displayed with the colour bar ranging from the minimum intensity to the maximum intensity, once in the same colour scaling as the observations.

NLFFF model It must be pointed out that the model includes only closed field lines, as the model describes only closed loops. The fans of loops leaving the observational image cannot be reproduced because of this. In the centre of the images for the *NLFFF*, a bright structure in east-west-direction can be seen in the synthesized images. There are some loops in this location in the observations, though slightly differently orientated. In other channels, like AIA 94, this structure is brighter in the observations relative to the rest of the image, and the similarity to the synthesized image is somewhat larger. The misalignment remains, however. To the south-east of this, an arcade of loops can be detected in the observations. This arcade is also present at least in the $z = 0$ - synthesized image, though with the individual loop having much less contrast. The faint lobe of emission in the southern half is present in all channels and in both observations and synthesized images, which makes it the probably best reconstructed feature of the AR on a qualitatively level. Nevertheless, individual loops have few contrast, if any, in the synthesized images, contrary to the observations. The lobe of emission in the north ranges from the western to the eastern polarity in the synthesized images, while in the observations the western polarity seems to be connected to the centre of the AR. In general, the loops display much more contrast in the observations, while the synthesized images show a rather smooth haze. A moss pattern (Fletcher and De Pontieu, 1999) is visible in the observations. Since moss is a transition region phenomena, it is questionable if the coronal loop models can reproduce it at all. The missing of the moss in the synthesized images is, therefore, not a problem.

The most striking difference between the synthesized images and the observations is that the synthesized images are too bright by orders of magnitude.

The other channels allow exactly the same conclusions to be drawn. For this reason, we restrict on showing the 171 channel. The model reproduces the observations very poorly on a qualitative level, and not at all on a quantitative level. From the points mentioned above, only the loop contrast can be improved by applying physical arguments. Loops rooted in the umbra of a sun

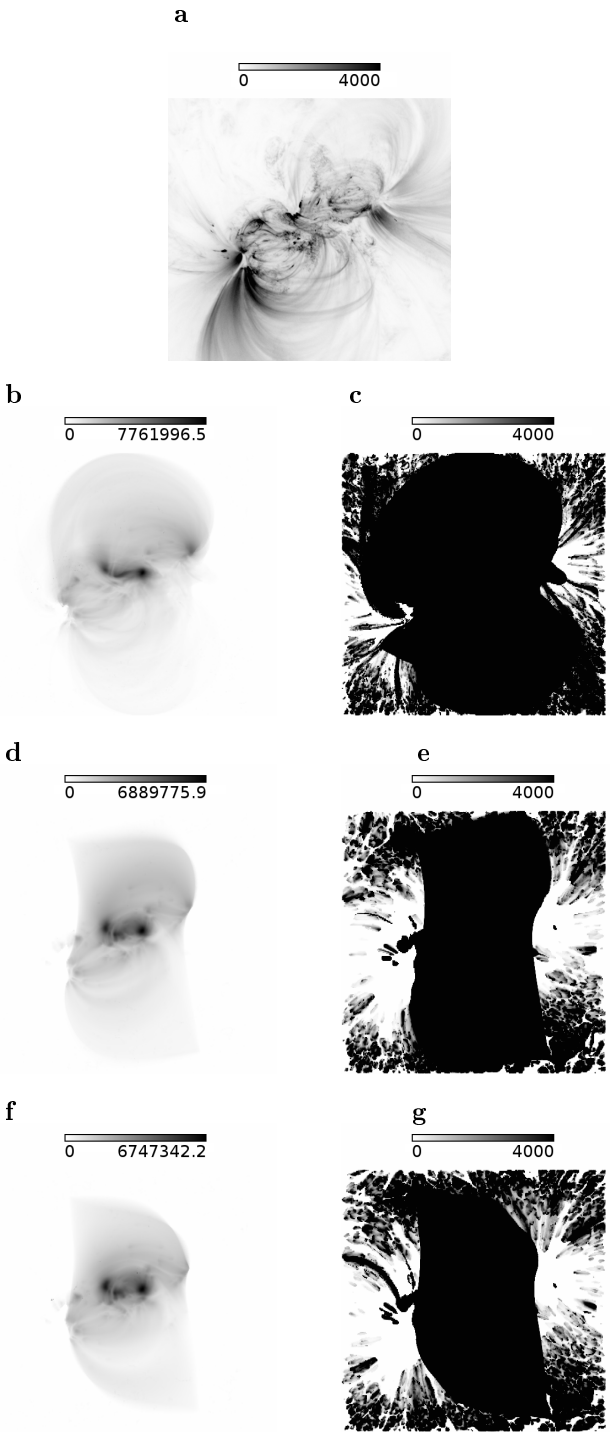

Figure 7.2: Observations of AR 11158 made by AIA 171 at Feb 14th, 2011 (a). Synthesized AIA 171 images from the model RTV78 + Golub et al. 82: NLFFF model (b and c), LFFF model with $\alpha = 2$ (d and e) and potential field model (f and g). Colour scaling is either from minimum to maximum intensity (b, d and f) or the same as in the observations (c, e and g). In the latter case, the images are heavily overexposed.

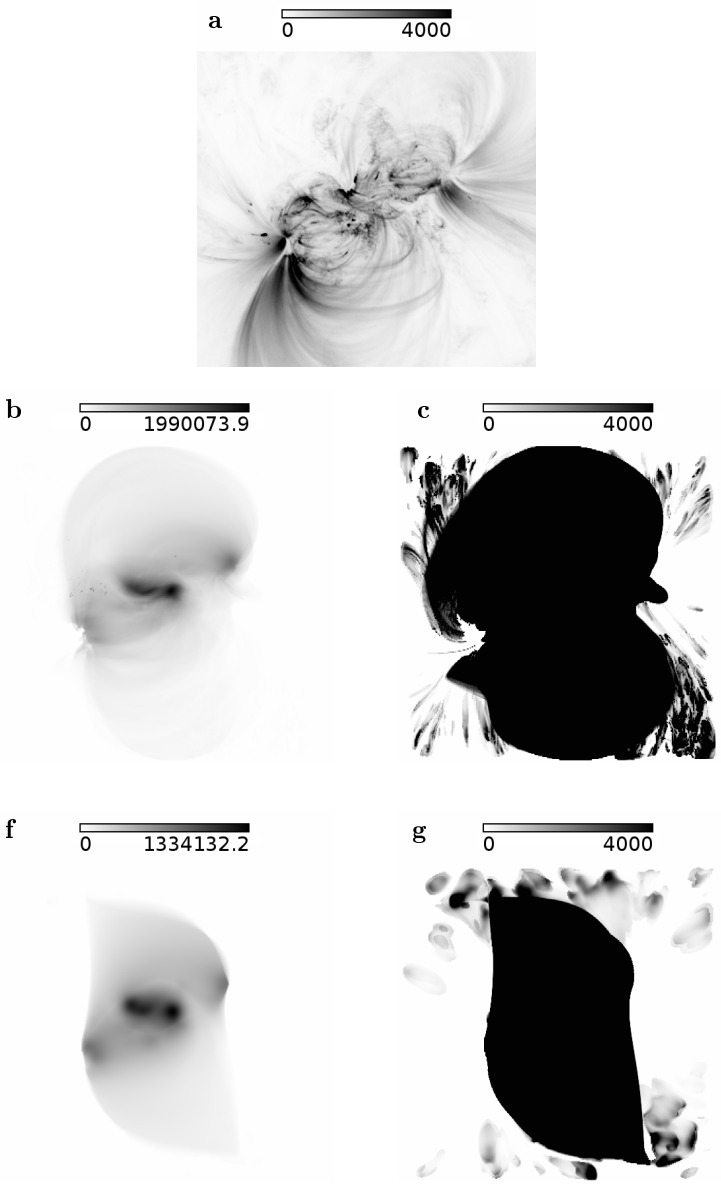

Figure 7.3: The same as in figure 7.2, just with an elevated lower boundary set to $z = 5$ instead of $z = 0$. Since there was no need to compute the results for the LFFF any more, these images are missing here. The labelling from figure 7.2 has been kept, though. Again, the synthesized images are overexposed when displaying them in the same colour scale as the observations.

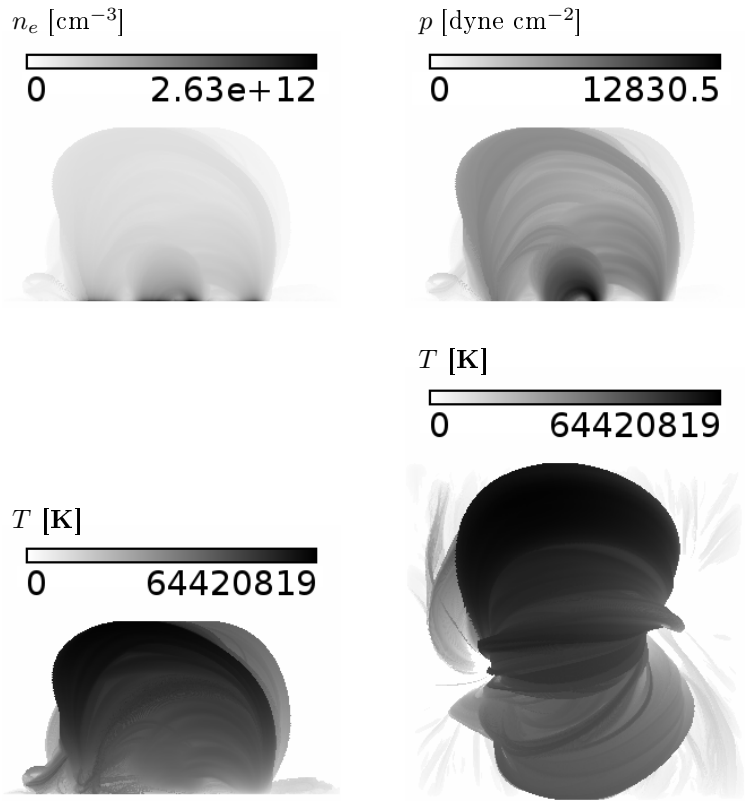

Figure 7.4: Physical conditions in the model atmosphere resulting from RTV78 + Golub et al., 1982, with the NLFFF and the lower boundary set to $z = 5$. Displayed maximum of the density, the pressure the temperature, respectively. The lower right picture has the same LOS as the observations. All other pictures feature a horizontal view from south to north.

spot are barely heated and, thus, invisible in X-ray and EUV (Bray et al., 1991, sec. 2.4.3 & 2.5). Figure 7.5 displays the same model, but now with all model loops removed that have footpoint field strengths above 500 Gs at both of the footpoints. Loops are distinguishable now, but the AR is still not reproduced neither qualitatively nor quantitatively.

The maximum of the density, pressure and temperature for a horizontal view from south to north are shown in figure 7.4. For the temperature, this is also plotted for the top-down view known from the synthesized images. The values are from the model using the NLFFF and having the lower boundary set to $z = 5$. As it can be read from the figure, all physical quantities are too high. The density is mostly a few 10^{11} cm^{-3} instead of $\approx 2 \cdot 10^9$ cm^{-3}. The pressure, which should be around unity in this unit, is a few thousand dyne cm^{-2} and the temperature is several 10 MK, temperatures which can barely reached by a flare. Together with the mismatching synthesized images, their brightness being caused by the high densities, this mismatch in the physical parameters of the coronal plasma strongly speaks against the model.

For the lower boundary set to $z = 0$, the computed errors basically follow the pattern of the computed values, i.e. the highest absolute errors can be found where also the highest values can be found. For the density, the errors reach up to $1.6 \cdot 10^8$ cm^{-3}, four orders below the absolute values. The pressure displays errors of about 10%. The errors in the temperatures go up to just roughly 2000 K, again between four and five orders of magnitude lower than the absolute values. Relative to the computed physical conditions, the absolute values of the errors are of similar size when setting the lower boundary to $z = 5$.

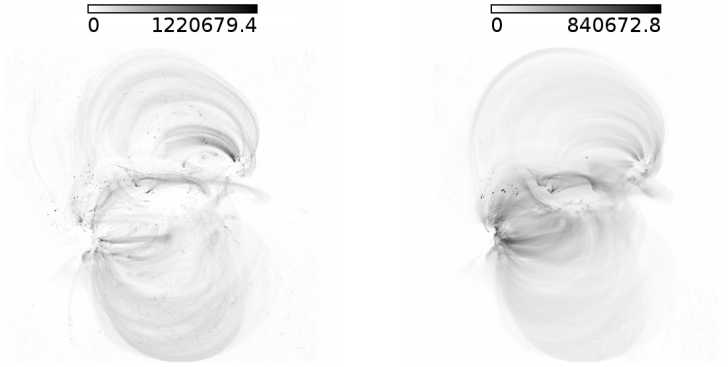

Figure 7.5: The RTV78 + Golub et al., 1982 model and a NLFFF, but without the emission from loops that are rooted in regions of at least 500 Gs with both foot points. Left: Lower boundary set to $z = 0$, right: lower boundary set to $z = 5$.

LFFF model and the potential field model The results are not better for the other magnetic field models. Contrary, while the NLFFF reveals at least a somewhat "organic" structure as known from real ARs, the shapes of the synthesized ARs for the LFFF and the potential field are very smooth, like the flame of a candle in non-moving air. We conclude that the type of the field model, non-linear or not, does play a strong role, and a NLFFF model yields results closer to observations. This is contradicting the postulations by Dudík et al. (2011) who did not see much of a difference between NLFFF and potential field, but agrees with Warren et al. (2018) who proposed that a NLFFF agrees best with observed loops.

Modified pressure scaling A way to deal with the quantitative problems of the model is to modify the pressure scaling (7.5) by additionally dividing the right hand side by 1000. This is an empirical estimation made from the results with the unmodified scaling. It is a constant factor which, qualitatively, does not matter much: it can be adjusted to whatever value fits best. The important point is that the dependency on B_z and L remains unchanged.

Figure 7.6 depicts the synthesized images for this modified RTV78 + Golub et al., 1982 model, with the NLFFF and the lower boundary set to $z = 5$. While the centre remains overexposed, the outer parts of the synthesized AR have an intensity similar to the observations. Figure 7.7 shows the maximum of density, pressure and temperature for each LOS in a horizontal view in north-south direction, as well as the maximum temperature in the top-down view. Compared to the unmodified pressure scaling, the physical parameters are in a range now which is expected for an AR corona. Still, the hottest part in the synthesized atmosphere is still not the core of the AR. The relative errors are about 10^{-5} for the density, 0.1 for the pressure and 10^{-4} for the temperature.

By adjusting the factor the pressure scaling is modified, the quantitative matching of the synthesized images to the observations can surely be improved further. However, since the qualitative matching is still poor, we do not make the effort and rule the model out instead.

RTV78 + Shrijver et al., 2004

Figure 7.8 shows the synthesized AIA 171 images for the combination of the RTV78 model with the maximum temperature following from equation (7.7). The underlying magnetic field is the NLFFF and the images are for both the lower boundary set to $z = 0$ and $z = 5$. For the latter one, also the maximum pressures and densities along the line of sights are displayed.

The loop structure is more prominent here compared to the smooth "haze" of the RTV78 models. An additional masking of loops anchored in regions of strong magnetic fields is not necessary since the Shrijver-scaling has such scaling implemented. Though the synthesized images are clearly different to the images from the other RTV78 models, the AR is still not reproduced in a geometric

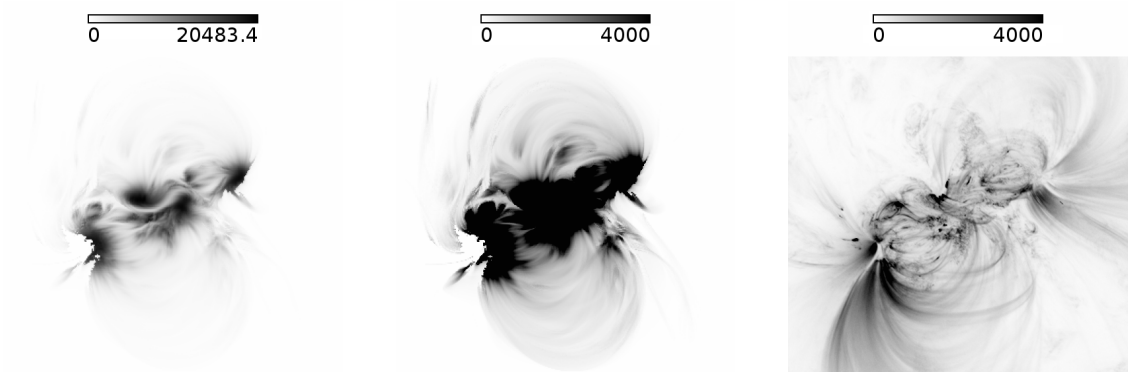

Figure 7.6: Synthesized AIA 171 images for the *modified* RTV78 + Golub et al., 1982 model. The field model is the NLFFF, the lower boundary is set to $z = 0$. Left: Colour scaling from 0 DN to maximum. Centre: colour scaling as in the observations. Right: AIA 171 observations.

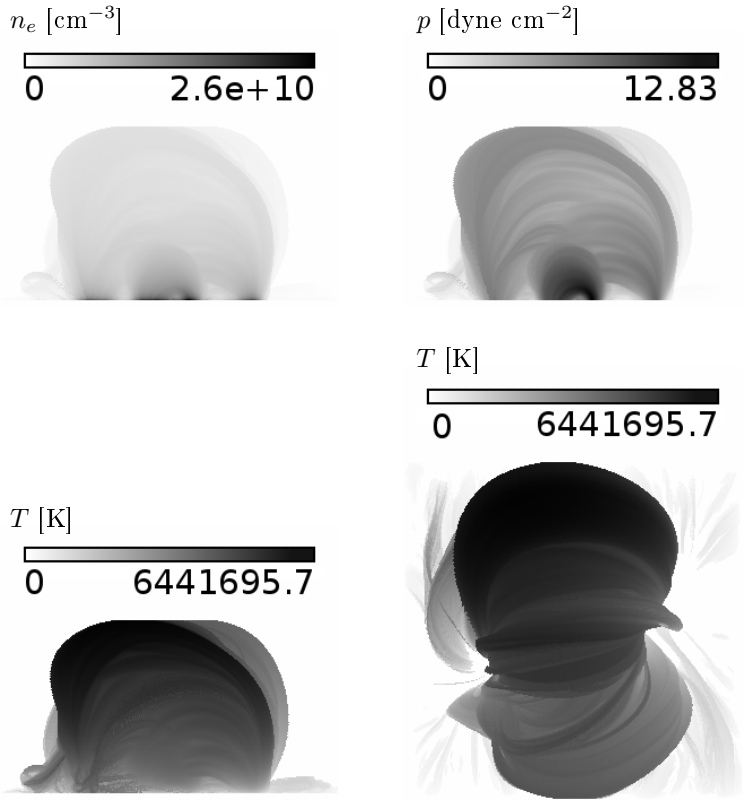

Figure 7.7: Physical conditions in the model atmosphere resulting from RTV78 + *modified* Golub et al., 1982, with the NLFFF and the lower boundary set to $z = 5$. Displayed are the maximum of the density, the pressure the temperature, respectively. The lower right picture has the same LOS as the observations. All other pictures feature a horizontal view from south to north.

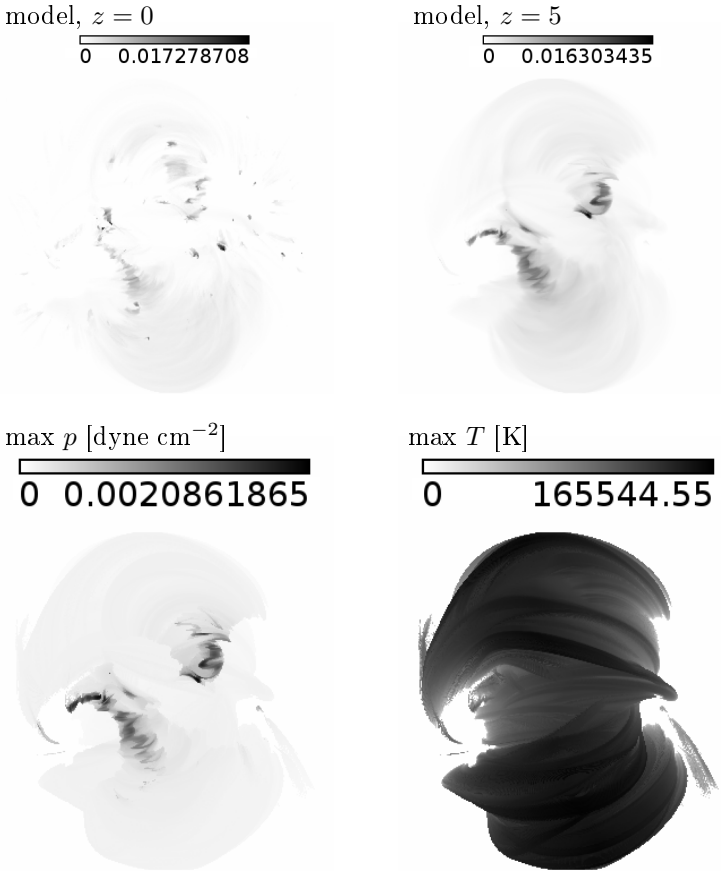

Figure 7.8: Results from the model RTV78 + Shrijver et al., 2004, with NLFFF. Top row: AIA 171 images synthesized when lower boundary is set to $z = 0$ and $z = 5$, respectively. Bottom row: maximum pressure and temperature along the LOS for the model where the lower boundary is at $z = 5$.

sense. The temperatures are in the same range as for the Golub-scaling, i.e., far too high. The densities and the pressures, on the other hand, are three orders of magnitude below what is to be expected in an AR. Consequently, the synthesized intensities are six orders below the observed value.

Deviating from correct physical values so much, the model RTV78 + Shrijver et al., 2004 has to be rejected, too.

7.2.5 Conclusion

For the RTV78 model with both of the scalings, (7.5) and (7.7), the purely geometrical appearance of the AR in the synthesized images cannot capture the observed AR at all. Additionally, the scaling had to be changed for the results being in a proper physical range. In case of the Golub-82-scaling, the emission from loops anchored in regions of strong magnetic fields has to be filtered out. Otherwise they would contribute as a smooth "haze", causing the loops to have negligible contrast to each other. We decide to reject the computed RTV78 models.

The NLFFF produces model-ARs with an organic shape. The ARs modelled on the basis of a potential field or an LFFF have a rather straight, more artificial-looking shape, somewhat reminiscent to the flame of a candle. From this we can at least conclude that the NLFFF is a better approximation to the real coronal field, and should be preferred over the other two field models.

We also lined out how an error estimation can be performed. With our estimation of the errors, they are quite small. Here, we used some typical values as input to demonstrate how the estimation

works. A more rigid estimation, using more precise values is straightforward. However, it is also not feasible here, as the models do not produce satisfactory results to begin with.

7.3 The Serio model

The model published by Serio et al. (1981) is an extension of the RTV78 model. Compared to the older model, it relaxes some of the assumptions made. In the Serio model both the pressure and the heating may decay exponentially in altitude with scale heights s_p and s_H, respectively. As a consequence, the authors distinguish two categories of loops which they call *class I loops* (with maximum temperature at loop top, like in RTV78) and *class II loops* (with a local temperature minimum located at the top, in contradiction to RTV78).

For the class I loops the authors provide some scaling laws:

$$T_{max} \approx 1400 \left(p_0 L_{half}\right)^{1/3} \exp\left(-\frac{0.08\ L}{s_H} - \frac{0.04\ L}{s_p}\right), \tag{7.9}$$

$$E_0 \approx 10^5 p_0^{7/6} L_{half}^{-5/6} \exp\left[L_{half}\left(\frac{1}{s_H} - \frac{1}{s_p}\right)\right]. \tag{7.10}$$

The values p_0 and E_0 are the pressure and the heating rate at the foot point. The pressure scale height is dependent on temperature and can be set to $s_p = 47$ m/K T_{max}, a common value (like in Serio et al., 1981). For solving the equation for T_{max} now, the principal branch of the Lambert-W function, W_{L} (Oliver, 2010), is required:

$$T_{max} \approx -\frac{0.04\ L_{half}}{47\ W_{\mathrm{L}}\left(-\dfrac{0.04 L_{half} \exp\left[0.08 L_{half}/47\right]}{47\left(p_0 L_{half}\right)^{1/3}}\right)} \tag{7.11}$$

7.3.1 Numerical approach

Unlike for the RTV78 model, there is no equation for $T(s)$ for the Serio model. Instead, we have to compute the temperature numerically. For a stationary solution, the temperature has to fulfil equation (7.1) again. We iteratively converge the temperature to a stationary state using a solver for the equation

$$d_t f(x) = \kappa d_x \left(f^\gamma d_x f\right) + S(f), \tag{7.12}$$

where S is the source term, in our case $E_H + \Lambda$. The non-linear diffusion term is treated by the transformation

$$dg := \kappa f^\gamma df. \tag{7.13}$$

This is described in Press et al. (1992) for homogeneous differential equations, but the approach can easily be extended to inhomogeneous ones. We use a backward-Euler scheme with a grid spacing of Δx, a step size of Δt and using the one-sided forward differentiation in time and the standard Δx^2 $[1\ -2\ 1]$ $/\Delta t$ differentiation for the second derivative. Eventually, this allows for describing an iteration step as followed.

We define the matrices

$$\mathbf{A} := \begin{pmatrix} -2\left(f_0^n\right)^\gamma & \left(f_1^n\right)^\gamma & & & 0 \\ \left(f_0^n\right)^\gamma & -2\left(f_1^n\right)^\gamma & \left(f_2^n\right)^\gamma & & \\ & \ddots & \ddots & \ddots & \\ & & \left(f_{N-3}^n\right)^\gamma & -2\left(f_{N-2}^n\right)^\gamma & \left(f_{N-1}^n\right)^\gamma \\ 0 & & & \left(f_{N-2}^n\right)^\gamma & -2\left(f_{N-1}^n\right)^\gamma \end{pmatrix},$$

$$\mathbf{B} = \mathrm{Diag}\left(\frac{dS_0^n}{df}, \ldots, \frac{dS_{N-1}^n}{df}\right),$$

$$\mathbf{C} := \left(\frac{\Delta x^2}{\kappa \Delta t} \mathbf{1} - \mathbf{A} - \frac{\Delta x^2}{\kappa} \mathbf{B} \right),$$

and

$$\mathbf{D} := \left(\frac{\Delta x^2}{\kappa \Delta t} \mathbf{1} + \left(\frac{1}{\delta} - 1 \right) \mathbf{A} - \frac{\Delta x^2}{\kappa} \mathbf{B} \right),$$

with $\mathbf{1}$ being the unit matrix. The iteration step from time n to time $n+1$ for the vector of the sampled values of f is then

$$\mathbf{C} \vec{f}^{n+1} = \mathbf{D} \vec{f}^{n} + \frac{\Delta x^2}{\kappa} \vec{S}^{n}.$$

The code requires boundary conditions which define an f_{-1} and an f_N. These two values are missing in matrix $\mathbf{A}$, but have to be included for the computation of the second derivative on the two most outside points. When f_{-1} is expressed by a linear combination of f_0 and f_1, and f_N is expressed by a linear combination of f_{N-2} and f_{N-1}, this can easily be adopted in the first and the last row of $\mathbf{A}$, without destroying the tri-diagonal structure.

7.3.2 Infinite heating scale height

In the case of infinite heating scale, the Serio-model has the uniform heating in common with the RTV78 model. The main difference here is that the pressure is not constant in altitude.

Temperature profiles

We computed the temperature profiles for the typical parameter space of coronal loops (table 7.3), with a total of 51 profiles. For a base pressure of $p_0 = 0.1$ dyne cm $^{-2}$, we did not compute profiles for 5 Mm and longer, as the very low temperatures cause very short pressure scale heights. The long loops are basically empty in the top.

For the computed profiles, the maximum temperatures are between 5% below and 17% above the theoretical values following from equation (7.11). Generally speaking, the lower the base pressure and the longer the loop is, the higher is the maximum temperature of the profile relative to (7.11). This shows that our numerical profiles match the estimations made by Serio et al. (1981). Nevertheless, equation (7.9) for the maximum temperature is the equation from RTV78, eq. (7.2), multiplied by a factor. After carefully inspecting our temperature profiles, we find the maximum temperature to be represented better by the following, empirical approximation which is explained in figure 7.9:

$$T_{max} \approx 1390 \left(p_0 L_{half} \right)^{1/3} \cdot y(L_{half}, p_0) \tag{7.14}$$

with the factors

$$y = A e^{-B(L_{half} - L_1)}, \tag{7.15}$$

$$A = \left(y_{1p} - y_{11} \right) \frac{p_0 - p_1}{p_2 - p_1} + y_{11}, \tag{7.16}$$

$$B = \frac{1}{L_2 - L_1} \ln \left(\frac{A}{y_{L1} + \left(y_{Lp} - y_{L1} \right) \frac{\ln p_0/p_1}{\ln p_2/p_1}} \right). \tag{7.17}$$

The parameters in the equations are defined by the explored parameter space: $L_1 := 5$ Mm, $L_2 := 100$ Mm, $p_1 := 0.1$ dyne/cm^2 and $p_2 = 10$ dyne/cm^2. The other factors, $y_{11} := 1.09$, $y_{1p} := 1.08$, $y_{L1} := 0.926$ and $y_{Lp} := 1.06$, are adjusted by hand and not fitted further by any automated procedure. Still, the maximum temperatures in our temperature profiles do not deviate more than about 2% now, compared to 17% for the original scaling proposed in Serio et al. (1981).

L [Mm]:	5	10	25	50	75	100			
p $\left[\text{dyne cm}^{-2}\right]$:	0.1	0.2	0.3	0.5	0.75	1	2	5	10

Table 7.3: Parameter space for which temperature profiles were generated numerically.

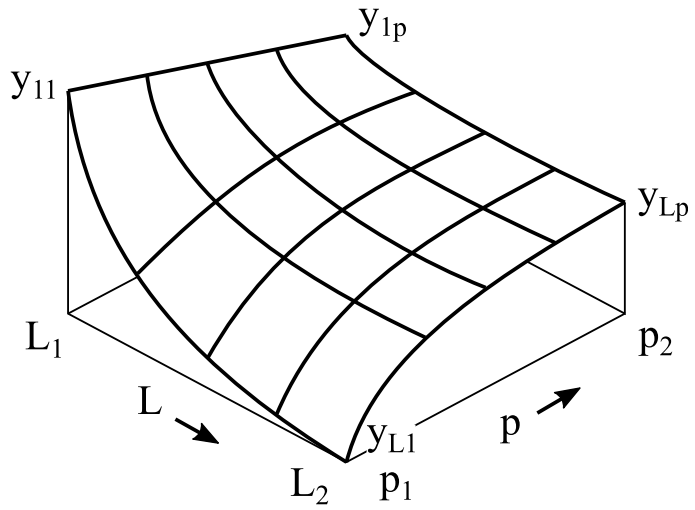

Figure 7.9: The topological shape of the function $y(L_{half}, p_o)$ in our empirically determined approximation of T_{max}.

Analytical approximation of the temperature profiles

Figure 7.10 displays all of the 51 temperature profiles, normalized to the loop length and the temperature differences. It can be seen that all profiles have a similar shape and, therefore, may be approximated by an analytical expression, empirically developed. This approximation is then the $T(s)$ we need for the modelling.

The shape of the profiles is, in principle,

$$\hat{f}(\hat{x}) = a\ \hat{x}^b\ e^{-c\hat{x}},$$

but in a coordinate system where the origin is at $s = L_{half}$ and $T = T_{max}$, the $\hat{x}$-axis points into the negative direction of the T-axis and the $\hat{f}$ is directed towards $-s$. Also, the maximum of $\hat{f}(\hat{x})$ has to coincide with the point (s_0, T_0), where s_0 is the minimum value s can have (in our case 0). Note that since the factor a just scales the dimension of $\hat{f}$, it can be chosen arbitrarily. After the coordinate transformation, and a suitable choice of a, the analytical approximation can eventually be expressed as

$$\frac{L_{half} - s}{L_{half}} = (T_{max} - T(s))^b\ \ e^{-b\frac{T_{max}-T(s)}{T_{max}-T_0}} \tag{7.18}$$

with

$$b = 0.1\left[1 - (s/L_{half})^{1/5}\right] + 0.5(s/L_{half})^{1/5}.$$

The coefficient c has been expressed by b during the derivation. Using the abbreviation

$$\chi := \frac{1}{b}\ln\frac{L_{half} - s}{L_{half}}$$

equation (7.18) can be again solved for T using the Lambert-W function W_{L}:

$$T(s) = T_{max} - \exp\left[\chi - W_{\mathrm{L}}\left(\frac{\exp\chi}{T_{max} - T_0}\right)\right]. \tag{7.19}$$

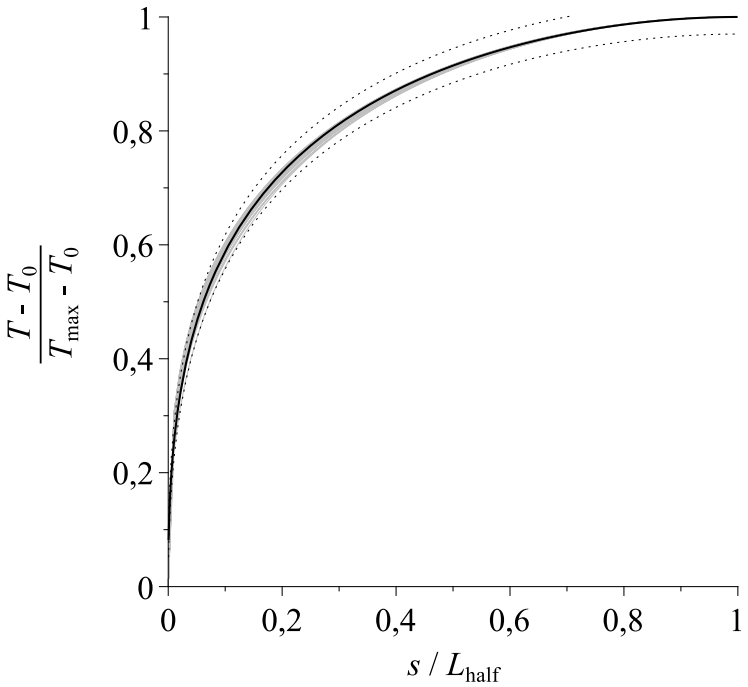

Figure 7.10: Numerically determined temperature profiles (grey lines), normalized to their length and temperature. All of them have a very similar shape and may be approximated with an analytical function (solid, black line, see text for details). The dotted lines denote a 3% deviation from this analytical function.

The values of the Lambert-W function are determined with a Newton iteration.

However, like in the RTV78 model, for any loop only the half length L_{half} is given. There is one free parameter left, either T_{max} or p_0.

The model Serio et al., 1981, + Golub et al., 1982

Here we use the scaling by Golub et al. (1982), equation (7.5), to close the set of equations. As the results do not improve much compared to the RTV78 models, we restrict this section to the model using the NLFFF and the lower boundary being at $z = 5$. For all other combinations, everything said here applies in a very similar way. Problems that have been mentioned when discussing the RTV78 models remain here, too, if not said otherwise.

Figure 7.11 displays the resulting synthesized images, accompanied by the observation. This time, the AIA 211 channel is depicted, as the loops show higher contrast compared to the background than the AIA 171 images. First, for the scaling exactly as in equation (7.5), a side view is presented in the same colour scale as the observations. In this model some of the larger loops have proper intensity instead of being overexposed. This is the improvement of this model compared to RTV78. In total, the AR still becomes far too bright when being modelled this way. This can be seen from the two images in the top view, one in min-to-max scaling and one in the scaling of the observations. The geometrical appearance remains far from the appearance of the real AR, unfortunately.

Therefore, we again applied the modified scaling with the right hand side of equation (7.5) being divided by 1000, as we did in paragraph 7.2.4. The resulting image for the AIA 211 channel is also shown in figure 7.11. The intensities are comparable to the observations, the shape is not, as before.

For the nominal scaling, the physical conditions in the model atmosphere display the same problems as for the RTV78 models. For the modified scaling, the physical conditions are in a proper range, but the problems stated for the RTV78 models remain here, too (figure 7.12).

It must be noted that the heating scale height is infinite. Hence the heating is constant along the loop, like in the RTV78 model. The similarities between the two models in the synthesized images are not too surprising. The main difference in the models presented here is the exponential decay of the pressure with height. The ratio "pressure scale height over loop length" increases with the base pressure and, of course, decreases with the loop length. For a base pressure of 1 dyne cm^{-2}, this ratio is 9.81 for a loop with a semi-length of 5 Mm. For a loop with $L_{half} = 50$ Mm, the ratio reduces to 2.1. For long loops with low density, the loop semi-length can even exceed the pressure scale height.

7.3.3 Discussion

The introduction of an exponential falloff of the pressure in altitude does not really improve the situation. The synthesized images of the AR display very similar problems as the images resulting from the RTV78 models. Thus, we conclude that the model of Serio et al. (1981), together with Golub et al. (1982), is not adequate to describe the AR corona either.

Since there is, in our eyes, not sufficient improvement compared to RTV78, we also abstain from combining the Serio-model with the scaling of Schrijver et al. (2004). Further computations with heating scale height below the loop semi-length are omitted, too.

7.4 An isothermal model

Both the RTV78 and the Serio model assume the loops to be semi circular. Although sometimes many loops of an AR can be nearly circular (for example, they are treated as circular in Aschwanden et al., 2000a) this is, in general, not the case. For example, in AR 11158 many of the large, overarching field lines are rather deformed ellipses, and in the core non planar, S-shaped loops can be found.

The influence on the appearance of a loop by its shape is pointed out in figure 7.13. For four completely artificial loops of the same length but varying shape (also sketched in figure 7.13) the expected appearance is displayed. Temperature, density and cross section are constant along the loops. It is obvious that the brightness variations between the different loops and within a single loop only depend on the shape of the loop. The more the loop is orientated parallel to the line of sight the brighter is the loop since the integration path through the loop increases.

The shape and the length also influence the energy balance of the loop when assuming an exponential decay in pressure and density with altitude. Figure 7.14 depicts the radiative loss power in dependence of the electron temperature which is assumed to be constant along the loops. The pressure scale height is $T \cdot 47$ m/K. These radiative losses normalized to n_0^2 are shown for three different lengths.

7.4.1 Defining the model

With this in mind we propose a static model that includes the exact shape of the loop or field line. For this model we take advantage of the observation that loops in the corona appear to be (nearly) isothermal (Aschwanden et al., 2000a), though it has been claimed that this might be an observational artefact (Peter and Bingert, 2012).

We assume the loop to be isothermal and the density to drop with

$$n_e(s) = n_0 e^{-\frac{h(s)}{h_p T}}$$

with $h_p = 47$ m/K again and h being the altitude. Now, with the heat conduction vanishing, equation (7.1) reduces to

$$0 = E_H(s) - n_e(s)^2 \Lambda(T(s))$$

The heating must compensate the radiative losses exactly. The field lines were gained by interpolating a grid of magnetic field vectors with a Runge-Kutta-scheme. Due to the discrete nature of the

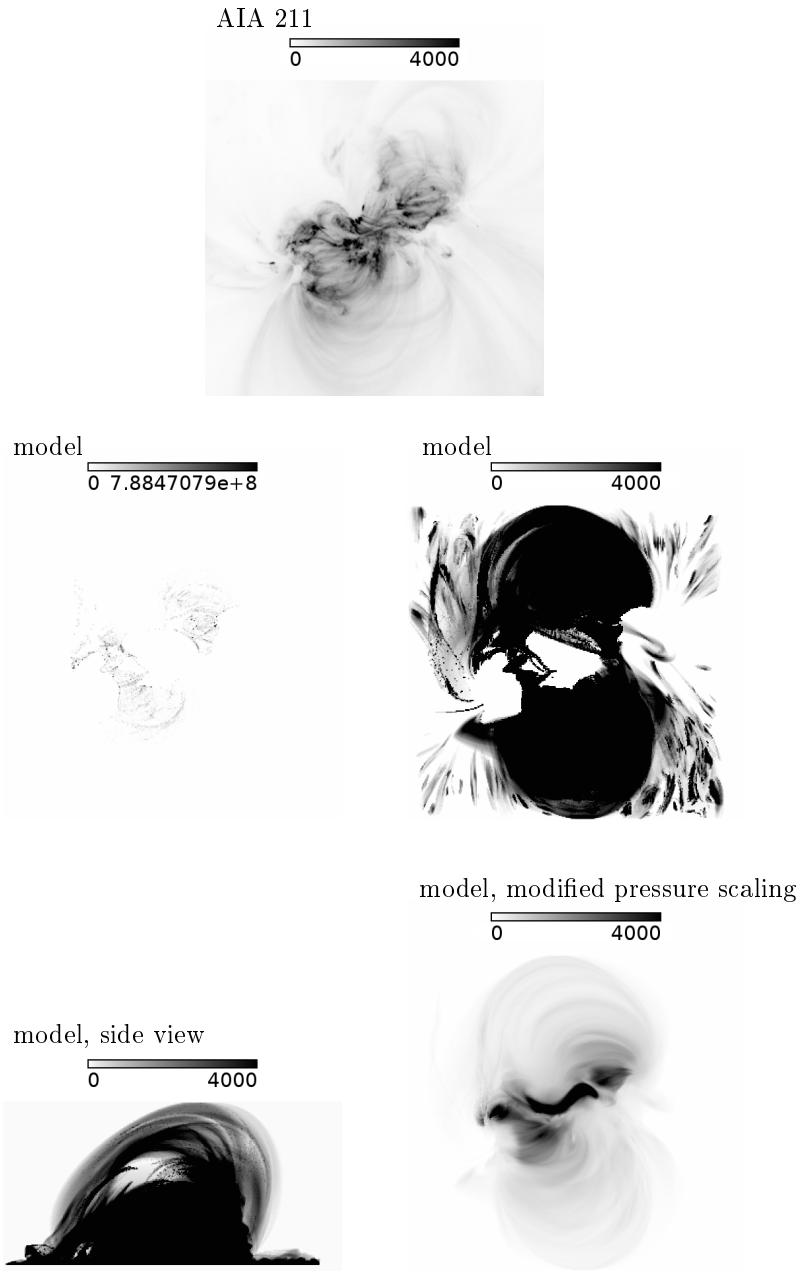

Figure 7.11: Results from the model Serio et al. 1982 + Golub et al., 1982, with NLFFF and the bottom layer at $z = 5$. Top: AIA 211 observations, Middle row: AIA 211 synthesized images in min-to-max scaling (left) and the scaling of the observations (right). Bottom row: synthesized side view (left) and the synthesized image for the modified pressure scaling.

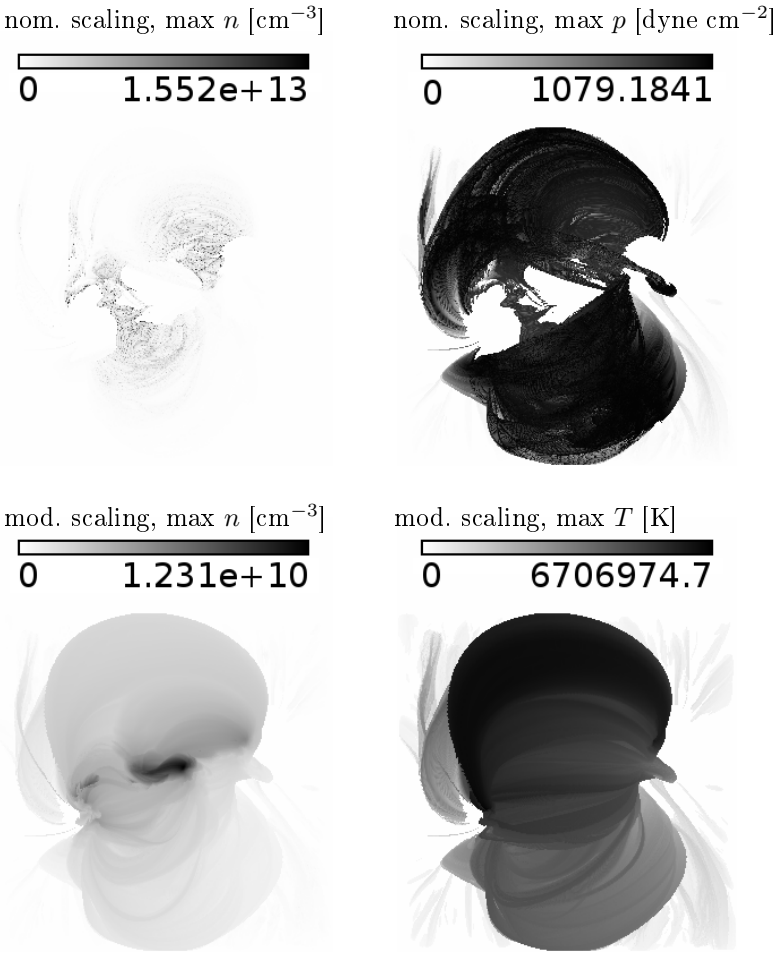

Figure 7.12: Physical conditions from the model Serio et al. 1982 + Golub et al., 1982, with NLFFF. Top: the nominal scaling of Golub et al., 1982. Bottom: the scaling where the pressure is divided by 1000.

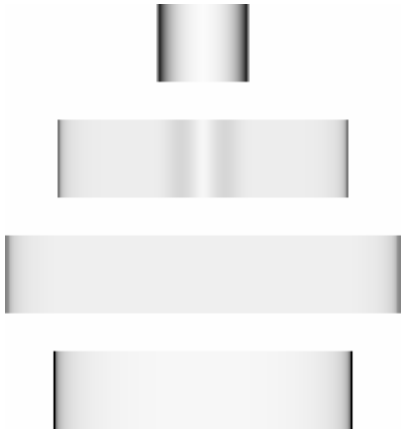

Figure 7.13: Modelled intensities (in a.u.) of four hypothetical loops of the same length. The loops have the same constant temperature and a constant density everywhere. They only vary in shape (fig. 7.14), yielding different appearances. These images are negative images, i.e. darker regions here are actually brighter.

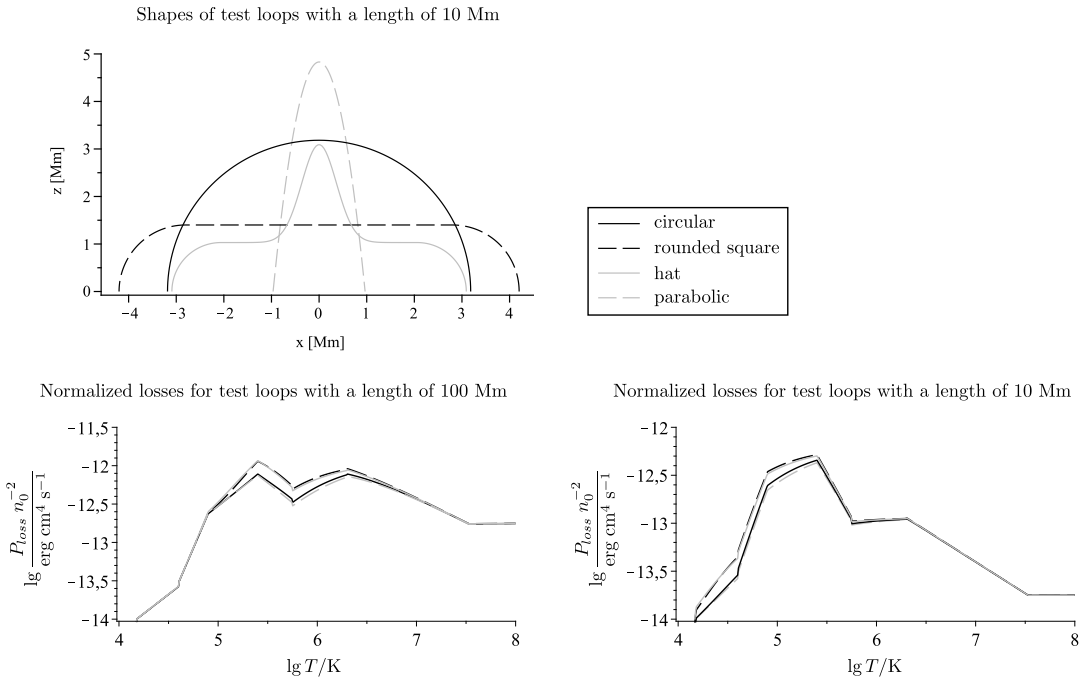

Figure 7.14: The normalized radiative losses $P_{loss}(T)/n_0^2$ for four loops with constant temperatures, but different shapes (bottom panels). Displayed are the cases of different loop lengths. Top panel: The shape of the loops. The different line styles and colours refer to the same shapes in each panel.

scheme, the field lines are polygon curves with nodes at loop coordinates $s_0 = 0,\ s_1,\ \ldots, s_{N-1} = L$. We can exploit this geometrical feature to determine the radiative losses within this isothermal model exactly. The radiative loss power in the straight segment between the nodes i and $i+1$ of the polygon curve can be expressed as

$$P_{loss,i} = n_0^2 \int_{s_i}^{s_{i+1}} e^{-\frac{2h(s)}{h_p T}} \Lambda(T)\, ds.$$

Evaluating the integral yields

$$P_{loss,i} = L_i \Lambda \cdot \begin{cases} \frac{h_p T}{2(h_{i+1}-h_i)} \left(e^{-\frac{2h_i}{h_p T}} - e^{-\frac{2h_{i+1}}{h_p T}} \right) & h_i \neq h_{i+1} \\ e^{-\frac{2h_{i+1}}{h_p T}} & h_i = h_{i+1} \end{cases}$$

when L_i is the length of the segment. The total loss power in the entire loop sums up to

$$P_{loss} = \sum_{i=0}^{N-2} P_{loss,i}. \tag{7.20}$$

This is a function of T and simply proportional to n_0^2. Using Schrijver et al. (2004) again to describe the total heat flux into the loop, the total heating power yields

$$E_{H,tot} = \frac{F_1 + F_2}{L},$$

with F_1 and F_2 being the heat fluxes through the two footpoints, respectively. In our isothermal model, this heat input must be balanced by the radiative loss. On the basis that nature prefers to do as little work as possible, we can compute a kind of well-defined base state with a least amount

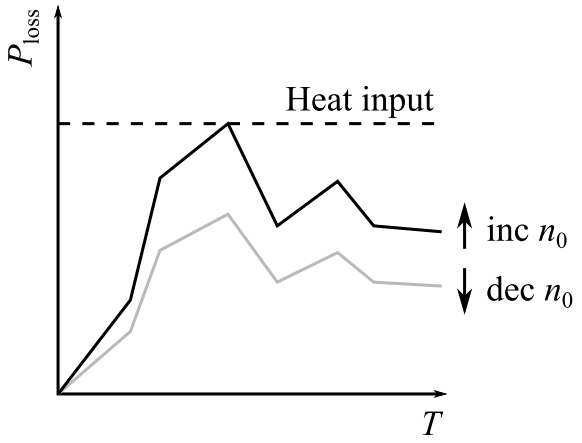

Figure 7.15: By adjusting n_0, the maximum of the radiative losses can be matched with the heat input rate.

of mass in the loop. The temperature where P_{loss} has its maximum is taken as the temperature of the loop. Afterwards, we adjust the base density n_0 such that heat input and radiative loss balance each other (figure 7.15). This way we get the solution with the minimum amount of material in the loop, since lower base densities would prevent the radiative loss to reach the heating power.

7.4.2 Results for the isothermal model

The quasi-isothermal part of the loop is restricted to the corona, hence we restrict the image synthesizing to models where the lower boundary is set to $z = 5$. We also restrict to the NLFFF, as we have ruled out the other field models as being of inappropriate shape in the previous sections. Schrijver et al. (2004) proposed a scaling of the heat flux with $B^{1\pm0.3}/L_{half}^{1\pm0.5}$. Therefore, we computed the isothermal model for different B/L-scalings within the given range. The AIA 171 channel is taken as representative again. Figure 7.16 displays the observations and three different scalings, all of them with the same colour scale. For the model images, the lowest layer of emission was removed for a better comparison of the coronal emission. Especially short loops bridging null lines in the magnetogram cause very localized brightenings which are restricted to the lowest layer of emission (see figure 7.17).

As for the synthesized images, the isothermal model performs slightly better than the models before. The intensities are in the same order of magnitude as for the observations. The model with a scaling proportional to $B^{1.1}/L^{1.1}$ is nearly equal to the observations in terms of intensities, and outperforms the other scalings here. Hence the following results are restricted to this scaling.

The lobes of loops in the north and the south are reproduced, like for the RTV78 and the Serio 81 models. The lobe in the north is somewhat better reproduced here, as the loops which remain in the western half of the AR are more prominent than in the other models. Also, the shape of the loops in the core of the AR are closer to the observations than in the other models. Nevertheless, while the right core loops are bright in the isothermal model, they are bright at their top and darker at their feet. In the observations, it is the other way around. This can be seen for the arcades of loops both in the south-eastern part and in the north-western part of the core. A major exception is the bundle of loops in the very centre of the AR, orientated east-north-east to west-south-west direction.They are very prominent in the AIA 94 observations, but can also be seen in the depicted AIA 171 observations. This bundle is entirely missing in the synthesized images.

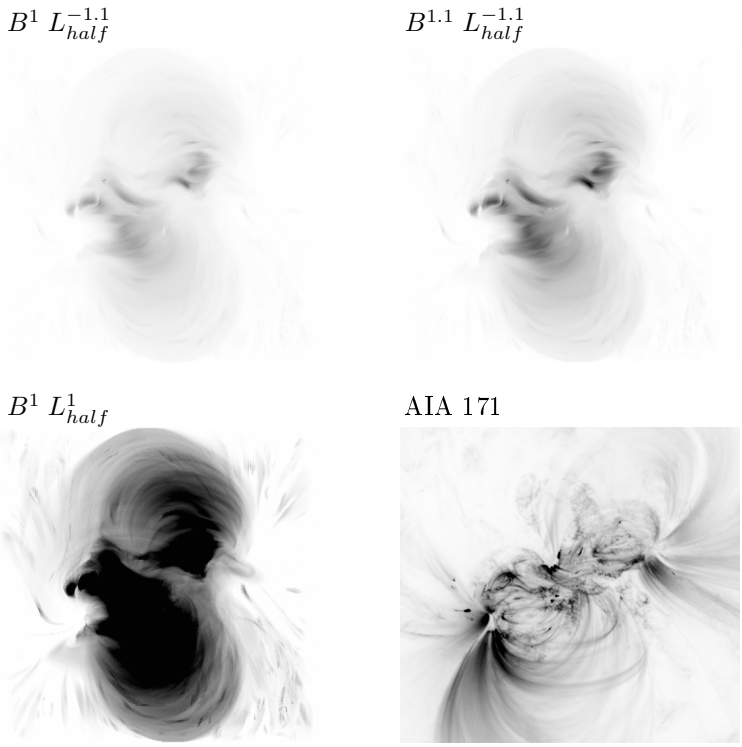

Figure 7.16: AIA 171 images synthesized from the isothermal model for different scalings of the heat flux through the footpoints, compared to the AIA 171 observations. All images are in the same colour scale, which is the same as for panel (a) in figure 7.2. For the synthesized images, the lowest layer of emission was removed so that the coronal emission can be seen better (see figure 7.17).

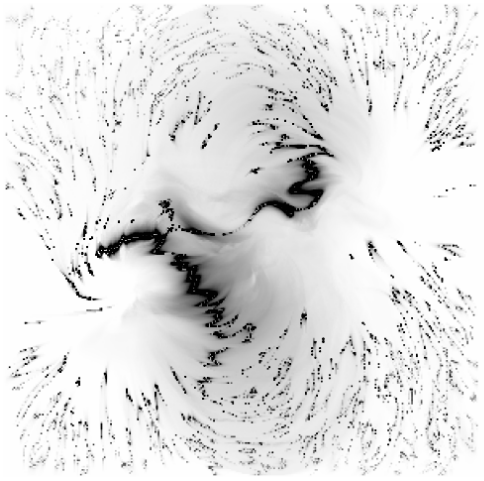

Figure 7.17: Synthesized AIA 171 image for the isothermal model with a heat flux scaling of $B^{1.1}/L^{1.1}$. Compared to figure 7.16, the lowest layer of emission, including brightenings from very short loops, has been kept.

7.4.3 Conclusions from the isothermal model

The isothermal model yields synthesized images closer to the observations than the RTV78 model or the Serio-model. The differences to the observations are still significant, though. Consequently, we cannot accept this model either.

Nevertheless, the overall intensities produced by the model with a $B^{1.1}/L_{half}^{1.1}$ scaling matches the intensities of the observations. Within the errors, this result supports the B/L scaling of the heat flux as proposed by Schrijver et al. (2004). It is also consistent with studies by Warren and Winebarger (2006), which found a similar scaling for the heating.

7.5 Discussion and conclusion

The results of the forward models presented in this chapter are not encouraging. None of the models is able to reproduce the observations in the AIA channels. This is in line with the studies by Lundquist et al. (2008a), Warren and Winebarger (2006) and Dudík et al. (2011), who also could not produce satisfactory results with static modelling. Following their lines of thought, we must raise the doubt that static models are an appropriate description of the AR corona, too. This part of the solar atmosphere is very dynamic, as it can be seen from high-cadence EUV observations. It must be questioned if loops are in a static or stationary state for longer periods at all. The loops may rather be like leaves in the storm: many of them can be seen flying around all the time, which is somehow a stationary state for the entire throng of leaves. Individual leaves, on the other hand, are never in a static state except when lying on the floor until they get blown away again.

So instead of forward-modelling more models, we have to come up with a completely different approach.

Chapter 8

Reconstructing the 3D corona: The *FitCoPI* method

In the previous chapters, different methods have been evaluated as unsatisfactory. Thus, we have to come up with a new solution. The idea of the ansatz described in this chapter yields from the following line of thought:

- Intensities are proportional to the density squared. Thus, they provide information about the amount of plasma in the LOS of a pixel.

- The coronal plasma is optically thin. When two loops are crossing each other in the observations it cannot be determined immediately how much emission originates from which loop.

- However, intensities along a loop should not change abruptly. Pixels in the neighbourhood of loop-crossings may help to overcome the problem mentioned in the previous item. This would require an algorithm to detect the pixels physically connected by a loop to any pixel in the observations.

- Since we have access to field line extrapolations, we can waive such an algorithm. Instead, we simply use the field lines as tracers of the loops.

The final result of these thoughts and the subsequent developments is the *FitCoPI* code (fitting coronal plasma iteratively), which is described in Barra (re-submitted to Solar Physics).

In this chapter, we present this new iterative method of fitting the densities and temperatures to the observations directly, without any constraints of physical models. The content of this chapter is from the publication mentioned above. The publication is briefly repeated here.

The SDO observations provide us with the 2D deviation of intensities in several EUV passbands. The problem is that, due to the high transparency of the corona in the EUV, we cannot distinguish directly how much intensity is produced at which point of a LOS. We always see a LOS integrated projection of the corona. Additionally, this problem goes hand in hand with the fact that many loops visible in EUV images of the AR are criss-crossing each other. The agent that helps us overcoming this problem is the magnetic field extrapolated from HMI data, which exists in 3D.

Another method which allows to obtain the 3D atmosphere is described in Warren et al. (2018). They link coronal loops that are detected in the observations with field lines derived from magnetic field extrapolations. In the end of this chapter, we compare their approach with the *FitCoPI* code.

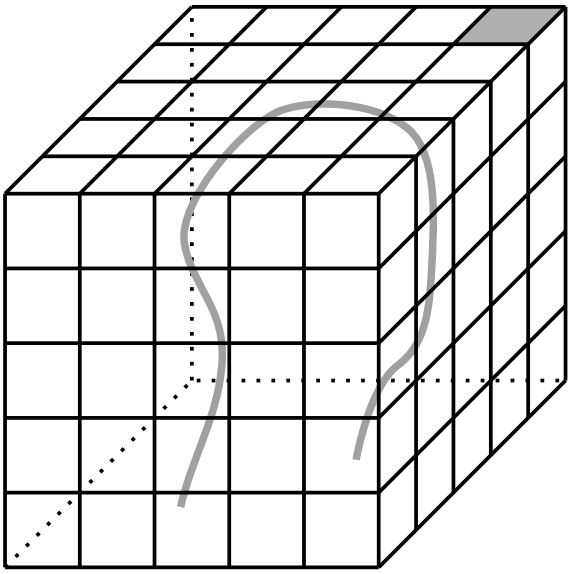

Figure 8.1: Setup of the numerical box: The grid cells are defined by the pixels (squares in top facet, one is highlighted in grey). Field lines are within this box and sample points (not depicted here) are placed on them (from Barra, re-submitted to Solar Physics).

8.1 Setting up the *FitCoPI* method

8.1.1 Setup of the numerical box

Numerical methods cannot work at infinite resolution but instead has to operate at a certain numerical resolution. The higher this resolution is the more precise are the results, but the stronger are the requirements in memory and computation time. The resolution of observations are limited by the instrument, hence it is useful for our iterative approach to subdivide the observed volume of the AR into cubic cells where the top facets match the size of one pixel when projected onto the detector. Since the sun is far away compared to the LOS depth of the observed volume, the LOS of different pixels can be considered parallel. The orientation of the computational cells is now chosen in the way that the edges are aligned to the LOS as well as the edges of the images of SDO (fig. 8.1).

For approximating the AR corona, we assume the plasma within one sub-cell (see below) to have a single value of the density and the temperature. This way it is easy to compute a hypothetically observed intensity in each filter of SDO, using equation (4.2). Together with the chosen alignment of the cells, the modelled, LOS-integrated intensity in a pixel can be calculated now by simply adding up the intensity from all cells along a column of the numerical box. However, exchanging two cells in the same column would not change the resulting synthesized image. In this thesis, we consider such two configurations to be *observationally equivalent* (OE).

The challenge is to obtain the configuration of physical conditions which does not only produces synthesized images that are close to the observations, but also close to the 3D corona, distinguishing it from other OE configurations. For doing so we utilise that a loop causes two points on it to be in physical contact. Due to mass flows and heat conduction, changes in the one point soon affects the other. Therefore, the configurations in the numerical cells cannot be chosen completely independent of each other. Instead, they are correlated to each other by the magnetic field.

8.1.2 Key idea

We have to deal with the problems of the transparent corona and the criss-crossing loops in images, as well as using the loops/the magnetic field for connecting different points in the numerical box.

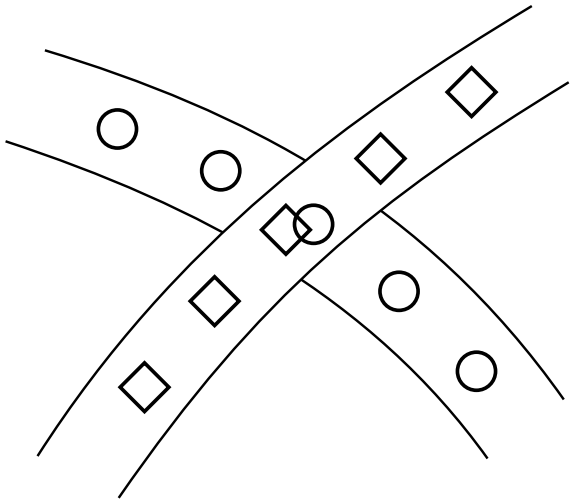

Figure 8.2: Two crossing loops with sample points placed on them. As the iterative updates are smoothed along the loops, the two sample points in the crossing can develop differently (from Barra, re-submitted to Solar Physics).

For doing so, we do not calculate the densities and temperatures in the grid cells directly. Instead, we compute these quantities on sample points equally spaced along the magnetic field lines derived from the extrapolated field data.

In the pixels affected by a sample point, the intensity ratios between the most recent synthesized image and the observations is used for determining an intermediate update on the sample point. The intermediate update is than smoothed with the intermediate updates of the neighbouring sample points *on the same loop* to a final update in the iteration step. After all final updates were applied to the sample points, new images are synthesized. Due to the smoothing, the properties in two intersecting loops can be distinguished in the intersection point. The information diffuses from sample points nearby into the intersection point (fig. 8.2).

8.2 Implementing the approach

We point out that there is not an unique way to implement the general approach. The implementation here is fairly simple, and more sophisticated implementations may be developed in the future.

8.2.1 The field lines and the sample points

First, we have to compute a set of field lines. This set has to be large enough to fill the AR and prevent artificial holes in the numerical set-up. On the other hand, it should not be too tight. First, more field lines imply more sample points and hence more computational demands in all aspects. Second, too many sample points too close to each other may prevent each other from getting enough influence onto the numerical cells (see below).

Like with the numerical box and its grid cells, which were derived from the SDO images and pixels, we take the resolution of the extrapolated field data as reference for our needs. This extrapolated field is given as magnetic field vectors on a $N_x \times N_y \times N_z$ equidistant grid. The spatial resolution of this data, and thus for our set of field lines, is determined by HMI. We call a Runge-Kutta-integrator for determining a field line from the NLFFF-model of the investigated AR. All grid points on at the bottom of the computational box are used as a starting point for the integrator. However, many of the resulting field lines remain extremely short and low, often ending after just one integration step. We thus immediately drop all field lines with a length less

than 8 grid point distances. This lengths translates to roughly two pixels in the images we use as input for the iteration (as described below). The smoothing for discriminating the conditions in crossing loops becomes infeasible on such short lengths.

The edge length of a cell may be denoted with d. The sample points must obey the Nyquist frequency, thus have to be placed not more than $0.5d$ apart from each other. To be on the safe side, we placed them with a spacing of $0.3d$, measured along the field line.

8.2.2 Filling the volume with plasma

So far we have 0D sample points located on 1D field lines in a 3D volume. How can we map the essential data on the sample points into the 3D volume? Here, we introduce sub-cells that help determining the influence of a sample point onto a cell but, in the end, must not be stored separately since all information is averaged over a cell anyway.

We subdivide each cell further into $N \times N \times N$ sub-cells and define a radius u_i for each sample point i. The radius describes the lateral radius of the loop at this point, and thus the loop cross section. We then assign each sub-cell to up to either one or no sample point, while a single sample point can be connected to several sub-cells. Each sample point applies for an assignment to all sub-cells that centre is not further away from the sample point than the u_i of the sample point. From all sample points applying for it, a sub-cell is assigned to the closest one. A sub-cell is assumed to be filled with homogeneous plasma of the density and temperature stored in the assigned sample point. Sub-cells that remained unassigned contain vacuum.

8.2.3 Influence of sample points, cells and pixels

Please note that we use the subscripts i and j for sample points, l and m for cells, μ and ν for pixels, f and g for the filters of the observing instrument.

The number of sub-cells in a cell assigned to a sample point determines the influence of the sample point on the cell. We denote the volume fraction of a cell l occupied by sub-cells assigned to sample point i with

$$c_{il} \in [0; 1],$$

the *cell weight*. Since the LOS integration for a pixel μ is done by summing up the contributions of the cells in one column, we also sum up the cell weights of a sample point i in that column. This obtains a measure for the influence of the pixel onto the sample point, the *pixel weight*:

$$p_{\mu i} := \sum_{\text{LOS of } \mu} c_{il}.$$

This measure is not limited to unity. For taking the average of a quantity with the pixel weights, we also need the *total pixel weight* of a sample point i,

$$P_i := \sum_{\mu} p_{i\mu}.$$

Figure 8.3 clarifies the relationship and weights between the sample points, the grid cells and the pixels.

8.2.4 Intensity from a cell

With equation (4.2), the intensity originating from a sub-cell and detected in filter f, in DN, can be modelled as

$$I_{sub,f} = A \frac{\Delta t_f}{N^2} \cdot \frac{d}{N} \cdot n_{sub}^2 K_f(T_{sub})$$

Compared to eq. (4.2), we set $\omega = 1/N^2$ the fraction of the pixel illuminated by the sub-cell (in pixel) and $\Delta z = d/N$ the depth of a sub-cell (in cm). The factor A is an area factor coming

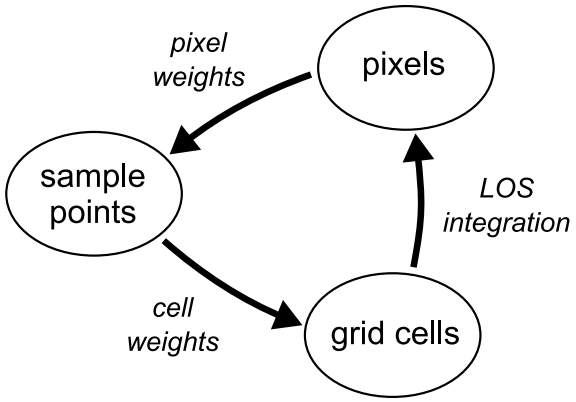

Figure 8.3: Relationship between, sample points, grid cells and pixels and their influential weights (from Barra, re-submitted to Solar Physics).

into play when rescaled observations are used instead of the original ones. In that case, A is the rescaled pixel area relative to the original pixel area. A possible reason to rescale the images would be that a lower resolution also results in a lower number sample points and, as a consequence, less computational demands. We use this later for our tests. The equation is multiplied with the exposure time Δt_f (in s) for getting the detected intensity (in DN) rather than the count rate. A subscript for the filter is kept for the exposure time because this value might be different for different filters. The density and temperature of the plasma in the sub-cell are described by n_{sub} (in cm^{-3}) and T_{sub} (in K), respectively.

Adding up the contributions of each sub-cell yields the detected intensity originating from the entire cell, which is required for the method. It gives

$$\begin{aligned} I_{kf} &= \frac{\Delta t_f}{N^2} \cdot \frac{d}{N} \sum_{\text{sub-cells}} n_{sub}^2 K_f(T_{sub}) \\ &= A \cdot d \cdot \Delta t_f \sum_i c_{ik} n_i^2 K_f(T_i), \end{aligned} \tag{8.1}$$

since $1/N^3$ is the volume fraction of a sub-cell to a grid cell. All such volume fractions of the sub-cells assigned to the same sample point add up to the cell weight c_{ik}, by definition.

The detected intensity in a single pixel now follows from adding up the contributions from all cells along the line of sight:

$$\begin{aligned} I_{\mu f} &= \sum_{\text{LOS}} I_{kf} \\ &= A \cdot d \cdot \Delta t_f \sum_i p_{\mu i} n_i^2 K_f(T_i). \end{aligned}$$

because of the definition of the pixel weight $p_{\mu i}$ as the sum of a single sample point's cell weights in a line of sight.

The sub-cell as a concept

Please note that from (8.1), the cell intensity can now be derived from the values stored in the sample points alone. Therefore there is no need to store the sub-cells themselves once the cell weights have been determined. However, for mapping the values of the sample points into the 3D volume, the sub-cells are a fine concept which provides several desirable advantages:

- The sub-cells consider the loop cross section via the u_i, specified for each sample point. Thus, volume far away from loops never contains plasma, while at the same time allowing

a competition where sample points are close to each other. Where sample points are dense, with their cross sections overlapping, the volume is fairly distributed to the, locally, closest sample point.

- When increasing the number of sub-divisions, the distribution of the volume to the sample points just becomes finer and finer, but eventually does not change much. In other words, the distribution converges for $N \to \infty$.
- The sub-cells do not have to be stored during the cell weight determination process either. The cell weights for each grid cell can be computed independently from the other cells. Therefore, it is possible to compute the cell weights for an entire cell and, after this has been done, use the same storage for computing the cell weights of the next cell.

8.2.5 Smoothing kernel

The smoothing along the field lines is elemental to the method. We use a simple Gaussian kernel for this task. First we define an individual contribution

$$W_{ij} := \begin{cases} \exp\left(-\left(\frac{s}{s_c}(i-j)\right)^2\right) & \text{if } |i-j| \leq s_c \\ 0 & \text{else} \end{cases}$$

which then becomes normalized to

$$w_{ij} := \frac{W_{ij}}{\sum_j W_{ij}}.$$

Here, s_c is a cut off distance and s a parameter controlling the width of the Gaussian.

8.2.6 Iterative update

The iterative update follows a certain scheme for both density and temperature. Based on the comparison between synthesized and observed images, an intermediate update (labelled with superscript *int*) is computed from the current values (labelled with a superscript *old*). By smoothing the intermediate values along the field lines, the new values (denoted with a superscript *new*) are generated. A full iteration consists of a density update first and a temperature update afterwards. After both of them, new synthesized images are generated.

In the updates, we use two measures as weights for averaging. The firsts are normalized response functions

$$k_f(T) := \frac{K_f(T)}{\max_T K_f}.$$

The second measure is the ratio of the observed intensity I in a pixel μ to the intensity in the brightest pixel for each channel f:

$$b_{\mu f} := \frac{I^{\text{obs}}_{\mu f}}{\max_\nu I^{\text{obs}}_{\nu f}}.$$

Density update

It follows from equation (4.2) that the intensity is proportional to the density squared. Consequently, a good assumption for the new density is

$$n^2_{\text{new}} \approx n^2_{\text{old}} \frac{I^{\text{obs}}_{\mu f}}{I^{\text{syn}}_{\mu f}},$$

based on the observed (obs) and synthesized (syn) intensity of pixel μ in filter f. For a given pixel μ, the ratio

$$\alpha_{\mu f} := \frac{I^{\text{obs}}_{\mu f}}{I^{\text{syn}}_{\mu f}} \tag{8.2}$$

varies between the different filters f. Therefore, for a certain sample point i, we define a filter averaged influence of the pixel by

$$\beta_{i\mu} := \frac{\sum\limits_f \Big(\alpha_{\mu f} b_{\mu f} k_f(T_i)\Big)^{1/2}}{\sum\limits_f \Big(b_{\mu f} k_f(T_i)\Big)^{1/2}}. \tag{8.3}$$

Since this also varies from pixel to pixel, we have to average it using the pixel weights:

$$n_i^{\text{int}} := \begin{cases} \dfrac{n_i^{\text{old}}}{P_i} \sum\limits_\mu p_{\mu i}\beta_{i\mu} & \text{if } P_i \neq 0, \\ n_i^{\text{old}} & \text{else.} \end{cases}$$

Eventually, the new density for the sample points is then

$$n_i^{\text{new}} := \frac{\sum\limits_j n_j^{\text{int}} w_{ij}}{\sum\limits_j w_{ij}}$$

Temperature update

The temperature update can be derived from filter ratios. For $I_{fg} := I_f/I_g$ and $K_{fg} := K_f/K_g$, it follows from (4.2) that in first order approximation

$$\Delta I_{fg} \approx \frac{\partial K_{fg}}{\partial \lg T} \Delta \lg T$$

holds. The ΔI_{fg} is a difference, and the equation above basically a first order Taylor expansion of $K_{fg}(\lg T)$. Solving the equation for $\Delta \lg T$ yields a forward Euler scheme for updating the temperatures. To do so, we define

$$\gamma_{\mu fg} := \begin{cases} I_{\mu fg}^{\text{obs}} - I_{\mu fg}^{\text{syn}} & \text{if } I_{\mu fg}^{\text{obs}} < 1, \\ I_{\mu gf}^{\text{obs}} - I_{\mu gf}^{\text{syn}} & \text{else,} \end{cases}$$

in analogy to the $\alpha_{\mu f}$ of the density update. We then first compute the filter average

$$\delta_{\mu i} := \frac{\sum\limits_{\substack{1 \le f < F \\ f < g \le F}} \gamma_{\mu fg} \rho_{fg} \left(k_f k_g b_{\mu f} b_{\mu g}\right)^{1/4}}{\sum\limits_{\substack{1 \le f < F \\ f < g \le F}} \left(r_f r_g b_{\mu f} b_{\mu g}\right)^{1/4}}. \tag{8.4}$$

Here, the function

$$\rho_{fg}(\lg T) := \begin{cases} \left(\frac{\partial}{\partial \lg T} R_{fg}(\lg T)\right)^{-1} & \text{if } I_{\mu fg}^{\text{obs}} < 1 \\ \left(\frac{\partial}{\partial \lg T} R_{gf}(\lg T)\right)^{-1} & \text{else} \end{cases}$$

is evaluated at $\lg T_i$ and the normalized responses k_f and k_g at T_i. From this follows

$$\lg T_i^{\text{int}} := \begin{cases} \lg T_i^{\text{old}} + \dfrac{\Delta s}{P_i} \sum\limits_\mu \delta_{\mu i} p_{\mu i} & \text{if } P_i \neq 0, \\ \lg T_i^{\text{old}} & \text{else.} \end{cases}$$

Here, Δs is a step size which is dynamically adjusted, as described below.

8.2.7 About design of the code

In the equations (8.3) and (8.4) the factor b_i appears. Also, the weight in the density update, (8.3), is a square root. Likewise, the weight in the temperature update, (8.4), is a fourth-order root. All this came out of our test, and here we briefly describe why the equations are as they are.

First about the roots. Initially the weight in the density update simply was k_f, which is obviously linear in the normalized response function k_f. A similar but quadratic weight of $k_f k_g$ in the temperature leads to an instability: the total DN count, which is used for the exit criteria, eventually runs haywire and no solution is found. Using the weight $(k_f k_g)^{1/2}$ instead, which is again of linear order, fixes this problem.

The factors b_i are not essential. Nevertheless, in our test case of AR 11087 they improve the results in the parts of the observations which are dark in many or even all channels. Spuriously high densities are much less frequent when including the factors.

The additional factors change the power of the weighting terms again. To balance this, the square root and, respectively, the fourth-order root are taken, as they can be found in the equations above.

The procedure monitors the total of DN count over all pixels in all filters. If this value oscillates, the step size Δs is multiplied with one half. In case the total DN count does not change much, the step size is increased by 5%. Additionally, the step size is clamped between 0.04 and 0.4, bounds rarely reached. The code terminates automatically when two criteria are met. First, the total DN counts after the last 200 iterations must not deviate more than 4% from their mean. Second, after each iteration the mean total DN count over the last 20 iterations is stored. The last 200 of these means must not deviate more than 1% from their collective average.

8.3 Evaluating the algorithm

The quality of the results the algorithm produces has been exhaustedly evaluated in Barra (re-submitted to Solar Physics). We briefly summarize this evaluation. For this evaluation, we synthesize an artificial AR corona from a simple loop model. The EUV images AIA would see when observing this model AR are generated. This hypothetical observations serve as input observations for the fitting process.

The advantage of the model AR is that we know its physical conditions everywhere down to the last detail. For real ARs this is not the case.

8.3.1 Comparing the fitted values to the model AR

For the evaluation we have to compare the synthesized reconstruction (RS) values to the ground truth synthesized (GTS) values of the model AR.

Line-of-sight images

Figure 8.4 shows the RS images and the GTS images obtained when observing along the hypothetical LOS of an instrument. These GTS images are used for the fitting process. Although the intensities are not fitted directly, these GTS images should still be reproduced by the code. Here, the channels AIA 171, AIA 304 and AIA 335 are displayed. The second one because it is the worst reproduced, the latter one because it is reproduced best. The reproduction quality of the channels not depicted here are similar to the one of AIA 171. Obviously, all channels are reproduced quite nicely. To demonstrate how well, the last row in figure 8.4 shows a measure of the relative deviations of the RS intensities, I_{RS}, from the GTS intensities I_{GTS}, $\lg\left(|I_{\mathrm{RS}} - I_{\mathrm{GTS}}|/I_{\mathrm{GTS}}\right)$. It can be seen that the largest deviations appear where the detected emission is faintest. In bright areas, the deviations are typically small. Over all pixels of all seven EUV channels of AIA, the RS intensity deviates less than 20% from the GTS value in about two thirds of the pixels.

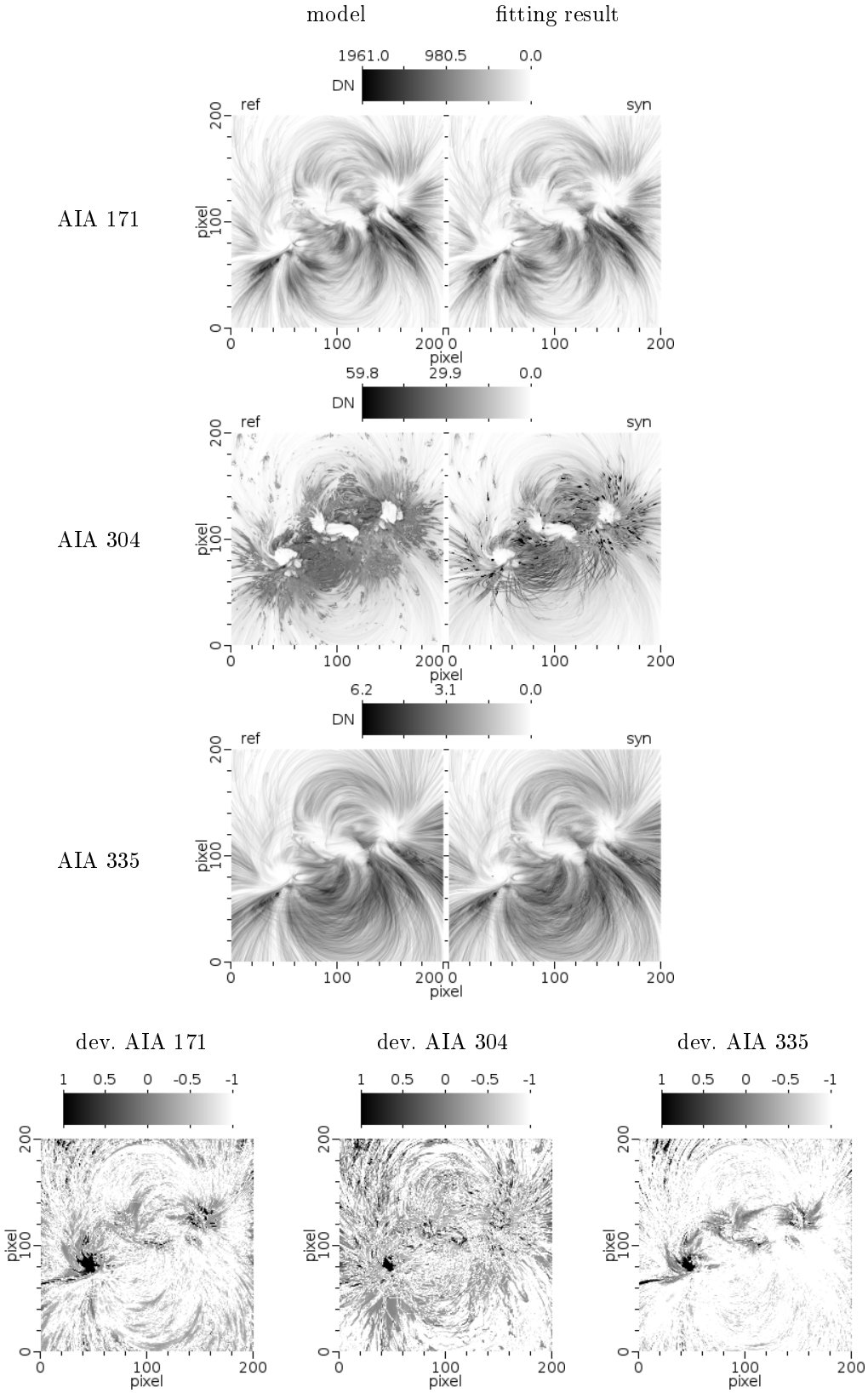

Figure 8.4: First three rows: GTS "observations" of the model AR (left) and to the RS images resulting from the fitting process (right). Last row: measure of the logarithm of relative deviations for each pixel, clamped between -1 and 1. Displayed are the channels AIA 171, 304 and 335. The LOS is the typical LOS an instrument on a spacecraft orbiting Earth would have (from Barra, re-submitted to Solar Physics).

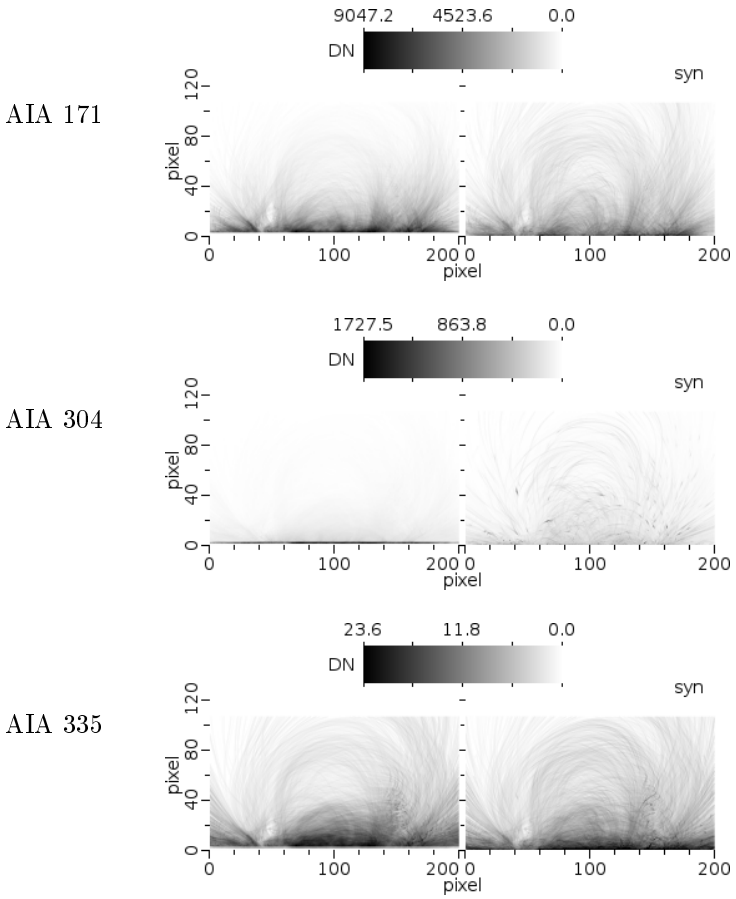

Figure 8.5: left: GTS "observations" of the model AR. Right: RS images resulting from the fitting process. This is a side view. In fig. 8.4, the hypothetical observer of this figure would watch from the right to the left (from Barra, re-submitted to Solar Physics).

Side view images

In figure 8.5 the same scene is shown in a side view. As these GTS images are not involved in the fitting process, this view is an independent test case. As we want to obtain the 3D density and temperature of the AR plasma, these images should be reproduced as well. Nevertheless, larger deviations caused by the errors that come with the method can be expected. Therefore, this view offers a first way of evaluating the quality of the approach.

The GTS images are again well reproduced. The structure of loops and fans of loops can be found in the RS images to a large extent. Only two points come to the eye: First, the photosphere and the chromosphere are unresolved. In the GTS images the lowest layers are invisible as the model AR is too cool to be seen in EUV here. Presumably due to the smoothing, coronal temperatures reach down to the bottom of the numerical box, and the lowest layers appear bright in the RS images. Second, some longer loops do not faint towards the top as they do in the GTS images. Very likely this means that the densities are overestimated in some of the longer loops.

Keeping these two issues in mind, we note that, in general, the structures are reproduced.

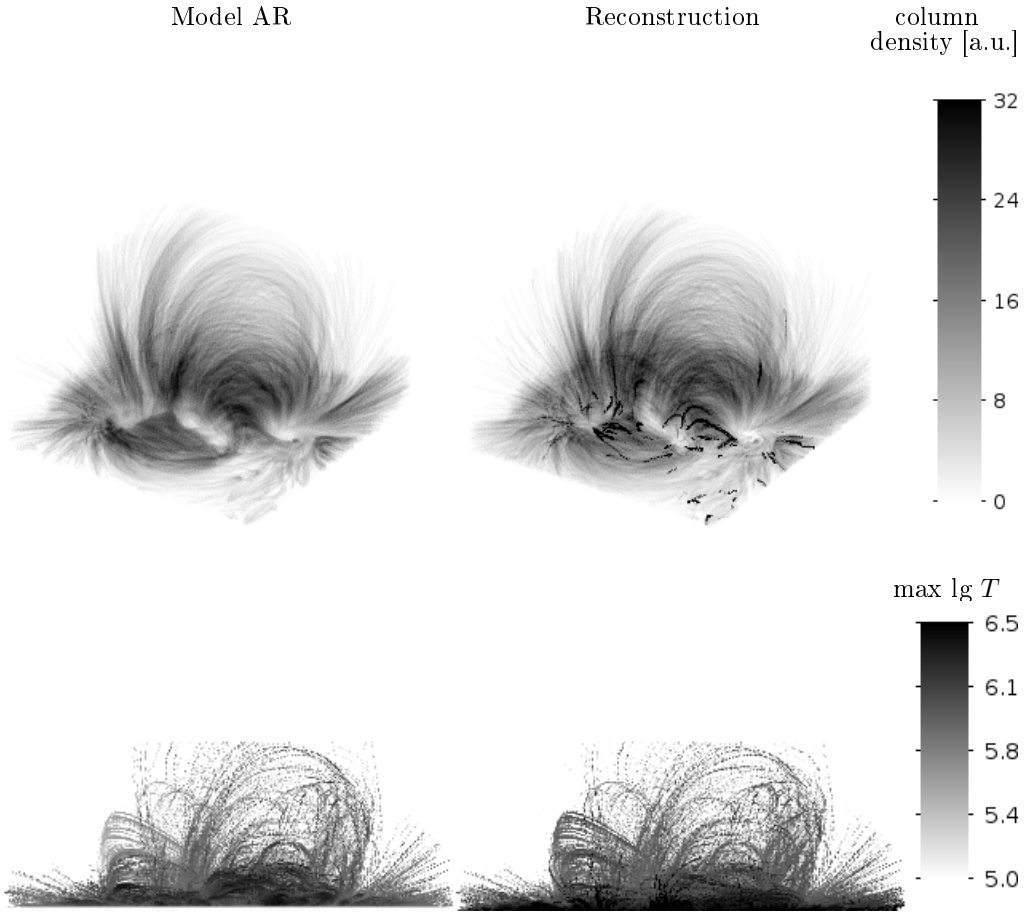

Figure 8.6: Top row: column densities, bottom row: max lg T along the LOS (from Barra, re-submitted to Solar Physics).

8.3.2 Density and temperature distribution

In figure 8.6 the column densities of the model AR and the fitting results are opposed to each other. The vantage point is in the top left corner of figure 8.4 and the view is tilted 60 degrees against the LOS of that figure. Again, the structure of the AR matches in both images very well. In the RS AR, some isolated and low lying loops can be found. These loops have densities orders of magnitude higher than the remaining AR. Hence, they can easily be spotted in the data. As they are very rare, they do not break the generally good reproduction.

The same figure also depicts the maximum lg T along the LOS for both the GTS AR as well as the RS AR. The vantage point is similar to the one in the images for the column densities. Just the view direction is now perpendicular to the one in figure 8.4. It is demonstrated now that, in the lowest layers only, the temperatures are too high. As before, however, the general structure of the AR is broadly captured.

For a numerical evaluation of the discrepancies between the GTS physical parameters and the fitted RS values, we binned all sample points according to their relative loop position. This allows us to compare sample points in the middle of their host loops with other sample points in the middle of their loop and so on. On the other hand, sample points of short, low reaching loops are binned together with long loops reaching high above the solar surface. For now, we ignore the latter issue.

For each bin, we determine the median, the 25% quantile and the 75% quantile of both the relative deviation in density, $\Delta n_{rel} := (n_{RS} - n_{GTS})/n_{GTS}$, and the relative deviation in tempe-

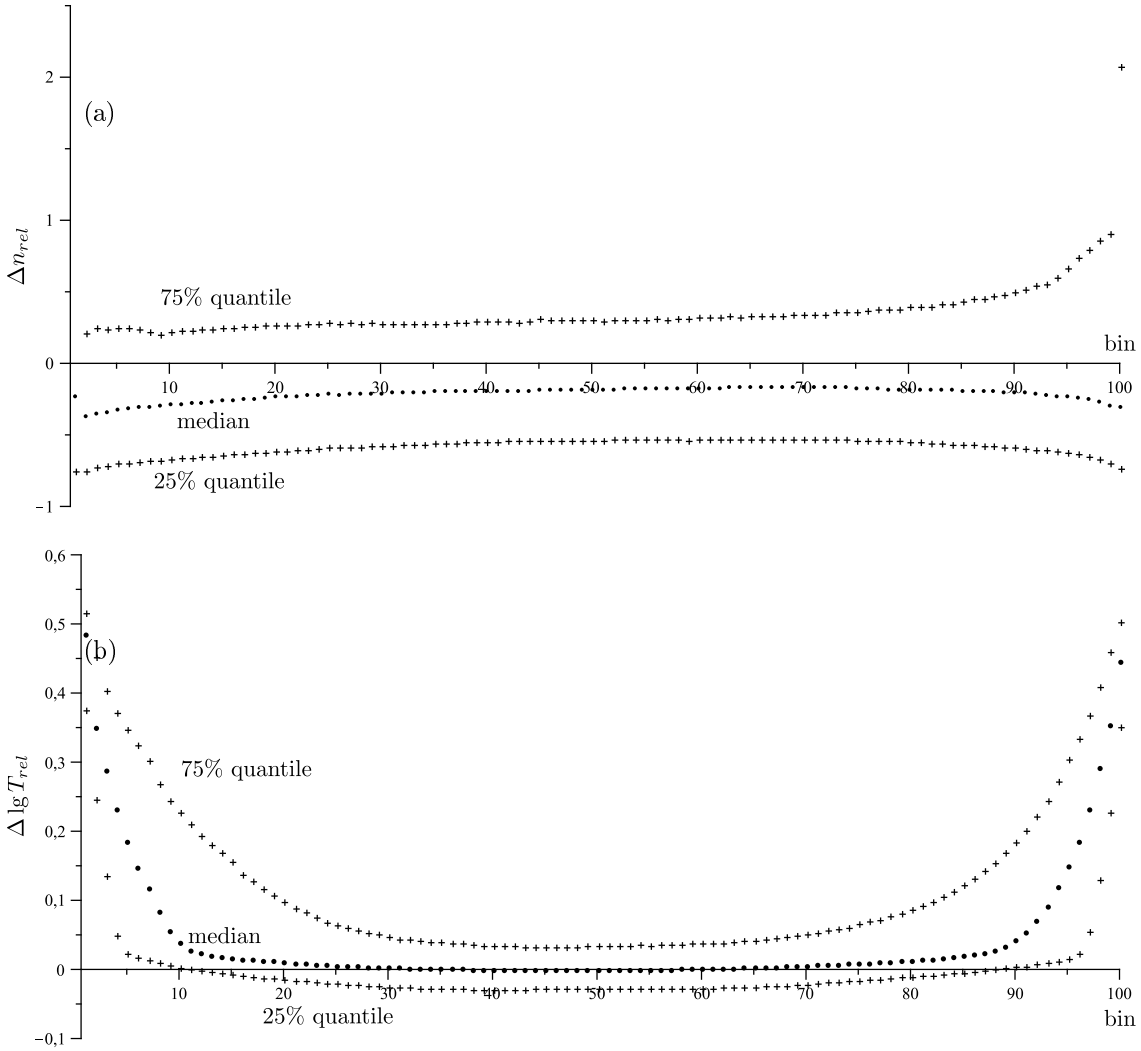

Figure 8.7: Top: relative deviation in density, bottom: relative deviation in temperature (from Barra, re-submitted to Solar Physics).

rature, $\Delta \lg T_{rel} := (\lg T_{RS} - \lg T_{GTS})/\lg T_{RS}$. For the statistics, we included only sample points above an altitude of $z = 3.2$ in grid space. In the model, this is the boundary between the corona we are interested in and the chromospheric part which already has been shown to have poorly matching temperatures in the reconstruction. Since emissivity goes with density squared, sample points with a model density below 0.01, the maximum possible density in the model is 1, are also excluded from the statistics on account to be too faint. Figure 8.7 plots the statistics. In the middle of the loops, the correct values are reproduced within the scattering range. The densities are, in median 20% below the model values. There are still sample points with overestimated densities, as it was suggested above. The RS temperatures are close to the GTS values. Near the end of the loops, the reconstructed temperatures exceed the model values, which can be explained again by the coronal temperatures being smoothed down to the lower layers.

Direct comparison

Here, we restrict our analysis again to sample points with an altitude above 3.2 and a model density above 0.01. Figure 8.8 depicts density plots for different measures. Each plot consists of

	rank correlation		rank correlation
density	0.4164	193 Å	0.4713
$\log T$	0.4801	211 Å	0.4647
94 Å	0.4657	304 Å	0.3183
131 Å	0.3527	335 Å	0.4404
171 Å	0.4331		
critical value:			0.0018

Table 8.1: Spearman's rank coefficient of correlation between the model values and the fitted values. It is computed for the density and the logarithm of the temperature of the sample points, and the "detected emissivity" $n^2 K_f(T)$ in each filter. The threshold value, up to which the compared measures are *un*correlated, is determined for a two sided test with a level of significance of 0.1%. The analysis is again restricted to sample points with a model density of 0.01 or above and an altitude of at least 3.2 (from Barra, re-submitted to Solar Physics).

300×300 bins. The plotted value is the number of sample points which fall into a bin, according their GTS value and their RS value. Besides the large scatter, the values have a tendency to follow the $x = y$ -line. Table 8.1 shows the rank correlation after Spearman between the GTS values and the RS values (for example Müller, 1975). Also noted is the critical value of rank correlation above which the GTS values and the RS values are *not un*correlated. It can be read from the table that the reconstructed values are clearly not uncorrelated from the model values. If this would be different, the code would not be reliable.

8.3.3 Application to active region AR 11087

We now apply the code to AR 11087, as observed on July 15th, 2010. The observations made by AIA are used as input for the code. The advantage of this AR is that it was also observed by the STEREO probes, being 77 degrees apart from SDO/AIA. Therefore, we can compare the STEREO A/EUVI observations with synthesized images derived from the fitting result. The magnetic field was extrapolated by Chifu et al. (2017) with their S-LINFF code. The mapping of the derived fields lines from the extrapolation grid into AIA image coordinates is explained in appendix A.

Figure 8.9 shows the observations in the channels AIA 94, 171, 304 and 335, representing all seven EUV channels. They are compared to the synthesized images resulting from the fitting process. The matching is again outstanding. Like with the test case above, the 304 channel is worst reproduced, while the 335 channel is best. The channels missing in this figure are of similar reproduction quality as the other two channels shown.

From the fitted 3D atmosphere, we can also synthesize images for STEREO A/EUVI (Howard et al., 2008). These synthesized images are compared with the real EUVI observations in figure 8.10. The differences between the two become clearer here. First, the synthesized images are brighter than the observed ones. We will discuss this later. Second, the synthesized image appear more noisy and chaotic. This is expected to some extent. We want to resolve structures along the LOS without a stereoscopic view. It is clear that this cannot work perfectly. Nevertheless, the general, morphological structure of the AR is captured. The vertical "pillar" above the centre of the AR in channel EUVI 195 Å can be seen in the RS image, too. Also, the "lagoon" observed in EUVI 304 has a similar appearance in the RS image. Therefore we think that the general appearance of the AR in the RS EUVI images is acceptable.

In figure 8.11 finally we show the fitted atmosphere itself. Displayed is the column density and the maximum $\lg T$ along the LOS from different view directions. The fitted atmosphere displays features commonly known from real AR atmospheres. The densities have common values, are highest in the core and decrease with altitude. The temperatures of $10^{6.3}$ K to $10^{6.6}$ K are typical for the core of an AR. Very hot, short loops can be found in the core, another common feature of ARs.

Like in the test case, some low lying loops of high density can be seen. Likewise, they are rare

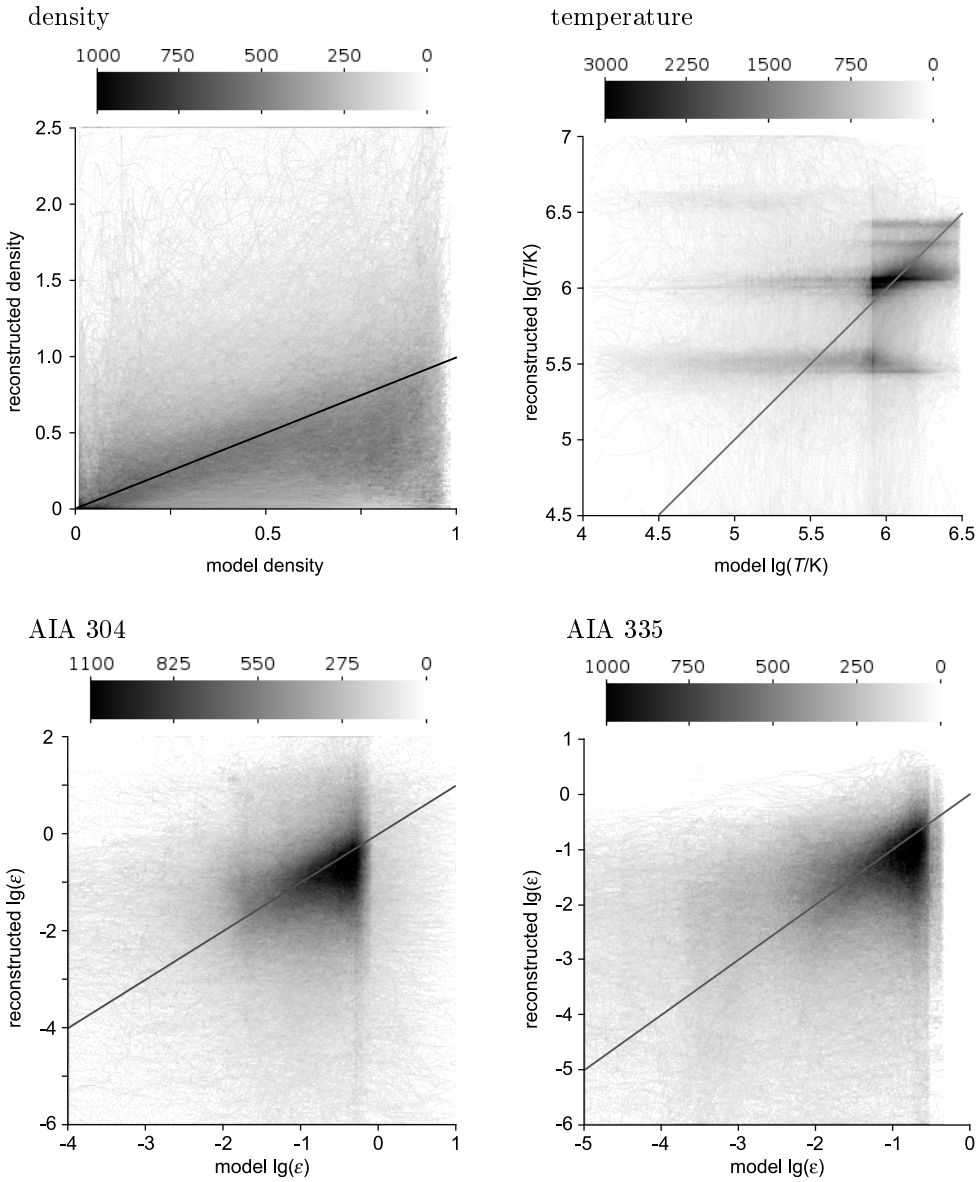

Figure 8.8: Density plots for density, temperature and the "detectable emissivity" $\varepsilon = n^2 K_f(T)$ for the two channels AIA 304 and AIA 335. The black lines indicate the line of identity where model value and fitted value are equal (from Barra, re-submitted to Solar Physics).

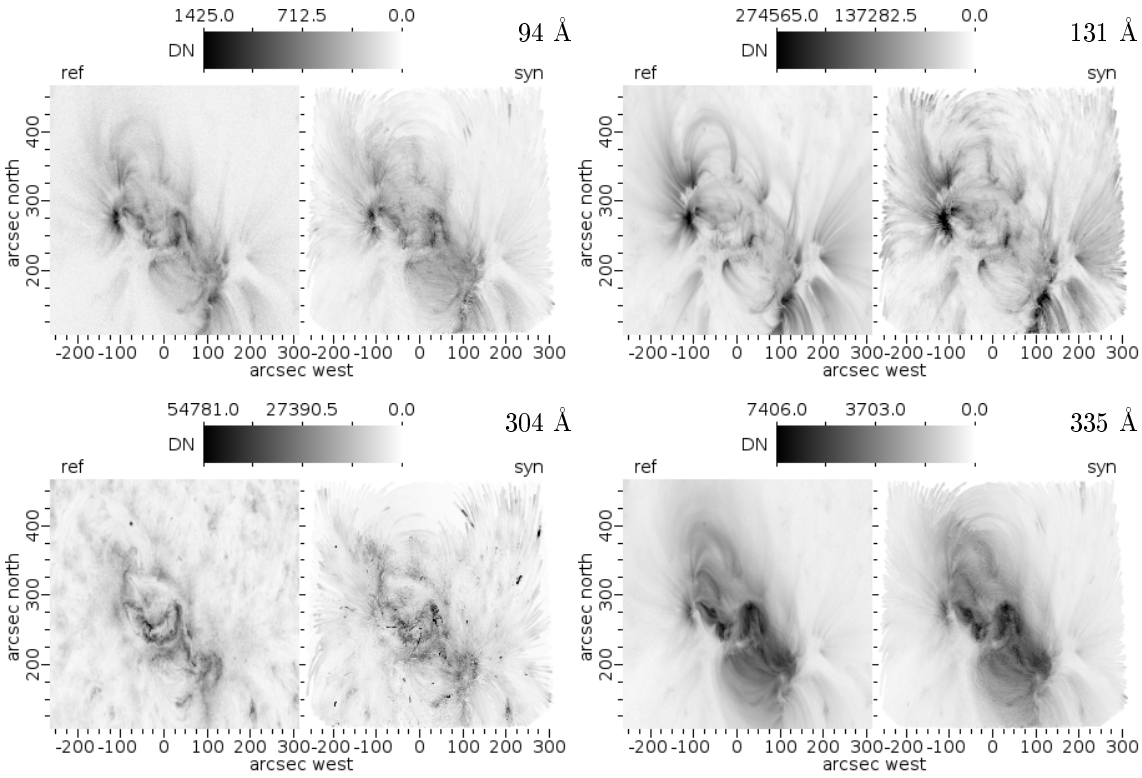

Figure 8.9: AIA observations (left in each pair) and images synthesized from the fitting results (right in each pair) for AR 11087 (from Barra, re-submitted to Solar Physics).

and isolated, as it can be seen in figure 8.11The generally good appearance of the densities is not destroyed. Outside of the core temperatures are too high, around 10^7 K. This might be caused by the observations being too faint to provide sufficiently good filter ratios.

8.4 Discussion

8.4.1 Estimation of the errors

It can be read from figure 8.7 that the densities scatter by around 50%. This is relatively low compared to the two orders of magnitude the density can vary within an AR (table 2.1). The logarithm of temperature displays an relative error of 4%. The range of temperatures in an AR is $10^{5.9}$ K to $10^{6.7}$ K (table 2.1), so that a variation in the exponent by about 0.3 is quite significant. Nevertheless, an order of magnitude estimation is possible.

8.4.2 Bright synthesized EUVI images

The RS images of AR 11087 for EUVI (figure 8.10) are between five times and ten times brighter than the observed ones. As the factor differs for the different filters, this cannot be explained by an overestimated density alone.

One possible effect coming into play here is the degradation. For synthesizing the images, we only have access to the launch values of the response functions $K_f(T)$. Since the instrument had been in space for four years by the time of the observations, it surely had suffered from degradation until then. This makes the observed images darker. Another point which likely plays a role are the errors in density, which tend to brighten the synthesized images. Due to the squared dependency of the intensity on the density, an overestimation has a stronger impact than an underestimation.

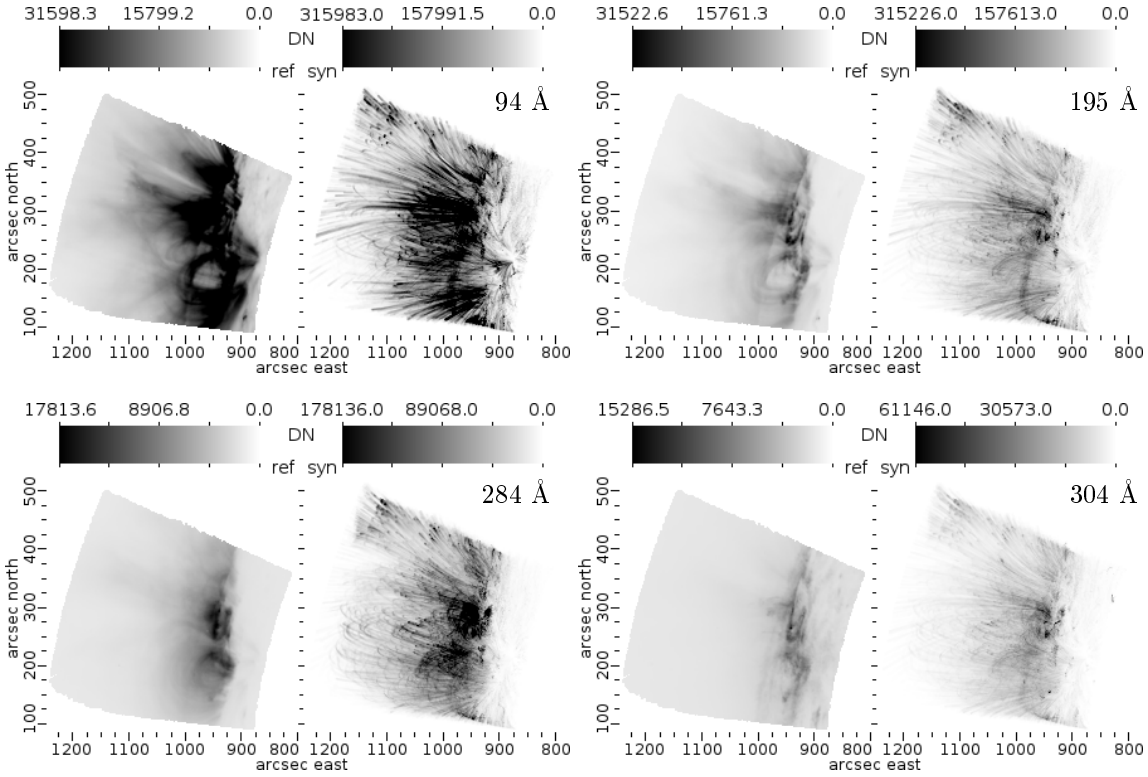

Figure 8.10: STEREO A/EUVI observations (left in each pair) and images synthesized from the fitting results (right in each pair) for AR 11087 (from Barra, re-submitted to Solar Physics).

8.4.3 Known issues

Two things must be kept in mind when using the *FitCoPI* approach. First are the temperatures near the lower boundary of the computational box. As mentioned above, coronal temperatures are smoothed down to bottom facet of the box. A chromosphere, or even photosphere, is not resolved. This has, however, surprisingly little effect onto the reconstruction of the atmosphere in the remaining volume. This is possibly due to the fact that most emission in the observed EUV regime originates from the corona.

A second issue appears when the LOS of the instrument used for the fitting passes through the box first but exits it again before reaching the solar surface. This, actually, happens during the application to AR 11087, in the northern part of the images. The situation is sketched in figure 8.12. Depicted is the numerical volume above the solar surface, as seen from STEREO A, and a LOS of SDO. The box is defined by the field extrapolation. Outside of it, no field data is available. The LOS passes through the box as well as through a volume not included into the computation. The emission from the latter region (noted *b* in the figure) is still observed, and contributes to the fitting process. The *FitCoPI* code compensates for this by increasing the density along the parts of the LOS that are within the box (*a* in the figure) to unnaturally high values. This effect can be seen in the top edges of the synthesized EUVI images in figure 8.10.

8.4.4 Comparison to other works

In Warren et al. (2018), the authors promote a method that links traced coronal loops with field lines derived from field extrapolations. This method also has the potential to obtain the 3D atmosphere: From the loops, when traced in several EUV filters, the physical properties of the plasma can be obtained, for example using a DEM analysis (Craig and Brown, 1976; Kashyap and Drake, 1998; Hannah and Kontar, 2012). At the same time, the field lines provide the three

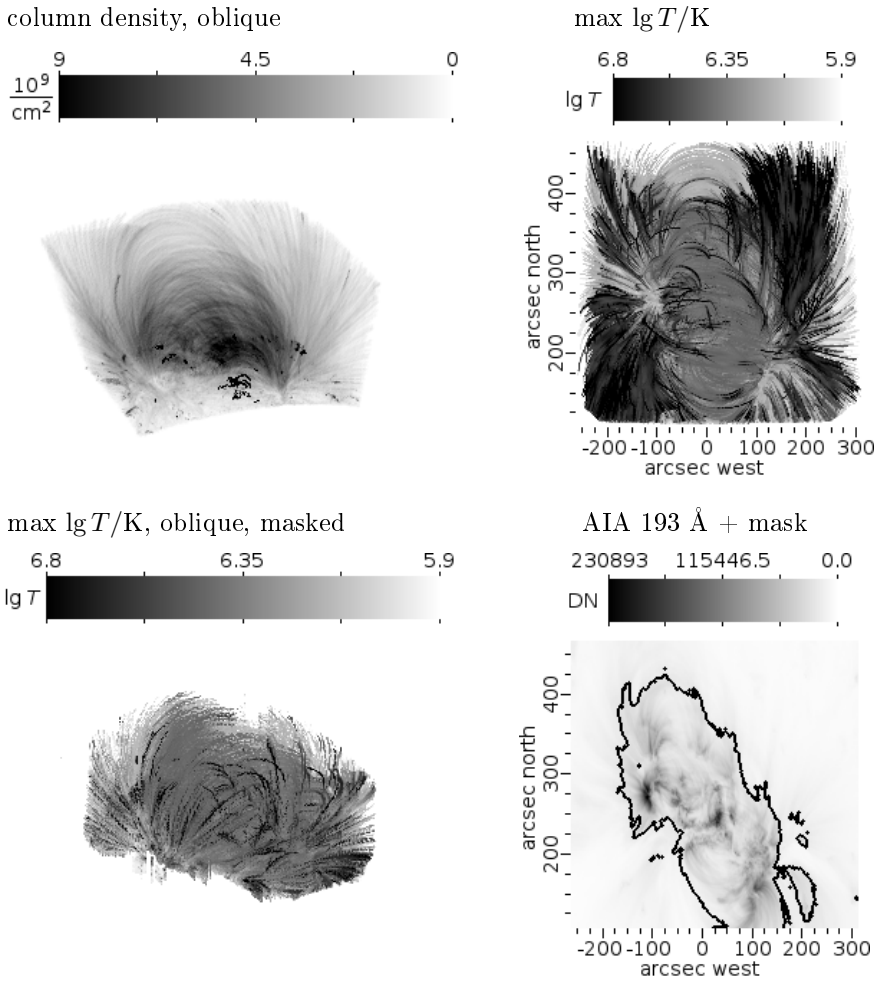

Figure 8.11: The fitted atmosphere for AR 11087. The lower left panel shows the maximum of lg T from a vantage point in the north west. Displayed is only the parts of the AR which, in the observations, reach 10% of the observed maximum intensity in at least two AIA channels. The mask is shown in the lower right panel along the AIA 193 observations (from Barra, re-submitted to Solar Physics).

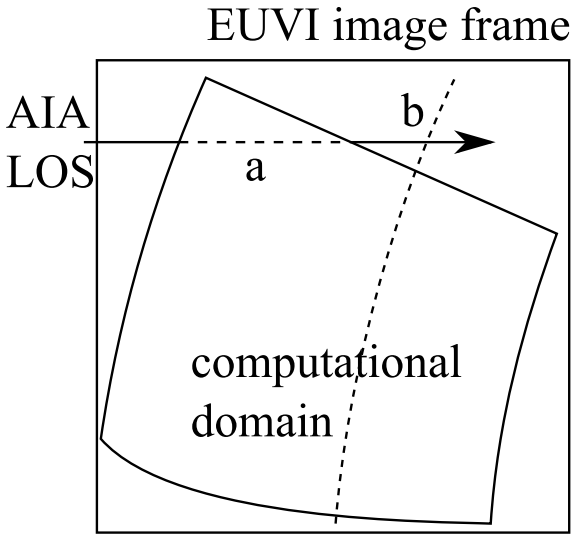

Figure 8.12: LOS not fully passing through the computational domain (from Barra, re-submitted to Solar Physics).

dimensional location in space. This method can gain physical properties, however, only where loops can be traced. Especially in the core this can be difficult. Also, along the LOS of each pixel the physical quantity can be obtained for only one point, as only one loop can be traced in each pixel. Nevertheless, the information yielded by this method may be sufficient to interpolate the atmosphere in the entire AR. Compared to that, our method has a resolution along the LOS. It also does not rely on traced loops but obtains data along all the field lines. The field lines do not have to coincide with coronal loops. But first, the extrapolation methods have been evolved so far that they produce quite good matching with the real field. Second, it is one of the main conclusions of Warren et al. (2018) that the field lines of the NLFFF have a very good coincidence with the observed loops. The advantage of the method by Warren et al. (2018) compared to *FitCoPI* is that they can deploy well tested methods for determining the plasma density and temperature, while this determination is part of our newly developed code. We think that both codes do not stand against each other but could be combined: The method by Warren et al. (2018) may provide an initial condition or even an constraint to the *FitCoPI* code.

8.5 Conclusion

The *FitCoPI* approach can reproduce an AR corona quite well. Although it is still not perfect, it can definitely provide an approximation of the atmosphere. The synthesized images along the LOS match the observations used for the fitting process remarkably well. Also the side views can be reproduced to a good extent. The magnitude and distribution of density and temperature in the synthesized atmosphere are common for AR coronas. The errors allow for order of magnitude estimations. The rank correlations in the test case are rather 0.4 than 0.8, but still significantly above the critical threshold for uncorrelated values. Reliable solutions are found only along LOSs that pass through the numerical box entirely, but current field line extrapolations of ARs are limited to the vicinity of the disk-centre anyway.

Having in mind that our implementation of *FitCoPI* presented here is a kind of prototype, the good results are even more astonishing. Barra (re-submitted to Solar Physics) mentions a list of points that can be improved within the frame. With the promising results here and some possibilities for improvements at hand, we conclude that the *FitCoPI* approach is an ansatz which should be pursued further.

Chapter 9

Summary, conclusions and outlook

9.1 Summary

In this thesis, we investigated several approaches to model the AR corona on the Sun. Observational constraints and inputs are provided by the SDO of NASA (Pesnell et al., 2012), mainly by the EUV imager AIA (Lemen et al., 2012) and the polarimeter HMI (Schou et al., 2012, chapter 4). Compared to other ways of analysing the physical conditions in the corona (for example Kashyap and Drake, 1998; Hannah and Kontar, 2012; Aschwanden et al., 2013), we intended to achieve a three dimensional model atmosphere rather than two dimensional maps. In contrast to tomographic and stereoscopic methods (like Aschwanden et al., 2000a; Vásquez et al., 2011), we also wanted the model to work for a single instrument and with a single set of observations taken in a short time (a minute or so).

Coronal models incorporate coronal heating. Therefore, if a model is able to reproduce the observed appearance of an AR corona, it can be deduced that the incorporated heating mechanism is likely to act in the observed AR. Such conclusions are desirable as the roles of different mechanisms in coronal heating are still under debate.

In all of the methods we investigated here, extrapolated magnetic fields and the field lines derived from that fields are used as a tracer for the loops. We use non-linear force-free-field models, namely the code by Wiegelmann et al. (2012) and its stereoscopic extension by Chifu et al. (2017). As these extrapolation codes are applicable only to ARs near the centre of the solar disk, we also focus on such ARs.

Goal of all methods is to obtain the physical quantities, electron density, electron temperature and gas pressure, along the field lines. After obtaining these quantities, images can be synthesized from the model atmosphere which can be compared against real observations. Also, the distribution of the quantities can be analysed for which heating mechanism fits best, if not already known.

First, we tried to retrieve the quantities along the loops (or in our case: the field lines) directly from the observations (chapter 6). The method of background subtraction and filter ratio analysis used is described in Aschwanden et al. (2008a). In the core of the AR, loops are heavily criss-crossing in the observed images. We found that this makes, in our opinion, an appropriate background subtraction impossible. The method is, hence, not feasible. We note that Aschwanden et al. (2013) published a code which incorporates an automated detection of loops in AIA observations. They detect the loops directly from the contrasts in the images, without using field lines. However, sometimes they also have problems to detect loops in the cores of near-disk-centre ARs, resulting in some voids without detected loops (compare their figure 11).

Next, we applied static loop models to the field lines (chapter 7). We used the classical model by Rosner et al. (1978) and the model by Serio et al. (1981). We combined them with scalings from Golub et al. (1982) and Schrijver et al. (2004) to close the set of equations. We also applied an isothermal model made by ourselves. Besides the NLFFF we also used a LFFF and a potential field model. None of the models can reproduce the EUV observations, and all have to be rejected.

As a consequence, no statement about the actual heating mechanisms can be made. This is in line with the work by Lundquist et al. (2008a), Warren and Winebarger (2006) and Dudík et al. (2011). They mainly modelled the AR corona with static models fitting X-ray observations. When they synthesized EUV images from their solutions, these images were not able to match observations either. However, the NLFFF produces a rather organic, realistic shaped AR, while the LFFF and the potential field cause the AR to appear very artificial in its morphology. This is contradicting to Lundquist et al. (2008a) who claimed that the difference in the appearance of the modelled AR between using a potential field and a NLFFF is negligible.

Finally, we developed a new code for iteratively fitting the 3D atmosphere using the fields lines and single vantage point observations (Barra, re-submitted to Solar Physics, chapter 8). The code, labelled *Fitting Coronal Plasma iteratively FitCoPI*, updates the physical properties at each point on the field lines, followed by smoothing the updates. This smoothing allows to discriminate between two loops in locations where they cross each other in the observations. In this early stage, the code is able to reproduce the observations quite remarkably. This is especially true for the observations that are used for the fitting input. Besides of this, though with some larger errors, also observations from other vantage points made at the same time match images synthesized from the fitted atmosphere very well. The errors in density and temperature, determined on the basis of a test case, allow for order of magnitude estimations. Possibilities how to further improve the code are given in Barra (re-submitted to Solar Physics), too. Warren et al. (2018) published a way to link traced loops in the observations to field lines yielded from field extrapolations. This method allows to gain a 3D atmosphere, too. Their method is, consequently, limited to the loops actually detected, which is difficult in the core. Compared to that, we can gain atmospheric reconstruction everywhere where there is a field line. Also, their method can yield physical properties for only one point along the LOS of each pixel while our method provides a resolution along the LOS. On the other hand, their method can use the well tested DEM analysis for retrieving the densities and temperatures. Both methods may be combined.

9.2 Conclusions

From the results mentioned above, we can draw several conclusions:

- In the core of an AR, background subtraction is nearly impossible. Directly inferring the physical conditions in loops located there is, therefore, not feasible.
- Static models cannot reproduce the EUV emission of an AR.
- The NLFFF should be preferred for extrapolating coronal magnetic fields from vector magnetograms, compared to potential fields and LFFFs.
- The *FitCoPI* code can already yield a good approximation of the AR corona. As it can be improved, it is an approach which should be pursued further.

9.3 Outlook

Analysing the atmosphere of AR 11087 obtained by the *FitCoPI* code in terms of signatures of heating mechanisms is pending. In the future, we would like to improve the *FitCoPI* approach further. Also, more tests on other active regions are planned as soon as possible to further proof the robustness of the method. Once the code can give very precise results, much better than now, time series of three dimensional AR coronas are possible. Such time series would allow to follow the heating and cooling processes very detailed. Especially, the correlation to the dynamics of the magnetic field can be seen. Surely this would provide strong evidence on the heating mechanisms acting, or not acting, or co-acting in the AR, in different parts of it and at different times.

Appendix A

Mapping the extrapolated fields

The extrapolated coronal magnetic fields used in this thesis are calculated on a rectangular grid based on HMI data. Therefore, the question arises where and how this box appears in the corresponding AIA images. Answering this requires a remapping of the numerical box into the "real world" and a consecutive mapping onto the AIA image or.

The remapping step transforms each point (x, y, z) of the numerical box to spherical coordinates (r, ϑ, φ) with the Sun-centre at $r = 0$, the solar equator at $\vartheta = 0$ and the point on the Sun beneath SDO at $\varphi = 0$. Here, the coordinate r is the radius measured in any unit of length, ϑ is the latitude (ranging from $\pi/2$ at the north pole to $-\pi/2$ at the south pole) and φ the longitude (east to west, ranging from 0 to 2π).

The mapping into the coordinates of the image or the grid for the *FitCoPI* algorithm transforms the (r, ϑ, φ) coordinates of a point into the image coordinates (u, v, w), where u (horizontal east to west axis) and v (vertical south to north axis) are the pixel where this point appears on the image and w is a depth information we need for the *FitCoPI* code.

The coordinates and the mapping used in HMI and AIA data are specified in the FITS keywords CTYPE1 and CTYPE2. The location of a reference point in the image data, its coordinate values, the coordinate increments per pixel and the coordinate units are also given in the header of each FITS image (Hanisch et al., 2001).

The coordinate and map projections systems are given in Thompson (2006).

A.1 Remapping the numerical box

The HMI images of the ARs, used for extrapolations appearing in this thesis, are in Carrington heliographic coordinate system. This coordinate system has the equator as zero latitude. The meridians rotate with a speed of $2\pi/25.38$ days (Thompson, 2006), reminiscing a mean rotation speed of the sun. For the remapping, the offset of the median underneath the observer, SDO in this case, which depends of the date of the observation, has to be known.

In the rectangular numerical box for the field extrapolation, the horizontal coordinates are Carrington longitude (ϕ) and latitude (θ). Therefore it gets slightly distorted when remapping onto the solar surface since the edge closer to a pole is shorter than the edge closer to the equator. The volume occupied by the numerical grid expands outwards (see figure A.1).

In the first step we transform the coordinates into the system we call "heliographic observer orientated" (HGOO) in this thesis (figure A.2). The solar horizon is at $\vartheta = 0$, the solar north pole at $\vartheta = \pi/2$. The meridian of longitude $\varphi = 0$ is determined as the one underneath the observer (who is assumed not to hover exactly over one of the poles) and increases to the west. This means, compared to Carrington coordinates, only the longitude changes depending on the

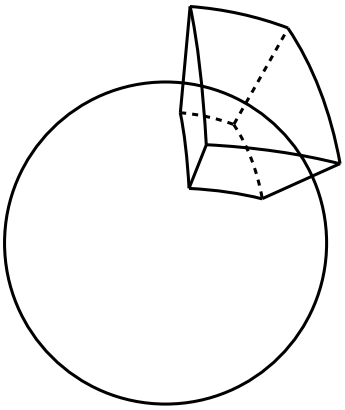

Figure A.1: Distortion of the rectangular grid used for the field extrapolation when remapped onto the sun. For making the effect clearly visible we used an extremely large volume in this sketch.

observer's Carrington longitude, ϕ_{obs}.

$$\begin{aligned}\vartheta &= \theta \\ \varphi &= \phi - \phi_{obs}.\end{aligned}$$

The distance r remains unchanged, quite naturally.

In the next step the HGOO coordinates are transformed into a system we announce as "helioequatorial Cartesian" coordinates here (HEQC, also figure A.2). This is a orthonormal Cartesian coordinate system $\vec{e}_a, \vec{e}_b, \vec{e}_c$ with the origin in the solar centre. The $\vec{e}_b$ axis points towards the solar north pole, the $\vec{e}_c$ axis towards the $\varphi = 0$ meridian. Since the north pole is also located on this meridian, the observer, by definition, is in the bc plane defined by $a = 0$. The $\vec{e}_a$ unit vector completes the basis vectors such that they build a right handed system, i.e. $\vec{e}_b \times \vec{e}_c = \vec{e}_a$. The HEQC coordinates follow from the HGOO coordinates by

$$\begin{aligned}a &= r \cos\vartheta \sin\varphi \\ b &= r \sin\vartheta \\ c &= r \cos\vartheta \cos\varphi.\end{aligned}$$

From the HEQC we easily arrive to the well used Heliocentric Cartesian coordinates (HCC, Thompson 2006), using x, y, z, by tilting the HEQC by the observer's Carrington latitude θ_{obs}. In HCC, the $\hat{x}$ axis is identical to the a axis, but the $\hat{z}$ axis now points directly towards the observer. The $\hat{y}$ axis completes the right handed system (see figure A.2).

$$\begin{pmatrix}\hat{x} \\ \hat{y} \\ \hat{z}\end{pmatrix} = \begin{pmatrix}1 & 0 & 0 \\ 0 & \cos\theta_{obs} & -\sin\theta_{obs} \\ 0 & \sin\theta_{obs} & \cos\theta_{obs}\end{pmatrix} \begin{pmatrix}a \\ b \\ c\end{pmatrix}.$$

A.2 Mapping to AIA images

Unlike the HMI data, AIA images use helioprojective coordinates, an observer centred spherical coordinate system, together with a gnomonic projection (HP, figure A.3). This is, the angle between a certain view direction and the central view direction of SDO increases linearly with each pixel in both the horizontal and vertical direction of the image axes. With the distance between observer

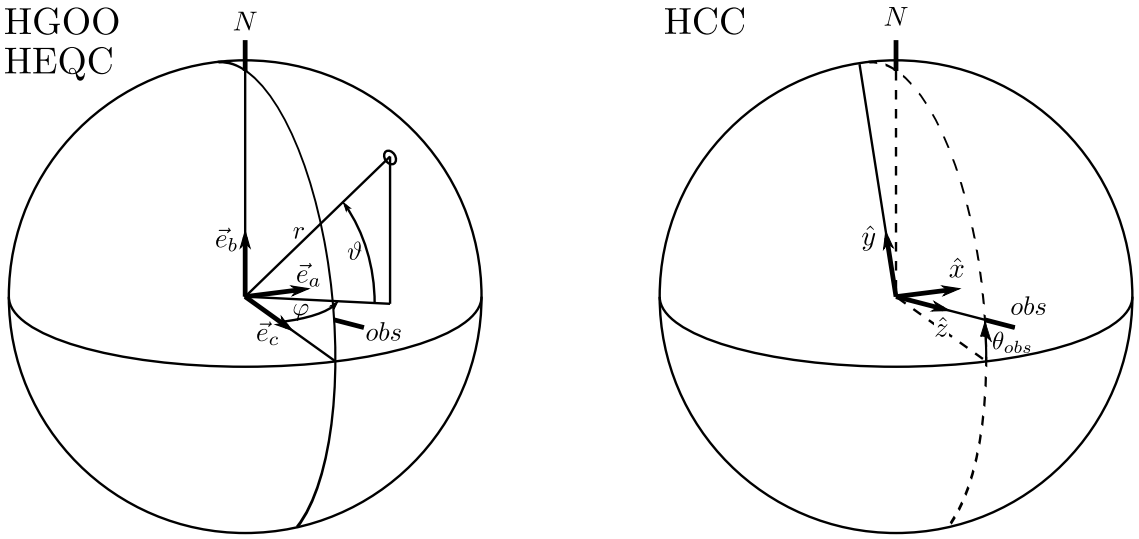

Figure A.2: Definition of the heliographic observer orientated and the helioequatorical Cartesian coordinates (left) as well as the heliocetric Cartesian coordinates (right). Denoted are the solar north pole (N) and the point on the surface underneath the observer (obs). Also depicted are the equator and the meridian of the observer, which is the zero meridian in the HGOO system.

and sun centre, d_{obs}, given, the HP coordinates follow from the HCC coordinates by

$$\begin{aligned}\alpha &= \tan^{-1}\left(\frac{\hat{x}}{d_{obs}-\hat{z}}\right)\\ \beta &= \sin^{-1}\left(\frac{\hat{y}}{\rho}\right)\\ \rho &= \left(\hat{x}^2+\hat{y}^2+(d_{obs}-\hat{z})^2\right)^{1/2},\end{aligned}$$

as specified in (Thompson, 2006). Note that this is a left handed coordinate system.

The pixel coordinates u (horizontal) and v (vertical) of a point on the AIA images are determined by the angular spacing Δ_α and Δ_β, as well as the location (u_0, v_0) of the disc centre on the image. We also take the chance to define the depth coordinate w in a way that (u, v, w) are a right handed coordinate system again.

$$\begin{aligned}u &= \frac{\alpha}{\Delta_\alpha}+u_0\\ v &= \frac{\beta}{\Delta_\beta}+v_0\\ w &= \frac{d_{obs}-\rho}{d}.\end{aligned}$$

Here, d is the physical grid spacing of the extrapolation grid[1], and thus has the same meaning as in chapter 8. The depth coordinate w is 0 when the point is as far from the observer as the centre of the sun and increases towards the observer.

A.3 The FitCoPI grid

For the *FitCoPI* code, it is sufficient taking a cut out of the full AIA image which engulfs the AR of interest. Once the field lines have been determined, their maximum extent towards the left, the

[1] Or, at least, a representative value for it, since this grid is distorted.

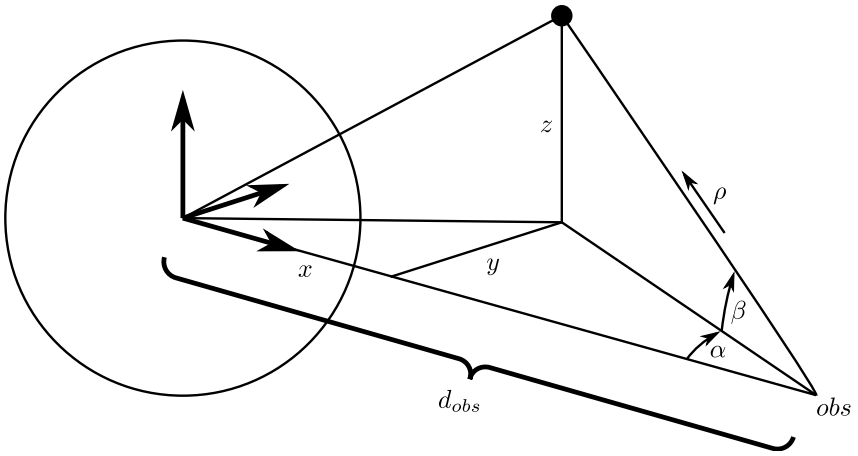

Figure A.3: Definition of the helioprojective coordinates. Shown is also the basis of the heliocentric Cartesian coordinates, as well as the x, y, z coordinates of an example and its correlated α, β, ρ. The location of the observer is denoted by *obs*.

bottom and the far distance, u_{min}, v_{min} and w_{min}, respectively, are known. This is also true for the extents into the opposite directions, u_{max}, v_{max} and w_{max}. Additionally, a boundary of width B pixels around the cut out containing the field lines might be wanted. In this case, the cut out is

$$\begin{aligned} u_{left} &= \lfloor u_{min} - 0.5 \rfloor - B \\ u_{right} &= \lceil u_{max} - 0.5 \rceil + B \\ v_{bottom} &= \lfloor v_{min} - 0.5 \rfloor - B \\ v_{top} &= \lceil v_{max} - 0.5 \rceil + B. \end{aligned}$$

The cut out ranges across the pixels u_{left} to u_{right} horizontally and v_{bottom} to v_{top} in the vertical direction, all boundaries included. It must be noted that this is true when the lower left edge of the image has the pixel coordinates (0,0) and the indices of the pixels are counted from 0 on. In FITS files, the indices begin at 1, giving the lower left corner a pixel coordinate of (0.5, 0.5). This is taken into account by the subtraction of 0.5 in the equations above.

The grid coordinates of a point write now as

$$\begin{aligned} x &= u - 0.5 - u_{left} \\ y &= v - 0.5 - v_{bottom} \\ z &= w - w_{min}. \end{aligned}$$

Again, due to the index counting in FITS images, 0.5 has been subtracted.

We use this set of grid coordinates (x, y, z), for the *FitCoPI* computations and the cut out for the reference images. In the computations, this grid is a rectangular grid. In reality, a very small residual angle remains as the volume is a wedge taken from a sphere. However, both the close and the far edge of the domain are located at a large distance from the observer (much further away than their mutual distance). Due to this geometrical configuration, the rectangular grid is a reasonable approximation. Figure A.4 over exaggerates the situation for displaying the important angles and distances more clear.

Nevertheless, we conclude this section with the necessary evaluation of the errors made by assuming the grid to be rectangular. In the rectangular approximation, the spacing between two points of the same z remains constant when reducing their z by the same amount, while in reality this spacing increases due to the spherical geometry of the coordinate system. When shifting from a distance d_{near} to a distance d_{far} from the observer, a spacing s_{near} increases to

$$s_{far} = s_{near} \frac{d_{far}}{d_{near}}.$$

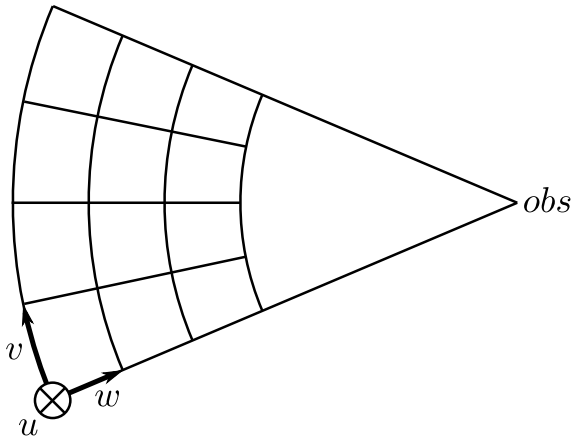

Figure A.4: The coordinates for the numerical grid. During the *FitCoPI* computation, this grid is assumed to be rectangular. Since the angles are much smaller than drawn in this image, this assumption does introduce only negligible errors (see text for details).

In an extreme case of low d_{near} and large separation, like $d_{far} = 148\ 504$ Mm, $d_{near} = 148\ 104$ Mm, this causes an increase by a factor of

$$\frac{d_{far}}{d_{near}} = 1 + \frac{d_{far} - d_{near}}{d_{near}} \approx 0.0027$$

This values reflects earth to be at perihelion ($d_{sun} = 149\ 600$ Mm). With the radius of the Sun being 696 Mm (both values, see for example Stix, 2004), d_{far} is the distance between the centre of the Earth and the subterrestrian point on the solar surface. The error caused by assuming the grid coordinates to form a rectangular grid is not larger than 0.3%, which is much less than the observational errors of AIA.

Appendix B

Curriculum Vitae

Stephan Barra
M.Sc. in Physik

Geboren:	1984
Geboren in:	Witten

Studium

seit 2.4.2012	Promotion zum Thema „Coronal active region modelling based on SDO data“ am MPI für Sonnensystemforschung im Rahmen der International Max Planck Research School for Solar System Sciene.
6.8.2007 – 2.9.2010	Studium M.Sc. Physik an der Ruhr-Universität Bochum, Abschlussarbeit zum Thema „Der räumliche Diffusionstensor geladener Teilchen in symmetriefreien Magnetfeldern“, Note: 1,2.
1.10.2004 – 8.8.2007	Studium B.Sc. Physik an der Ruhr-Universität Bochum, Abschlussarbeit zum Thema „Instabilitäten in anisotropen, kalten Plasmen“, Note: 2,5.

Schulischer Werdegang

1995 – 2004	Lessing-Gymnasium Bochum, abgeschlossen mit Abitur, Note 2,2.
1991 – 1995	Kirchschule Bochum, Grundschule.

Wissenschftl. Tätigkeiten

15.10.2016 – 15.4.2017 und 1.11.2010 – 15.5.2011	Wissenschaftlicher Mitarbeiter am Lehrstuhl für Theoretische Weltraum- und Astrophysik an der Ruhr–Universität Bochum.

Bochum, 24. 4. 2019

Appendix C

Acknowledgements

I thank my advisers Dr. Thomas Wiegelmann and PD Dr. Horst Fichtner for their helpful input to this work.

I thank my family and my friends and especially my dad for their support.

I thank the *International Max Planck Research School* for funding the Work.

Without them, this work would never have been possible. Someone else would have to come up with the ideas presented here, then.

Appendix D

Illustration credits

Figure 1.1: by Ralf Künneman, published under the Creative Commons Attributions Share-alike 2.5 generic licence (`https://creativecommons.org/licenses/by-sa/2.5/deed.en`).

Figures 2.2, 6.2, 6.3, 7.2a, 7.3a, 7.6 right panel, 7.11 AIA 211 panel, 7.16 AIA 171 panel, 8.4 observations, 8.11 AIA 193 panel: These figures use images with courtesy of NASA/SDO and the AIA, EVE and HMI science teams.

Figure 2.3, lower panel: from Wedemeyer-Böhm et al. (2009). Reprinted by permission from Springer Nature Customer Service Centre GmbH, *Space Science Reviews*, S. Wedemeyer-Böhm, A. Lagg, Å. Nordlund: Coupling from the Photosphere to the Chromosphere and the Corona, Springer Science+Business Media B.V. © 2008, transformed to grey-scale

Figure 2.4: from Gary (2001). Reprinted by permission from Springer Nature Customer Service Centre GmbH, *Solar Physics*, G. A. Gary: Plasma Beta above a Solar Active Region: Rethinking the Paradigm, Kluwer Academic publishers © 2001

Figure 4.4: from Grigis et al. (2012), in grey-scale, courtesy of NASA/SDO and the AIA science team (`www.lmsal.com/sdodocs/doc?cmd=dcur&proj_num=SDO0064&file_type=pdf`)

Figures 8.1, 8.2, 8.3, 8.4, 8.5, 8.6, 8.7, 8.8, 8.9, 8.10, 8.11, 8.12, Table 8.1: Grey-scaled and, partially, older versions from Barra, which, in the meanwhile, has been published in *Solar Physics* 294: 101, July 2019, doi: 10.1007/s11207-019-1428-y under the Creative Commons Attributions 4.0 International License (`https://creativecommons.org/licenses/by/4.0/`)

Figure 8.10 observations: This figure uses images with courtesy of NASA/STEREO and the SECCHI science team.

Bibliography

T. E. Abdelatif. Heating of coronal loops by phase-mixed shear Alfvén waves. *Astrophysical Journal*, 322:494–502, November 1987. doi: 10.1086/165745.

AIA webpage. URL `http://aia.lmsal.com`.

P. Antolin and L. Rouppe van der Voort. Observing the Fine Structure of Loops through High-resolution Spectroscopic Observations of Coronal Rain with the CRISP Instrument at the Swedish Solar Telescope. *Astrophysical Journal*, 745:152, February 2012. doi: 10.1088/0004-637X/745/2/152.

S. Arrhenius. On the Physical Nature of the Solar Corona. *Astrophysical Journal*, 20:224, October 1904. doi: 10.1086/141154.

M. J. Aschwanden. Revisiting the Determination of the Coronal Heating Function from Yohkoh Data. *Astrophysical Journal Letters*, 559:L171–L174, October 2001. doi: 10.1086/323788.

M. J. Aschwanden. *Physics of the Solar Corona.* Springer-Verlag, 2004. ISBN 3-540-22321-5.

M. J. Aschwanden, D. Alexander, N. Hurlburt, J. S. Newmark, W. M. Neupert, J. A. Klimchuk, and G. A. Gary. Three-dimensional Stereoscopic Analysis of Solar Active Region Loops. II. SOHO/EIT Observations at Temperatures of 1.5-2.5 MK. *Astrophysical Journal*, 531:1129–1149, March 2000a. doi: 10.1086/308483.

M. J. Aschwanden, T. D. Tarbell, R. W. Nightingale, C. J. Schrijver, A. Title, C. C. Kankelborg, P. Martens, and H. P. Warren. Time Variability of the "Quiet" Sun Observed with TRACE. II. Physical Parameters, Temperature Evolution, and Energetics of Extreme-Ultraviolet Nanoflares. *Astrophysical Journal*, 535:1047–1065, June 2000b. doi: 10.1086/308867.

M. J. Aschwanden, N. V. Nitta, J.-P. Wuelser, and J. R. Lemen. First 3D Reconstructions of Coronal Loops with the STEREO A+B Spacecraft. II. Electron Density and Temperature Measurements. *Astrophysical Journal*, 680:1477–1495, June 2008a. doi: 10.1086/588014.

M. J. Aschwanden, J.-P. Wülser, N. V. Nitta, and J. R. Lemen. First Three-Dimensional Reconstructions of Coronal Loops with the STEREO A and B Spacecraft. I. Geometry. *Astrophysical Journal*, 679:827-842, May 2008b. doi: 10.1086/529542.

M. J. Aschwanden, J.-P. Wuelser, N. V. Nitta, J. R. Lemen, and A. Sandman. First Three-Dimensional Reconstructions of Coronal Loops with the STEREO A+B Spacecraft. III. Instant Stereoscopic Tomography of Active Regions. *Astrophysical Journal*, 695:12–29, April 2009. doi: 10.1088/0004-637X/695/1/12.

M. J. Aschwanden, P. Boerner, C. J. Schrijver, and A. Malanushenko. Automated Temperature and Emission Measure Analysis of Coronal Loops and Active Regions Observed with the Atmospheric Imaging Assembly on the Solar Dynamics Observatory (SDO/AIA). *Solar Physics*, 283:5–30, March 2013. doi: 10.1007/s11207-011-9876-5.

M. Asplund, N. Grevesse, A. J. Sauval, and P. Scott. The Chemical Composition of the Sun. *Annual Review of Astronomy & Astrophysics*, 47:481–522, September 2009. doi: 10.1146/annurev.astro.46.060407.145222.

S. Barra. The FitCoPI code: Iterative determination of the 3D density and temperature configuration in the active region corona. re-submitted to Solar Physics.

A. J. C. Beliën, P. C. H. Martens, and R. Keppens. Coronal Heating by Resonant Absorption: The Effects of Chromospheric Coupling. *Astrophysical Journal*, 526:478–493, November 1999. doi: 10.1086/307980.

N. H. Bian, E. P. Kontar, and A. G. Emslie. Suppression of Parallel Transport in Turbulent Magnetized Plasmas and Its Impact on the Non-thermal and Thermal Aspects of Solar Flares. *Astrophysical Journal*, 824:78, June 2016. doi: 10.3847/0004-637X/824/2/78.

P. Boerner, C. Edwards, J. Lemen, A. Rausch, C. Schrijver, R. Shine, L. Shing, R. Stern, T. Tarbell, A. Title, C. J. Wolfson, R. Soufli, E. Spiller, E. Gullikson, D. McKenzie, D. Windt, L. Golub, W. Podgorski, P. Testa, and M. Weber. Initial Calibration of the Atmospheric Imaging Assembly (AIA) on the Solar Dynamics Observatory (SDO). *Solar Physics*, 275:41–66, January 2012. doi: 10.1007/s11207-011-9804-8.

T. J. M. Boyd and J. J. Sanderson. *The Physics of Plasmas*. Cambridge University Press, 2003. ISBN 978-0-521-45912-9.

R. J. Bray, L. E. Cram, C. J. Durrant, and R. E. Loughhead. *Plasma loops in the Solar Corona*. Cambridge University Press, digitally printed first paperback edition 2005 edition, 1991. ISBN 978-0-521-02223-1.

M. Cassé and P. Goret. Ionization models of cosmic ray sources. *Astrophysical Journal*, 221: 703–712, April 1978. doi: 10.1086/156075.

J. Chae, U. Schühle, and P. Lemaire. SUMER Measurements of Nonthermal Motions: Constraints on Coronal Heating Mechanisms. *Astrophysical Journal*, 505:957–973, October 1998. doi: 10.1086/306179.

J. Chae, A. I. Poland, and M. J. Aschwanden. Coronal Loops Heated by Magnetohydrodynamic Turbulence. I. A Model of Isobaric Quiet-Sun Loops with Constant Cross Sections. *Astrophysical Journal*, 581:726–735, December 2002. doi: 10.1086/344103.

I. Chifu, T. Wiegelmann, and B. Inhester. Nonlinear Force-free Coronal Magnetic Stereoscopy. *Astrophysical Journal*, 837:10, March 2017. doi: 10.3847/1538-4357/aa5b9a.

J. W. Cirtain, L. Golub, A. R. Winebarger, B. de Pontieu, K. Kobayashi, R. L. Moore, R. W. Walsh, K. E. Korreck, M. Weber, P. McCauley, A. Title, S. Kuzin, and C. E. Deforest. Energy release in the solar corona from spatially resolved magnetic braids. *Nature*, 493:501–503, January 2013. doi: 10.1038/nature11772.

J. W. Cook, C.-C. Cheng, V. L. Jacobs, and S. K. Antiochos. Effect of coronal elemental abundances on the radiative loss function. *Astrophysical Journal*, 338:1176–1183, March 1989. doi: 10.1086/167268.

I. J. D. Craig and J. C. Brown. Fundamental limitations of X-Ray spectra as diagnostics of plasma temperature sructure. *Astronomy and Astrophysics*, 49:239–250, June 1976.

J. M. Davila. Heating of the solar corona by the resonant absorption of Alfven waves. *Astrophysical Journal*, 317:514–521, June 1987. doi: 10.1086/165295.

A. De Groof and M. Goossens. Fast and Alfvén waves driven by azimuthal footpoint motions. II. Random driver. *Astronomy & Astrophysics*, 386:691–698, May 2002. doi: 10.1051/0004-6361:20020204.

I. De Moortel and P. Browning. Recent advances in coronal heating. *Philosophical Transactions of the Royal Society of London Series A*, 373:20140269–20140269, April 2015. doi: 10.1098/rsta.2014.0269.

B. De Pontieu, S. W. McIntosh, M. Carlsson, V. H. Hansteen, T. D. Tarbell, P. Boerner, J. Martinez-Sykora, C. J. Schrijver, and A. M. Title. The Origins of Hot Plasma in the Solar Corona. *Science*, 331:55, January 2011. doi: 10.1126/science.1197738.

Jose Carlos del Toro Iniesta. *Introduction to Spectropolarimetry*. Cambridge University Press, 2003. ISBN 0-521-03648-1.

G. Del Zanna. The multi-thermal emission in solar active regions. *Astronomy & Astrophysics*, 558:A73, October 2013. doi: 10.1051/0004-6361/201321653.

G. Del Zanna, B. O'Dwyer, and H. E. Mason. SDO AIA and Hinode EIS observations of "warm" loops. *Astronomy and Astrophysics*, 535:A46, September 2011.

G. Del Zanna, K. P. Dere, P. R. Young, E. Landi, and H. E. Mason. CHIANTI - An atomic database for emission lines. Version 8. *Astronomy & Astrophysics*, 582:A56, October 2015. doi: 10.1051/0004-6361/201526827.

K. P. Dere, E. Landi, H. E. Mason, B. C. Monsignori Fossi, and P. R. Young. CHIANTI - an atomic database for emission lines. *Astronomy & Astrophysics Supplement Series*, 125, October 1997. doi: 10.1051/aas:1997368.

P. Dmitruk, D. O. Gómez, and E. E. DeLuca. Magnetohydrodynamic Turbulence of Coronal Active Regions and the Distribution of Nanoflares. *Astrophysical Journal*, 505:974–983, October 1998. doi: 10.1086/306182.

J. Dudík, E. Dzifčáková, M. Karlický, and A. Kulinová. Is it possible to model observed active region coronal emission simultaneously in EUV and X-ray filters? *Astronomy & Astrophysics*, 531:A115, July 2011. doi: 10.1051/0004-6361/201015947.

B. Edlén. Die Deutung der Emissionslinien im Spektrum der Sonnenkorona. Mit 6 Abbildungen. *Zeitschrift für Astrophysik*, 22:30, 1943.

EVE webpage. URL `http://lasp.colorado.edu/home/eve/`.

U. Feldman, P. Mandelbaum, J. F. Seely, G. A. Doschek, and H. Gursky. The potential for plasma diagnostics from stellar extreme-ultraviolet observations. *Astrophysical Journal Supplement Series*, 81:387–408, July 1992. doi: 10.1086/191698.

L. Feng, B. Inhester, S. K. Solanki, T. Wiegelmann, B. Podlipnik, R. A. Howard, and J.-P. Wuelser. First Stereoscopic Coronal Loop Reconstructions from STEREO SECCHI Images. *Astrophysical Journal Letters*, 671:L205–L208, December 2007. doi: 10.1086/525525.

B. Fleck, V. Domingo, and A. I. Poland. The SOHO mission. *Solar Physics*, 162, December 1995.

L. Fletcher and B. De Pontieu. Plasma Diagnostics of Transition Region "Moss" using SOHO/CDS and TRACE. *Astrophysical Journal Letters*, 520:L135–L138, August 1999. doi: 10.1086/312157.

J. M. Fontenla, E. H. Avrett, and R. Loeser. Energy balance in the solar transition region. I - Hydrostatic thermal models with ambipolar diffusion. *Astrophysical Journal*, 355:700–718, June 1990. doi: 10.1086/168803.

P. Foukal. Magnetic loops, downflows, and convection in the solar corona. *Astrophysical Journal*, 223:1046–1057, August 1978. doi: 10.1086/156338.

P. V. Foukal. The pressure and energy balance of the cool corona over sunspots. *Astrophysical Journal*, 210:575–581, December 1976. doi: 10.1086/154862.

S. L. Freeland and B. N. Handy. Data Analysis with the SolarSoft System. *Solar Physics*, 182: 497–500, October 1998. doi: 10.1023/A:1005038224881.

G. A. Gary. Plasma Beta above a Solar Active Region: Rethinking the Paradigm. *Solar Physics*, 203:71–86, October 2001. doi: 10.1023/A:1012722021820.

L. Golub, G. Noci, G. Poletto, and G. S. Vaiana. Active Region Coronal Evolution. *The Astrophysical Journal*, 259:359–365, August 1982.

Leon Golub and Jay M. Pasachoff. *The Solar Corona*. Cambridge University Press, second edition edition, 2010. ISBN 978-0-521-88201-9.

N. Grevesse and A. J. Sauval. Standard Solar Composition. *Space Science Reviews*, 85:161–174, May 1998. doi: 10.1023/A:1005161325181.

Paolo. Grigis, Yingna. Su, and Mark Weber. AIA PSF Characterization and Image Deconvolution. February 2012. URL `www.lmsal.com/sdodocs/doc?cmd=dcur&pro\T1\j_num=SDOD0076&file_type=pdf`.

W. Grotrian. Ergebnisse der Potsdamer Expedition zur Beobachtung der Sonnenfinsternis am 9. Mai 1929 in Takengon (Nordsumatra). 6. Mitteilung. Über die Intensitätsverteilung des kontinuierlichen Spektrums der inneren Korona. Mit 8 Abbildungen. (Eingegangen am 27. Juni 1931). *Zeitschrift für Astrophysik*, 3:199, 1931.

W. Grotrian. Zur Frage der Deutung der Linien im Spektrum der Sonnenkorona. *Die Naturwissenschaften*, 27:214, March 1939.

R. J. Hanisch, A. Farris, E. W. Greisen, W. D. Pence, B. M. Schlesinger, P. J. Teuben, R. W. Thompson, and A. Warnock, III. Definition of the Flexible Image Transport System (FITS). *Astronomy & Astrophysics*, 376:359–380, September 2001. doi: 10.1051/0004-6361:20010923.

I. G. Hannah and E. P. Kontar. Differential emission measures from the regularized inversion of Hinode and SDO data. *Astronomy & Astrophysics*, 539:A146, March 2012. doi: 10.1051/0004-6361/201117576.

J. Heyvaerts and E. R. Priest. Coronal heating by phase-mixed shear Alfv'en waves. *Astronomy & Astrophysics*, 117:220–234, January 1983.

J. Heyvaerts and E. R. Priest. A self-consistent turbulent model for solar coronal heating. *Astrophysical Journal*, 390:297–308, May 1992. doi: 10.1086/171280.

HMI webpage. URL `http://hmi.stanford.edu`.

J. V. Hollweg. Transition region, corona, and solar wind in coronal holes. *Journal of Geophysical Research*, 91:4111–4125, April 1986. doi: 10.1029/JA091iA04p04111.

A. W. Hood, D. Gonzalez-Delgado, and J. Ireland. Heating of coronal loops by phase-mixing. *Astronomy & Astrophysics*, 324:11–14, August 1997.

R. A. Howard, J. D. Moses, A. Vourlidas, J. S. Newmark, D. G. Socker, S. P. Plunkett, C. M. Korendyke, J. W. Cook, A. Hurley, J. M. Davila, W. T. Thompson, O. C. St Cyr, E. Mentzell, K. Mehalick, J. R. Lemen, J. P. Wuelser, D. W. Duncan, T. D. Tarbell, C. J. Wolfson, A. Moore, R. A. Harrison, N. R. Waltham, J. Lang, C. J. Davis, C. J. Eyles, H. Mapson-Menard, G. M. Simnett, J. P. Halain, J. M. Defise, E. Mazy, P. Rochus, R. Mercier, M. F. Ravet, F. Delmotte, F. Auchere, J. P. Delaboudiniere, V. Bothmer, W. Deutsch, D. Wang, N. Rich, S. Cooper, V. Stephens, G. Maahs, R. Baugh, D. McMullin, and T. Carter. Sun Earth Connection Coronal and Heliospheric Investigation (SECCHI). *Space Science Reviews*, 136:67–115, April 2008. doi: 10.1007/s11214-008-9341-4.

H. S. Hudson. Solar flares, microflares, nanoflares, and coronal heating. *Solar Physics*, 133:357–369, June 1991. doi: 10.1007/BF00149894.

J. A. Ionson. Resonant absorption of Alfv'enic surface waves and the heating of solar coronal loops. *Astrophysical Journal*, 226:650–673, December 1978. doi: 10.1086/156648.

P. A. Isenberg. Investigations of a turbulence-driven solar wind model. *Journal of Geophysical Research*, 95:6437–6442, May 1990. doi: 10.1029/JA095iA05p06437.

M. L. Kaiser, T. A. Kucera, J. M. Davila, O. C. St. Cyr, M. Guhathakurta, and E. Christian. The STEREO Mission: An Introduction. *Space Science Reviews*, 136:5–16, April 2008. doi: 10.1007/s11214-007-9277-0.

V. Kashyap and J. J. Drake. Markov-Chain Monte Carlo Reconstruction of Emission Measure Distributions: Application to Solar Extreme-Ultraviolet Spectra. *Astrophysical Journal*, 503: 450–466, August 1998. doi: 10.1086/305964.

James A. Klimchuk. On Solving the Coronal Heating Problem. *Solar Physics*, 234:41–77, March 2006. doi: 10.1007/s11207-006-0055-z.

E. P. Kontar, N. H. Bian, A. G. Emslie, and N. Vilmer. Turbulent Pitch-angle Scattering and Diffusive Transport of Hard X-Ray-producing Electrons in Flaring Coronal Loops. *Astrophysical Journal*, 780:176, January 2014. doi: 10.1088/0004-637X/780/2/176.

M. Kramar, S. Jones, J. Davila, B. Inhester, and M. Mierla. On the Tomographic Reconstruction of the 3D Electron Density for the Solar Corona from STEREO COR1 Data. *Solar Physics*, 259:109–121, October 2009. doi: 10.1007/s11207-009-9401-2.

E. Landi, U. Feldman, and K. P. Dere. CHIANTI-An Atomic Database for Emission Lines. V. Comparison with an Isothermal Spectrum Observed with SUMER. *Astrophysical Journal Supplement Series*, 139:281–296, March 2002. doi: 10.1086/337949.

J. R. Lemen, A. M. Title, D. J. Akin, P. F. Boerner, C. Chou, J. F. Drake, D. W. Duncan, C. G. Edwards, F. M. Friedlaender, G. F. Heyman, N. E. Hurlburt, N. L. Katz, G. D. Kushner, M. Levay, R. W. Lindgren, D. P. Mathur, E. L. McFeaters, S. Mitchell, R. A. Rehse, C. J. Schrijver, L. A. Springer, R. A. Stern, T. D. Tarbell, J.-P. Wuelser, C. J. Wolfson, C. Yanari, J. A. Bookbinder, P. N. Cheimets, D. Caldwell, E. E. Deluca, R. Gates, L. Golub, S. Park, W. A. Podgorski, R. I. Bush, P. H. Scherrer, M. A. Gummin, P. Smith, G. Auker, P. Jerram, P. Pool, R. Soufli, D. L. Windt, S. Beardsley, M. Clapp, J. Lang, and N. Waltham. The Atmospheric Imaging Assembly (AIA) on the Solar Dynamics Observatory (SDO). *Solar Physics*, 275:17–40, January 2012. doi: 10.1007/s11207-011-9776-8.

D. D. Lenz, E. E. Deluca, L. Golub, R. Rosner, J. A. Bookbinder, C. Litwin, F. Reale, and G. Peres. Long-lived Coronal Loop Profiles from TRACE. *Solar Physics*, 190:131–138, December 1999. doi: 10.1023/A:1005209616355.

D. M. Long, G. Valori, D. Pérez-Suárez, R. J. Morton, and A. M. Vásquez. Measuring the magnetic field of a trans-equatorial loop system using coronal seismology. *Astronomy & Astrophysics*, 603: A101, July 2017. doi: 10.1051/0004-6361/201730413.

L. L. Lundquist, G. H. Fisher, and J. M. McTiernan. Forward Modeling of Active Region Coronal Emissions. I. Methods and Testing. *Astrophysical Journal Supplement Series*, 179:509–533, December 2008a. doi: 10.1086/592775.

L. L. Lundquist, G. H. Fisher, T. R. Metcalf, K. D. Leka, and J. M. McTiernan. Forward Modeling of Active Region Coronal Emissions. II. Implications for Coronal Heating. *Astrophysical Journal*, 689:1388–1405, December 2008b. doi: 10.1086/592760.

B. Lyot. L'Etude de la Couronne Solaire en Dehors des Eclipses. *L'Astronomie*, 45:248–253, 1931.

B. Lyot. Étude de la couronne solaire en dehors des éclipses. Avec 16 figures dans le texte. *Zeitschrift für Astrophysik*, 5:73, 1932.

A. Malanushenko, C. J. Schrijver, M. L. DeRosa, M. S. Wheatland, and S. A. Gilchrist. Guiding Nonlinear Force-free Modeling Using Coronal Observations: First Results Using a Quasi-Grad-Rubin Scheme. *Astrophysical Journal*, 756:153, September 2012. doi: 10.1088/0004-637X/756/2/153.

F. Malara, P. Petkaki, and P. Veltri. Dissipation of Alfvén Waves in Force-free Magnetic Fields: Competition between Phase Mixing and Three-dimensional Effects. *Astrophysical Journal*, 533: 523–534, April 2000. doi: 10.1086/308636.

E. Marsch and C.-Y. Tu. The effects of high-frequency Alfv'en waves on coronal heating and solar wind acceleration. *Astronomy & Astrophysics*, 319:L17–L20, March 1997a.

E. Marsch and C.-Y. Tu. Solar Wind and Chromospheric Network. *Solar Physics*, 176:87–106, November 1997b. doi: 10.1023/A:1004975703854.

H. E. Mason and B. C. M. Fossi. Spectroscopic diagnostics in the VUV for solar and stellar plasmas. *Astronomy & Astrophysics Review*, 6:123–179, November 1994. doi: 10.1007/BF01208253.

I. Milić and M. van Noort. Line response functions in nonlocal thermodynamic equilibrium. Isotropic case. *Astronomy & Astrophysics*, 601:A100, May 2017. doi: 10.1051/0004-6361/201629980.

R. J. Morton and J. A. McLaughlin. High-resolution Observations of Active Region Moss and its Dynamics. *Astrophysical Journal*, 789:105, July 2014. doi: 10.1088/0004-637X/789/2/105.

D. Müller, R. G. Marsden, O. C. St. Cyr, and H. R. Gilbert. Solar Orbiter . Exploring the Sun-Heliosphere Connection. *Solar Physics*, 285:25–70, July 2013. doi: 10.1007/s11207-012-0085-7.

P. H. et al. Müller. *Lexikon der Stochastik*. Akademie-Verlag, 1975.

U. Narain and P. Ulmschneider. Chromospheric and Coronal Heating Mechanisms II. *Space Science Reviews*, 75:453–509, February 1996. doi: 10.1007/BF00833341.

L. Ofman and M. J. Aschwanden. Damping Time Scaling of Coronal Loop Oscillations Deduced from Transition Region and Coronal Explorer Observations. *Astrophysical Journal Letters*, 576: L153–L156, September 2002. doi: 10.1086/343886.

L. Ofman and T. Wang. Hot Coronal Loop Oscillations Observed by SUMER: Slow Magnetosonic Wave Damping by Thermal Conduction. *Astrophysical Journal Letters*, 580:L85–L88, November 2002. doi: 10.1086/345548.

L. Ofman, J. M. Davila, and R. S. Steinolfson. Coronal heating by the resonant absorption of Alfven waves: The effect of viscous stress tensor. *Astrophysical Journal*, 421:360–371, January 1994. doi: 10.1086/173654.

L. Ofman, J. A. Klimchuk, and J. M. Davila. A Self-consistent Model for the Resonant Heating of Coronal Loops: The Effects of Coupling with the Chromosphere. *Astrophysical Journal*, 493: 474–479, January 1998. doi: 10.1086/305109.

W. J. F. Oliver. *NIST Handbook of Mathematical Functions*. Cambridge University Press, 2010. ISBN 978-0-521-14063-8.

E. N. Parker. Magnetic neutral sheets in evolving fields. I - General theory. *Astrophysical Journal*, 264:635–647, January 1983a. doi: 10.1086/160636.

E. N. Parker. Magnetic Neutral Sheets in Evolving Fields - Part Two - Formation of the Solar Corona. *Astrophysical Journal*, 264:642, January 1983b. doi: 10.1086/160637.

E. N. Parker. Nanoflares and the solar X-ray corona. *Astrophysical Journal*, 330:474–479, July 1988. doi: 10.1086/166485.

W. D. Pesnell, B. J. Thompson, and P. C. Chamberlin. The Solar Dynamics Observatory (SDO). *Solar Physics*, 275:3–15, January 2012. doi: 10.1007/s11207-011-9841-3.

H. Peter and S. Bingert. Constant cross section of loops in the solar corona. *Astronomy & Astrophysics*, 548:A1, December 2012. doi: 10.1051/0004-6361/201219473.

V. Polito, P. Testa, J. Allred, B. De Pontieu, M. Carlsson, T. M. D. Pereira, M. Gošić, and F. Reale. Investigating the Response of Loop Plasma to Nanoflare Heating Using RADYN Simulations. *Astrophysical Journal*, 856:178, April 2018. doi: 10.3847/1538-4357/aab49e.

S. R. Pottasch. The Lower Solar Corona: Interpretation of the Ultraviolet Spectrum. *Astrophysical Journal*, 137:945, April 1963. doi: 10.1086/147569.

W. Press, Sula Teukolsky, W. Vetterling, and B. Flannety. *Numerical Recipes in C*. Cambridge University Press, 1992.

E. R. Priest, C. R. Foley, J. Heyvaerts, T. D. Arber, D. Mackay, J. L. Culhane, and L. W. Acton. A Method to Determine the Heating Mechanisms of the Solar Corona. *Astrophysical Journal*, 539:1002–1022, August 2000. doi: 10.1086/309238.

F. Reale. More on the Determination of the Coronal Heating Function from Yohkoh Data. *Astrophysical Journal*, 580:566–573, November 2002. doi: 10.1086/343123.

R. Rosner, W. H. Tucker, and G. S. Vaiana. Dynamics of the quiescent corona. *The Astrophysical Journal*, 220:643–665, 1978.

S. Sahal-Brechot, M. Malinovsky, and V. Bommier. The polarization of the O VI 1032 A line as a probe for measuring the coronal vector magnetic field via the Hanle effect. *Astronomy & Astrophysics*, 168:284–300, November 1986.

T. Sakurai. A New Approach to the Force-Free Field and Its Application to the Magnetic Field of Solar Active Regions. *Publications of the Astronomical Society of Japan*, 31:209–230, 1979.

J. Schou, P. H. Scherrer, R. I. Bush, R. Wachter, S. Couvidat, M. C. Rabello-Soares, R. S. Bogart, J. T. Hoeksema, Y. Liu, T. L. Duvall, D. J. Akin, B. A. Allard, J. W. Miles, R. Rairden, R. A. Shine, T. D. Tarbell, A. M. Title, C. J. Wolfson, D. F. Elmore, A. A. Norton, and S. Tomczyk. Design and Ground Calibration of the Helioseismic and Magnetic Imager (HMI) Instrument on the Solar Dynamics Observatory (SDO). *Solar Physics*, 275:229–259, January 2012. doi: 10.1007/s11207-011-9842-2.

C. J. Schrijver, A. M. Title, A. A. van Ballegooijen, H. J. Hagenaar, and R. A. Shine. Sustaining the Quiet Photospheric Network: The Balance of Flux Emergence, Fragmentation, Merging, and Cancellation. *Astrophysical Journal*, 487:424–436, September 1997. doi: 10.1086/304581.

C. J. Schrijver, A. W. Sandmann, M. J. Achwanden, and M. L. DeRosa. The coronal heating mechanism as identified by full-sun visualizations. *The Astrophysical Journal*, 615:512–525, November 2004.

K. Schwarzschild. Ueber die totale Sonnenfinsternis vom 30. August 1905. *Astronomische Mitteilungen der Universitaets-Sternwarte zu Goettingen*, 13, 1906.

SDO mission webpage. URL `http://www.nasa.gov/mission-pages/sdo/main/index.html`.

SDO webpage. URL `http://sdo.gsfc.nasa.gov`.

S. Serio, G. Peres, G. S. Vaiana, L. Golub, and R. Rosner. Closed coronal structures. ii. generalized hydrostatic model. *The Astrophysical Journal*, 243:266–300, 1981.

P. L. Similon and R. N. Sudan. Energy dissipation of Alfv'en wave packets deformed by irregular magnetic fields in solar-coronal arches. *Astrophysical Journal*, 336:442–453, January 1989. doi: 10.1086/167023.

Lyman Spitzer. *Physics of Fully Ionized Gases*. Interscience Publishers, second reviewed edition edition, 1962.

Michael Stix. *The Sun*. Springer-Verlag, second edition. corrected second printing 2004 edition, 2004. ISBN 978-3-540-20741-4.

P. Testa, B. De Pontieu, J. Martínez-Sykora, E. DeLuca, V. Hansteen, J. Cirtain, A. Winebarger, L. Golub, K. Kobayashi, K. Korreck, S. Kuzin, R. Walsh, C. DeForest, A. Title, and M. Weber. Observing Coronal Nanoflares in Active Region Moss. *Astrophysical Journal Letters*, 770:L1, June 2013. doi: 10.1088/2041-8205/770/1/L1.

J. K. Thalmann, S. K. Tiwari, and T. Wiegelmann. Force-free Field Modeling of Twist and Braiding-induced Magnetic Energy in an Active-region Corona. *Astrophysical Journal*, 780:102, January 2014. doi: 10.1088/0004-637X/780/1/102.

W. T. Thompson. Coordinate systems for solar image data. *Astronomy & Astrophysics*, 449: 791–803, April 2006. doi: 10.1051/0004-6361:20054262.

A. M. Title and C. J. Schrijver. The Sun's Magnetic Carpet. In R. A. Donahue and J. A. Bookbinder, editors, *Cool Stars, Stellar Systems, and the Sun*, volume 154 of *Astronomical Society of the Pacific Conference Series*, page 345, 1998.

A. A. van Ballegooijen. Cascade of magnetic energy as a mechanism of coronal heating. *Astrophysical Journal*, 311:1001–1014, December 1986. doi: 10.1086/164837.

A. A. van Ballegooijen, M. Asgari-Targhi, and A. Voss. The Heating of Solar Coronal Loops by Alfvén Wave Turbulence. *Astrophysical Journal*, 849:46, November 2017. doi: 10.3847/1538-4357/aa9118.

A. M. Vásquez, Z. Huang, W. B. Manchester, and R. A. Frazin. The WHI Corona from Differential Emission Measure Tomography. *Solar Physics*, 274:259–284, December 2011. doi: 10.1007/s11207-010-9706-1.

R. W. Walsh and J. Ireland. The heating of the solar corona. *Astronomy & Astrophysics Review*, 12:1–41, 2003. doi: 10.1007/s00159-003-0021-9.

H. P. Warren and A. R. Winebarger. Hydrostatic Modeling of the Integrated Soft X-Ray and Extreme Ultraviolet Emission in Solar Active Regions. *Astrophysical Journal*, 645:711–719, July 2006. doi: 10.1086/504075.

H. P. Warren and A. R. Winebarger. Static and Dynamic Modeling of a Solar Active Region. *Astrophysical Journal*, 666:1245–1255, September 2007. doi: 10.1086/519943.

H. P. Warren, A. R. Winebarger, J. T. Mariska, G. A. Doschek, and H. Hara. Observation and Modeling of Coronal "Moss" With the EUV Imaging Spectrometer on Hinode. *Astrophysical Journal*, 677:1395–1400, April 2008. doi: 10.1086/529186.

H. P. Warren, A. R. Winebarger, and D. H. Brooks. Evidence for Steady Heating: Observations of an Active Region Core with Hinode and TRACE. *Astrophysical Journal*, 711:228–238, March 2010. doi: 10.1088/0004-637X/711/1/228.

H. P. Warren, N. A. Crump, I. Ugarte-Urra, X. Sun, M. J. Aschwanden, and T. Wiegelmann. Toward a Quantitative Comparison of Magnetic Field Extrapolations and Observed Coronal Loops. *Astrophysical Journal*, 860:46, June 2018. doi: 10.3847/1538-4357/aac20b.

S. Wedemeyer-Böhm, A. Lagg, and Å. Nordlund. Coupling from the Photosphere to the Chromosphere and the Corona. *Space Science Reviews*, 144:317–350, April 2009. doi: 10.1007/s11214-008-9447-8.

T. Wiegelmann. Nonlinear force-free modeling of the solar coronal magnetic field. *Journal of Geophysical Research (Space Physics)*, 113:A03S02, March 2008. doi: 10.1029/2007JA012432.

T. Wiegelmann, J. K. Thalmann, B. Inhester, T. Tadesse, X. Sun, and J. T. Hoeksema. How Should One Optimize Nonlinear Force-Free Coronal Magnetic Field Extrapolations from SDO/HMI Vector Magnetograms? *Solar Physics*, 281:37–51, November 2012. doi: 10.1007/s11207-012-9966-z.

L. Woltjer. On Hydromagnetic Equilibrium. *Proceedings of the National Academy of Science*, 44: 833–841, September 1958. doi: 10.1073/pnas.44.9.833.

T. N. Woods, F. G. Eparvier, R. Hock, A. R. Jones, D. Woodraska, D. Judge, L. Didkovsky, J. Lean, J. Mariska, H. Warren, D. McMullin, P. Chamberlin, G. Berthiaume, S. Bailey, T. Fuller-Rowell, J. Sojka, W. K. Tobiska, and R. Viereck. Extreme Ultraviolet Variability Experiment (EVE) on the Solar Dynamics Observatory (SDO): Overview of Science Objectives, Instrument Design, Data Products, and Model Developments. *Solar Physics*, 275:115–143, January 2012. doi: 10.1007/s11207-009-9487-6.